Final Report

on

Implication of Wolf Creek Indications – Final Report

to

Nuclear Regulatory Commission
Washington DC

by

D. Rudland, D.-J. Shim, T. Zhang, and G. Wilkowski

Engineering Mechanics Corporation of Columbus
3518 Riverside Drive
Suite 202
Columbus, OH 43221
Phone/Fax (614) 459-3200/-6800

August 2007

Table of Contents

List of Figures

List of Tables

1. Introduction

In October 2006, NRC-RES informed Emc^2 of circumferential indications that had been located by ultrasonic testing (UT) in three of the pressurizer nozzle dissimilar metal (DM) welds at the Wolf Creek nuclear power plant. The NRC staff tasked Emc^2 with analyzing these defects. Using ASME Section XI type analyses, Emc^2 estimated the times to both leakage and rupture for each indication. The results indicated that under certain conditions, no margin between leakage and rupture existed [1]. The results from these analyses led the NRC staff to request that the inspection/mitigation program currently in place for the pressurizer nozzles be accelerated. This acceleration affected nine PWR plants in the current US fleet. In response, the industry embarked on a short-term technical program aimed at refining the crack growth analyses conducted by Emc^2. The main emphasis of the industry program was to use advanced finite element (FE) methods to remove the semi-elliptical flaw assumption that is typical in ASME Section XI type analyses. In addition, detailed sensitivity analyses were conducted to demonstrate that sufficient margins exist for the pressurizer nozzles that would be affected by the accelerated inspection request.

The purpose of this report is two fold. First, using similar techniques, confirmatory analyses were conducted by Emc^2 in order to verify the calculations conducted by the industry [2]. Since both Emc^2 and the NRC staff worked very closely with the industry during the program, many of the technical issues have been discussed and agreed upon. The majority of this report presents the confirmatory results for the stress intensity factor (K) solutions, the welding residual stress, and the leak/rupture margin analyses. Secondly, the applicability of this methodology for predicting leak/rupture margins is addressed by discussing the improvements to the standard methodology, the conservatisms and uncertainties associated with this analysis.

The purpose of this report is not to make an overall judgment of acceptability of these results and their implication to the plants that may be affected by the accelerated inspection request, since that decision requires not only technical but also regulatory insight. The purpose is to verify the industry's results and highlight some of the technical issues that may warrant additional consideration.

2. Description of Confirmatory Analyses

2.1 Development and Description of PipeFracCAE

PipeFracCAE is a FE mesh generator developed by Emc^2 which can be employed to generate three-dimensional FE mesh for a cracked pipe and plate with and without a weld. The FE model generated from PipeFracCAE can be used as a direct input for the commercial FE code ABAQUS[*] [3]. During this effort, PipeFracCAE has been updated with a semi-automated process to handle subcritical crack growth analyses. The key features and limitations of PipeFracCAE are described in the following subsections. Figure 1 shows a screen shot from PipeFracCAE.

---

[*] PipeFracCAE output for Warp3D and ANSYS are under development.
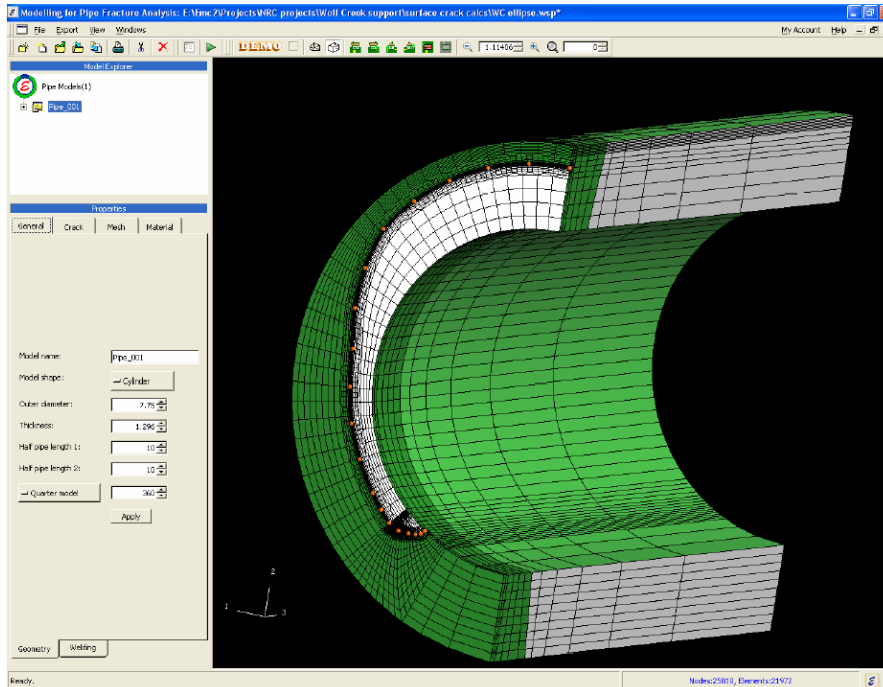
Figure 1 Screen shot from PipeFracCAE

2.1.1   Mesh Generation

Figure 2 shows a typical FE mesh generated from PipeFracCAE. As shown in this figure, the FE model is a quarter symmetric, three-dimensional model. The weld geometry is simplified by assuming a zero bevel angle. Note that in the current version of the crack growth module in PipeFracCAE, the center of the crack must be located on the symmetry plane.

PipeFracCAE is capable of generating a FE mesh with either 8-noded or 20-noded brick elements. For the present effort, 20-node brick elements[†] were employed. Moreover, collapsed crack-tip elements were used for modeling the crack tip with the midside nodes moved to the quarter-point location to generate the $r^{(-1/2)}$ singularity at the crack tip. As shown in Figure 2, concentric rings of elements were used near the crack-tip to calculate the stress intensity factor values.

The internal pressure was applied to the inner surface of the pipe and also 100% of the internal pressure was applied to the crack face to simulate crack-face pressure loading. Axial tension and bending moment were applied at the end of the pipe as a pressure loading.

In order to impose a welding residual stress on the crack plane, an appropriate temperature distribution varying in the thickness and circumferential direction was applied to the weld region. This produced simulated welding residual stress on the crack plane. Since the welding residual

---

[†] Sensitivity studies between 8- and 20-noded elements were conducted and due to the 8-noded mesh density needed for accurate K values, 20-noded elements were used.

stress was imposed through applied displacements, the redistribution of the residual stress was properly captured during the crack growth[‡].
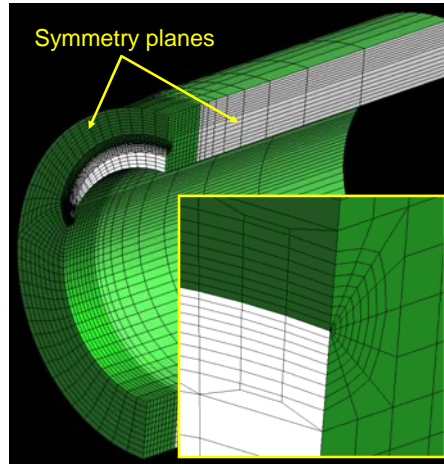
Figure 2 Typical FE mesh generated from PipeFracCAE

The meshing capabilities of PipeFracCAE previous to the current effort were limited to the idealized surface crack, idealized through-wall crack, and idealized complex crack in the circumferential and axial direction. An idealized surface crack is defined by the crack depth and length where the crack shape can be either semi-elliptical or rectangular (constant depth). An idealized through-wall crack assumes a crack front parallel to the pipe radius. For idealized complex cracks, the crack is defined by a constant depth surface crack with two curvatures at both ends. Example meshes for these idealized cracks are shown in Figure 3.

| | | | |
| (a) | (b) | (c) | (d) |
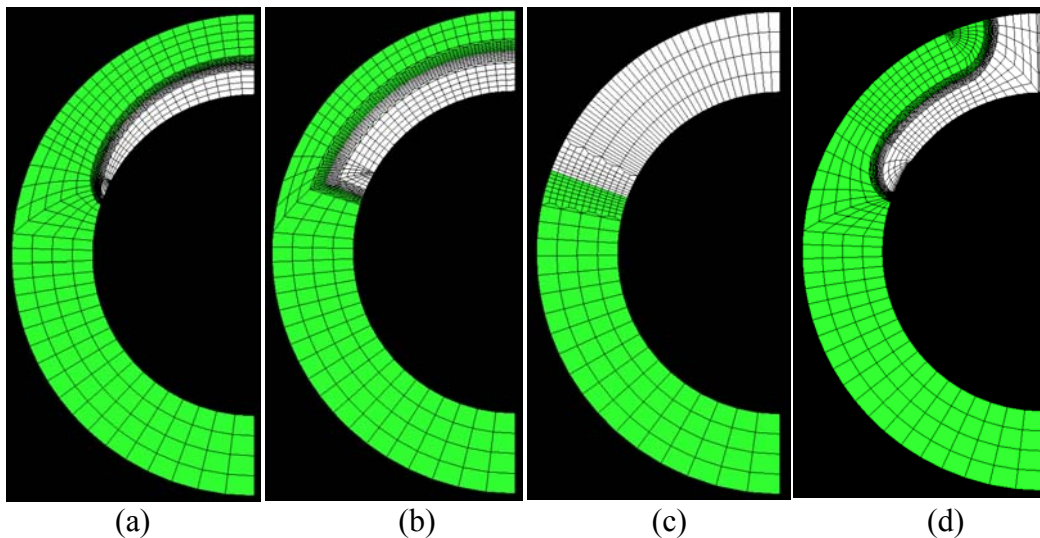
Figure 3 Example mesh of (a) semi-elliptical surface crack, (b) rectangular (constant depth) surface crack, (c) idealized through-wall crack, (d) idealized complex crack

---

[‡] An equilibrated initial stress field could have been used instead of the thermal gradient to approximate the welding residual stress; however this approach was taken to verify the industry's analyses.

In this project, the amount of crack growth at each location along the crack front was based on the stress intensity factor at that point. Since the stress intensity factor is known to vary along the crack front, it was expected that the crack grows in an arbitrary manner. So the first task in the present effort was to extend the capability of PipeFracCAE to handle arbitrary crack shapes. For this purpose, PipeFracCAE was modified so that the crack front can be defined by the user-defined coordinates. As a trial, 20 points were used to define the arbitrary crack shape. However, it was shown that 20 points were not sufficient to smoothly define the crack front for a semi-elliptical crack. Based on this study, PipeFracCAE was modified and 40 points[§] were used to define the arbitrary crack front. Another extension that was incorporated to PipeFracCAE is the full circumferential surface crack. In some cases, a part circumferential surface crack can grow significantly in the circumferential direction while the growth in the thickness direction is limited. In this case, the crack grows to form a full circumferential surface crack. PipeFracCAE was modified to cover this type of crack shape where the crack front is also defined by the 40 points. The final extension that was incorporated to PipeFracCAE is the arbitrary full complex crack, where the crack has a 360 degree crack length on the ID surface and part circumferential crack length on the OD surface. Figure 4 shows some examples of arbitrary shaped cracks generated from PipeFracCAE, where the orange color symbols are the 40 points used to define the crack front. As shown in Figure 5, the crack front nodes are distributed along the crack front defined by the 40 points (the crack front node does not have to be defined on one of the 40 points).

(a)   (b)   (c)
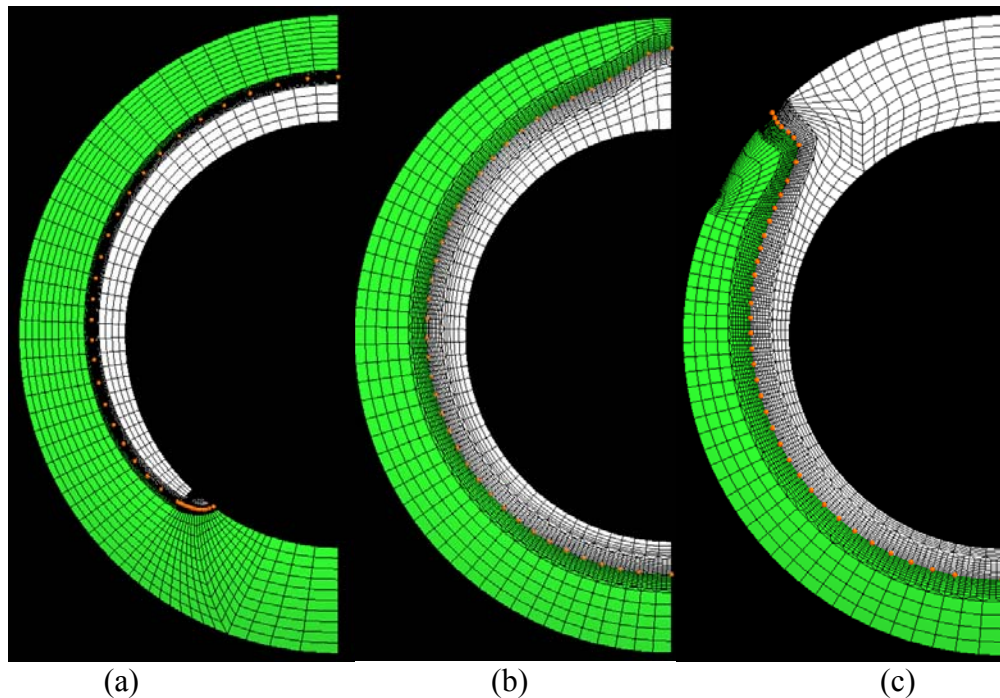
Figure 4 Example mesh of (a) arbitrary finite length surface crack, (b) 360 degree, arbitrary surface crack, (c) arbitrary complex crack

---

[§] The user-defined crack front points are used to generate the crack front nodes, but are not necessarily identical to the nodes.
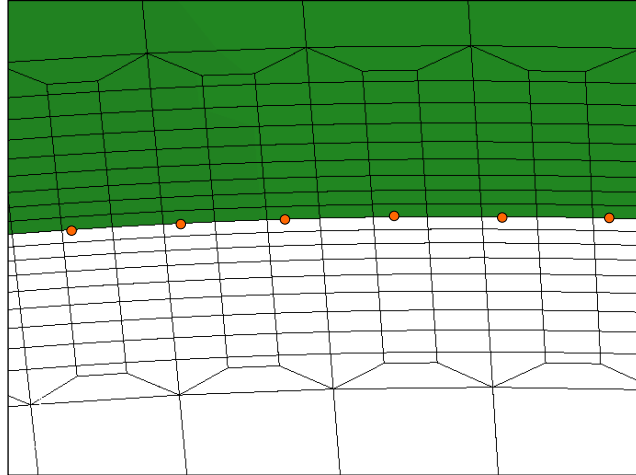
Figure 5 Definition of crack front using 40 points along the crack front

2.1.2   *Crack Growth Modeling*

In the present effort, ABAQUS is employed to calculate the K values at each node along the crack front. These results are then used to determine the amount of crack growth at each location (i.e. each crack front node). The crack growth direction is defined as the direction normal to the crack front at each nodal location. The MRP-115 [4] crack growth rate (75th percentile) for Alloy 182, which is a function of K and temperature, is adopted in the present effort. In PipeFracCAE, the crack growth is controlled by two parameters, i.e., time increment and maximum crack growth length. The time increment, along with the crack growth rate, is used to calculate the amount of crack growth at each crack front node. However, if there is any node point where the amount of crack growth exceeds the maximum crack growth length set by the user, the time increment is automatically reduced so that the maximum crack growth along the crack front does not exceed the maximum crack growth length. This method was employed to ensure that there was no unrealistic jump in the crack growth calculations.

The procedure described above has been incorporated in PipeFracCAE as a semi-automated process. The FE model generated from PipeFracCAE is sent to ABAQUS, which calculates the K values along the crack front. This information is passed back to PipeFracCAE for the crack growth calculation and definition of the new crack front. This process is continued while also considering crack shape transition.

2.1.3   *Crack Shape Transition*

If the initial crack is defined as a part circumferential surface crack and the crack growth in the thickness direction is limited due to compressive welding residual stress, the crack can grow into a full circumferential surface crack. Figure 6 shows an example of a crack front transition from an arbitrary part circumferential surface crack to an arbitrary full circumferential surface crack. As shown in Figure 6, the transition is made smoothly without any discontinuity.

(a)   (b)
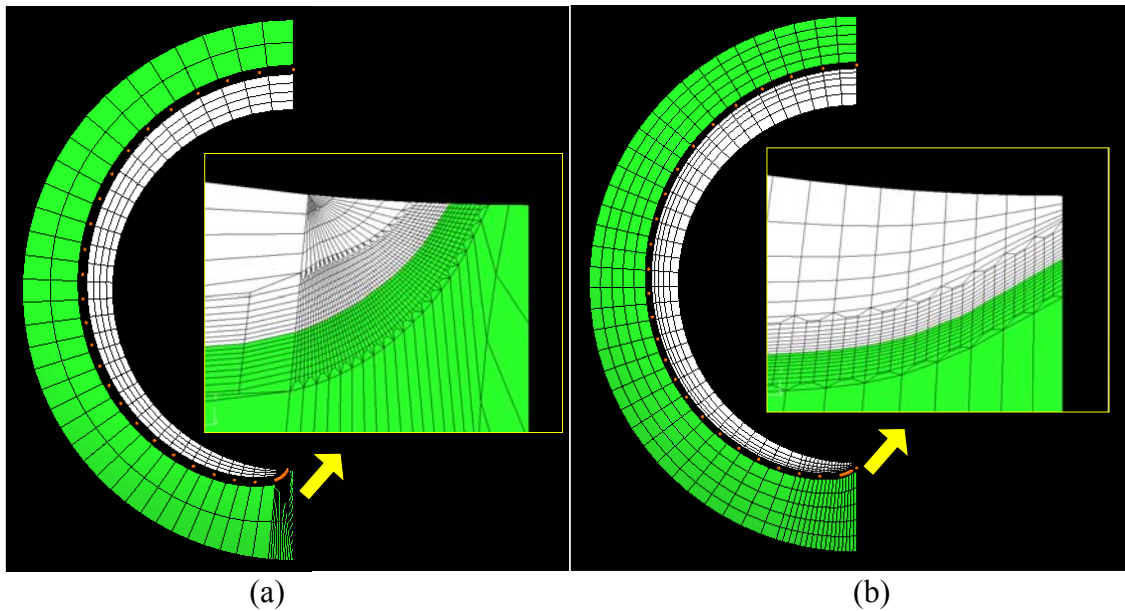
**Figure 6 Transition from (a) arbitrary part circumferential surface crack to (b) arbitrary
full circumferential surface crack**

If the initial crack is defined as a full circumferential surface crack or if a full circumferential
surface crack is formed from a part circumferential surface crack, subsequent crack growth can
cause the crack to penetrate through the wall thickness and form a complex crack. Figure 7
shows an example of a crack front transition from arbitrary full circumferential surface crack to
arbitrary full complex crack. Figure 8 shows how the complex crack front is defined from the
last surface crack front. As described earlier, the crack growth direction at each node is normal to
the crack front. As shown in Figure 8, the new crack front is calculated from the surface crack.
The intersection of the new crack front and the OD surface is defined as the crack-tip location of
the complex crack on the OD surface. So if a small time increment (or small maximum crack
growth length) is used in PipeFracCAE, the crack profile just before or after wall penetration can
be captured.   If the intersection between the new crack front and the OD was sharp, meshing
issues occurred. In this case, any ligament less than 5-10% of the wall thickness was eliminated
as illustrated in Figure 8.

(a)   **(b)**
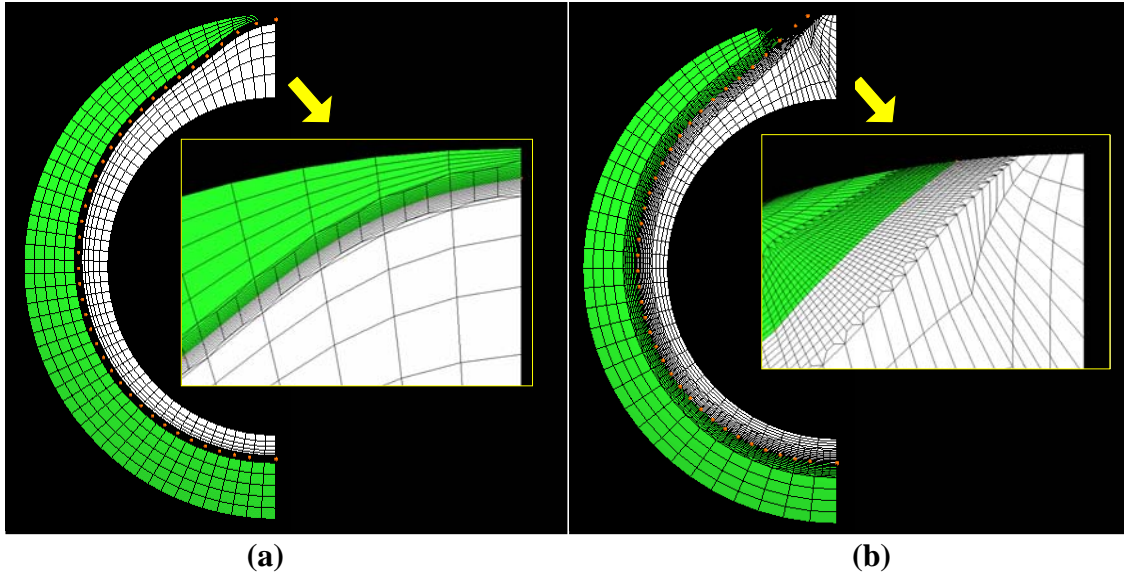
Figure 7 Transition from (a) full circumferential surface crack to (b) full complex crack
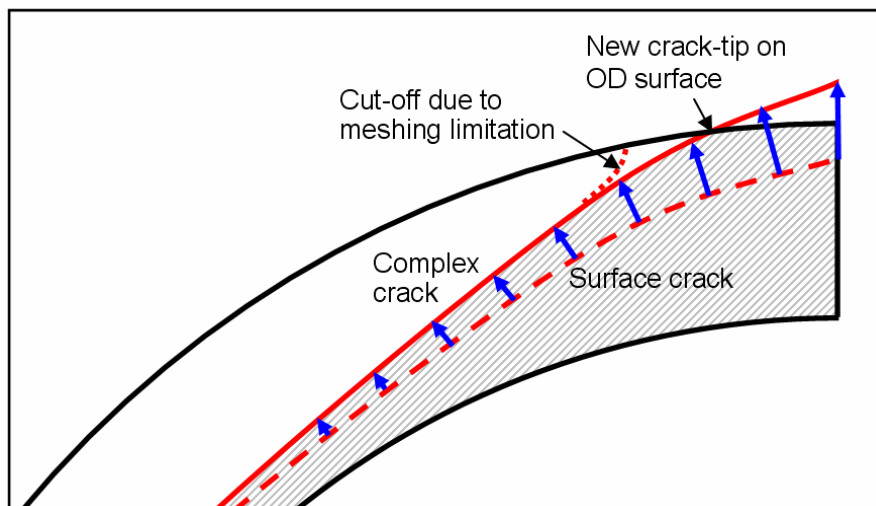
Figure 8 Illustration showing how the complex crack front is defined from growth of a surface crack

2.1.4   *Limitations*

In some of the cases considered in the present effort, the part circumferential surface crack grew into a through-wall crack before growing into a full circumferential surface crack. For this type of crack, an arbitrary through-wall crack module was needed. The need for the arbitrary through-wall crack module arose in the mid-stage of the project. Due to limited time schedule, it was not possible to update PipeFracCAE. As an alternative method, as shown in Figure 9, a fictitious crack was added to extend the part circumferential surface crack into a full circumferential surface crack. Subsequent crack growth was based on the full circumferential surface crack, which grew into a full complex crack.   This assumption is conservative in both critical crack size margin and leak rate.

| Part circumferential surface crack | Full circumferential surface crack | Full complex crack |
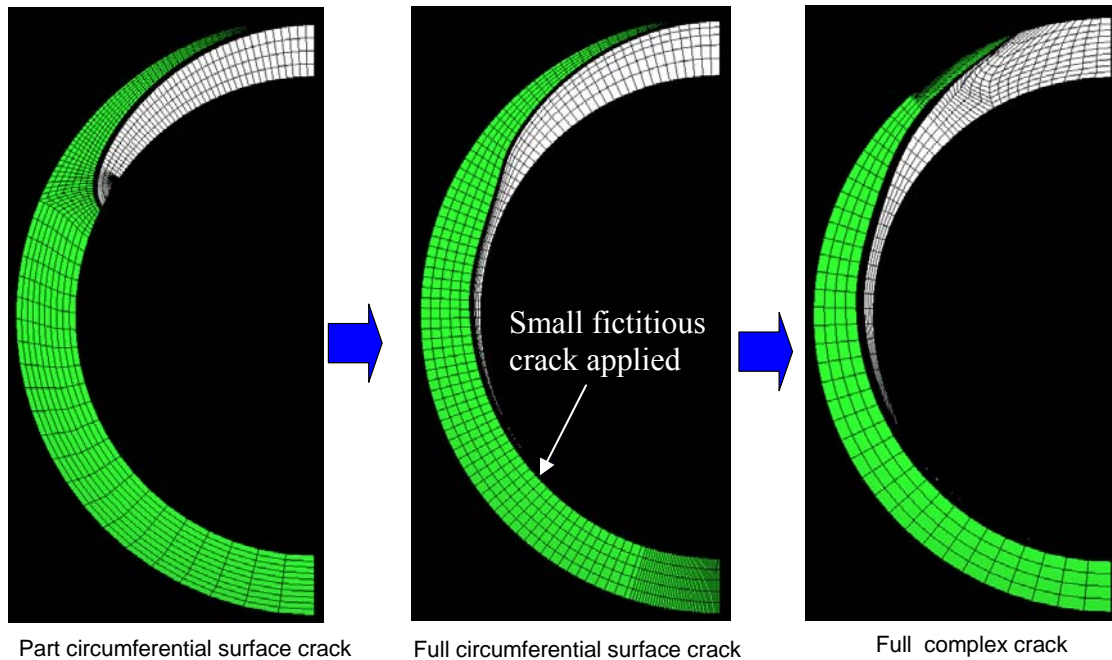
Figure 9 Fictitious crack added to part circumferential surface crack due to meshing limitations

2.2   Critical crack size calculation

Accurate determination of the critical crack size is very important to the prediction of the margin between leakage and rupture. The determination of critical circumferential flaw sizes has been extensively investigated in experimental and analytical efforts since the 1970's for nuclear piping. Much of that work was summarized in Reference 5. The evaluation of cracks in nuclear piping for in-service flaw evaluation procedures is incorporated for nuclear piping in ASME Section XI Articles IWB-3600 as well as Appendix C [6] and H [7]. This flaw evaluation procedure incorporated safety factors on stress that vary for service level. There are criterion for circumferential flaws in stainless steel piping and their welds, ferritic piping and their welds, but not yet for high nickel alloy welds like Alloy 82/182. Currently the criterion for Alloy 82/182 is under development [8].

2.2.1   Technical basis document for critical crack size determination

In order to fully document the past work on the calculation of critical crack size, Emc^2 developed a technical basis document on this subject [9]. This technical basis document was meant as a reference to document the relevant experimental and analytical results for accurately predicting the critical size of both surface and through-wall cracks. It was not meant as a comprehensive review of all of the technical issues pertaining to the criticality of these cracks, but more as a reference document that the reader can use as a guide to finding more technical detail if desired. The issues discussed in this document included:

- The behavior of surface, complex, and through-wall cracks,
- The use of limit-load versus elastic-plastic fracture mechanics,
- Proper material properties to use for accurate failure predictions, and
- Role of secondary stresses.

This document was used as a basis for the calculation of critical crack size in this effort.

2.2.2 *Assumptions and methodologies used for this study*

This section of the report describes the methodologies for the calculation of critical crack size used as part of this effort. The methodology used in this effort was developed from the documentation in Reference 9 and much discussion between the NRC staff and the industry in many of the public meetings that were held in the spring and early summer of 2007. The methodology used was not meant to be generic, but specific for this need and only applicable because further research and development was not possible in the time frame of the program.

Surface cracks

For non-idealized surface cracks, the calculation of critical crack size was determined using the NSC criteria for arbitrary surface cracks developed by Rahman [10]. In this approach, the integration of the cracked area is balanced with the uncracked area and the membrane and bending load required to reach the flow stress is calculated. Extensive past research [9] for cracks in similar metal welds suggest that for limit-load conditions, the base metal flow properties control the behavior. For DM welds, numerical analyses suggest that the lower strength base metal flow properties would produce the limiting results. If the crack in the DM weld is near the center of the weld, a combination of the carbon steel and stainless steel flow stress would control. However, in this effort, since these postulated defects can occur at any location in the weld or butter, the stainless steel flow strength was used conservatively.

Note that in Reference 9, some experimental data were developed which suggest that for deep surface flaws, the NSC predictions were non-conservative, i.e., the experimental loads at failure were much less than predicted by the NSC criteria. However, since further research on this topic was not possible, it was agreed to ignore this effect.

Complex cracks

The analyses conducted in the Phase I effort (Section 5) suggested that once these arbitrary surface cracks break the surface, they would become complex cracks. A complex crack is a combination of a surface and through-wall crack. Limited research has been performed on complex cracks, but the data and analyses presented in Reference 9 (which is based only on base metal experiments), suggests that NSC may be appropriate for these flaws when the Dimensionless Plastic Zone Parameter (DPZP) is greater than 1.0. However, there has been limited research on complex cracks that suggests that the tearing resistance is much lower than a through-wall crack with the same OD crack length, and therefore the appropriate apparent fracture toughness must be used in calculating the DPZP parameter. When the DPZP parameter is less than 1.0, it has been shown that EPFM conditions exist. In those cases, it is appropriate to estimate the load-carrying capacity by the use of the Z-factor, as is done in ASME Section XI analyses. Z-factors have not been developed for complex cracks in Alloy 82/182 materials, but have been suggested for TWC in these materials [8]. Therefore, due to the lack of experimental data on complex cracks in DM welds, it was decided that these flaws would be analyzed using the NSC equations for an arbitrary crack and applying the Z factors per Reference 8 for all cases including those where DPZP>1.

Secondary stresses

The role of displacement-controlled secondary stresses in the critical crack size determination is a hotly debated topic. To understand the role of secondary stresses, the NRC staff[**] conducted pipe system experiments (mid 1990s and early 2000) with typical and elevated levels of thermal expansion stresses [11 and 12]. The details of these experiments are discussed in Reference 9. In summary, the experimental results showed that the secondary stress in this pipe system test acted as a primary stress from a fracture viewpoint due to the size of the surface flaw (a/t ≈ 0.65 and $\theta/\pi \approx 0.5$), which localized the plasticity at the crack plane and allowed negligible plasticity in the uncracked pipe loop. The rotations due to the surface crack (up to maximum load) are very small compared to the pipe rotations that can occur due to the thermal expansion stress.

Due to the limited experimental results, it was decided that for the analyses in this study the displacement-controlled thermal expansion stresses (which include the normal thermal stratifications stresses) would be included in the critical crack size determination. All other displacement-controlled stresses, such as the transient thermal stratification stresses, were assumed to be relieved for complex crack evaluations.

The industry conducted two separate analyses to demonstrate the effect of secondary loads on cracked pipe [2]. In the first industry analysis (Appendix B of Ref. 2), an elastic surge line piping analysis was conducted with the appropriate displacement-controlled stresses. The rotational degrees of freedom restraints at the surge nozzle DM weld node were removed and the equivalent rotation at that location approached 2 degrees. It was argued that since the limited experimental results on complex cracks showed slightly more than 2 degrees of crack rotation at maximum load, all of the displacement-controlled stresses would be relieved before the complex crack reached a critical state. However, the 2-degree rotation (from the displacement-controlled stresses) would displace the complex cracked pipe to a near critical state. Therefore engineering judgment dictates that the displacement-controlled loads must have an impact on the critical crack size, since rotation from these loads occur. In addition, not all complex cracks will fail at 2 degrees of crack rotation. Since no experimental data for complex cracks in Alloy 82/182 exists, the rotation at failure is unknown for these types of flaws.

In their second analyses (Appendix C of Ref. 2), detailed elastic and elastic-plastic finite element analyses were conducted on through-wall cracks in straight pipe of different lengths. The loads were applied with both bending moments and equivalent rotations. The comparison of the reaction moment (from the rotation runs) with the applied moments gave an indication of how much of the displacement-controlled bending moment was relieved by the compliance of the pipe. These results show that for a through-wall crack of 50% of the circumference with a simulated pipe system compliance equal to 60 feet of straight pipe, one half of bending moment was relieved. In addition, it was shown that at this point, the crack driving force was reduced significantly (still slightly above J_{Ic}, but still below critical). These results show that for the cases analyzed, the displacement-controlled stresses are relieved, but actual magnitude is dependent on the crack size and pipe system compliance.

[**] These data were generated through the international group programs, BINP and IPIRG, where participants other than the NRC funded this work

2.3   Leak rate modeling

The leak-rate calculations performed in the confirmatory calculations were conducted using the SQUIRT leak rate code. SQUIRT, which stands for Seepage Quantification of Upsets In Reactor Tubes, is a computer program that predicts the leakage rates for cracked pipes in nuclear power plants. The development of the SQUIRT computer model enables licensing authorities and industry users to conduct the leak-rate evaluations for leak-before-break applications in a more efficient manner. The SQUIRT code also includes technical advances that are not available in other computer codes currently used for leak-rate estimation. The SQUIRT code has been benchmarked against other leak-rate codes and validated against experimental results [13,14].

2.3.1   *The Henry-Fauske flow model in SQUIRT*

A review [15] of existing thermal-hydraulic models indicated that the Henry-Fauske model was the best currently available representation of two-phase fluid flow through tight cracks in a piping system. This model allows for non-equilibrium vapor generation rates as the fluid flows through the crack. The rate at which vapor is formed approaches the equilibrium value using an exponential relaxation correlation, with the correlation coefficients determined from the experimental data of Henry. In addition to the uncertainty associated with specifying the non-equilibrium vapor generation rate, other uncertainties in the analysis arise due to incomplete knowledge of the flow path losses, the friction factors for tight cracks, and the potential for particulate plugging.

2.3.2   *Other thermodynamic flow models*

The SQUIRT code has three different thermal-hydraulic flow models depending on the thermodynamic state of the fluid inside the pipe. The default model is the Henry-Fauske two-phase model for tight cracks for subcooled liquid as described above. The other two models are as follows.

1. Single-phase liquid model. A model was added to predict the leakage rate through a pipe crack when the fluid inside the pipe is under pressure, but the fluid temperature is below the saturation temperature corresponding to the ambient pressure outside of the pipe. In this case the fluid remains a liquid as it flows through the pipe crack and as it is discharged. This model solves the flow equations associated with non-compressible fluid flow.

2. Superheated single-phase steam model. A model was added to predict the leakage rate through a pipe crack when the fluid inside the pipe is superheated steam. By definition, superheated steam has a steam quality of 100%. In this case, the fluid remains a gas as it flows through the pipe crack and as it is discharged. This module solves the flow equations associated with compressible gas flow.

If the temperature of the fluid inside the pipe is less than or equal to the saturation temperature of the fluid at the ambient pressure, then the single-phase liquid flow model can be used to calculate a leakage rate. Alternatively, if the crack depth (pipe wall thickness) to hydraulic diameter ratio is less than 0.5, then the single-phase liquid model can also be used because the fluid is assumed to pass through the crack as a liquid before it has time to flash to a two-phase mixture.

If the temperature of the fluid inside the pipe is greater than the saturation temperature of water at the pipe operating pressure, then the superheated steam fluid flow model may be used to calculate the leakage rate. Under these circumstances, the steam quality is assumed to be 100% throughout the crack depth, and the fluid is modeled as a single-phase compressible flow.

Finally, if the crack depth (pipe wall thickness) to hydraulic-diameter ratio is greater than 15 (tight crack) and the fluid inside the pipe is a liquid, the fluid will flash to a two-phase mixture at the ambient pressure, and the Henry-Fauske two-phase flow model in SQUIRT may be used to calculate the flow rate. Figure 10 shows the critical pressure ratio as a function of the crack depth (pipe wall thickness) to hydraulic diameter ratio for two-phase flow. This figure also shows the region on the plot where the Henry-Fauske model is valid. Likewise, the figure also shows the region on the plot where the single-phase liquid model may be used to approximate the leakage rate. Finally, the current version of SQUIRT does not have a transitional two-phase flow model to handle pipe cracks with depth (pipe wall thickness) to hydraulic diameter ratios between 0.5 and 15. A sensitivity study was done in a previous study [14] and it was determined that at L/D=15, the single-phase model overpredicted the two-phase flow model by 30% for both large and small leak rates. This is within the normal scatter of leak rate data where the scatter was a factor of 2 (except at very low leak rates). Therefore, it was decided that for conditions where L/D<15, the all-liquid model should be used but the results should be scaled by a factor that would range linearly from 0.7 (at L/D=15) to 1 (at L/D=1).
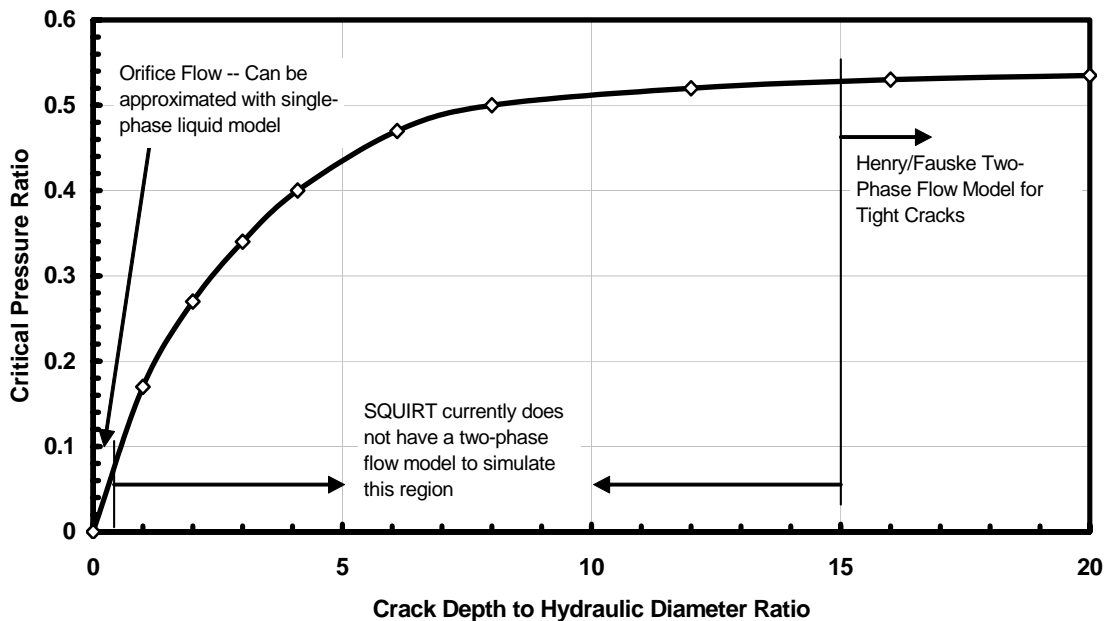
Figure 10 Plot of critical pressure ratio as a function of crack depth to hydraulic diameter ratio showing when the leak rate models in SQUIRT are valid [16]

2.3.3 Crack size assumptions

The SQUIRT code has two modules. SQUIRT2 calculates the leakage rate from a crack given the crack length, crack opening displacement (COD) and thermodynamic conditions. SQUIRT4 uses an iterative approach to calculate the crack length given the thermodynamic conditions, the material properties, and the leak rate. This iterative process uses typical J-estimation schemes to

predict the COD at a given condition. In this effort, since detailed FE analyses were conducted for each time step, the COD from those analyses were used with the SQUIRT2 module. In addition, SQUIRT2 allows the input of both the ID and OD crack length and COD. According to the SQUIRT user's manual [13], SQUIRT assumes that the behavior in both crack length and COD is linear between the OD and ID.

Since SQUIRT assumes that the behavior between the ID and the OD is linear, the results from the FE analyses can be used to determine the accuracy of this assumption. Figure 11 shows the normalized half COD (normalized by the half COD at the OD) for the relief nozzle geometry (Case 6, see Section 6 for details). In this figure, two different crack lengths are shown, and the results suggest that for the shorter OD crack lengths, the trend of COD through the thickness is not linear. However, as the OD crack length increases, the trend becomes linear. For the shorter crack lengths, the COD values are slightly less than the linear approximation, suggesting that the linear approximation would yield higher leak rates.
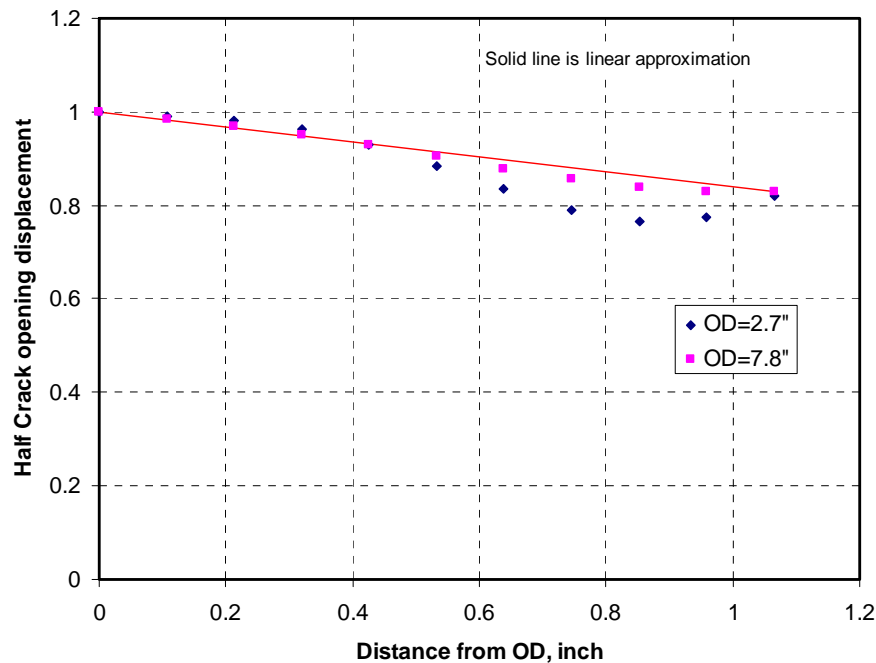
Figure 11 Normalized half crack opening displacement for Case 6

A much larger effect is seen when an approximation of the ID crack length is made. As described in Section 5 of this report, for most of these analyses, the resulting leaking crack was complex in shape in that the ID length extended completely around the circumference, and the OD crack length was limited in circumferential extent. An example of the profile for a leaking crack in Case 6 is shown in Figure 12a. In this figure, which shows half of the crack profile, the solid red line represents the leaking crack front with an OD crack length of approximately 3 inches. The purple dashed line represents the linear approximation in crack depth from the OD length to the full ID length. The blue dashed line represents the approximation that the ID crack length is equal to the OD crack length. In addition, Figure 12b shows the COD profile for this same crack. These figures suggest that the approximation of the ID crack length equal to the ID circumference is overly conservative for full extent complex cracks, i.e., too large of a flow path

13

is assumed, while the approximation that the ID and OD crack length being equal may be too restrictive. Since there is no available complex crack leak rate experimental data that can be used to verify these predictions, it can only be assumed that the actual leak rate will fall between these two bounds. Therefore, for the purposes of these analyses, leak rates at both conditions were calculated and averaged.

| (a) Crack shape | (b) Numerical COD |

Scale = inch
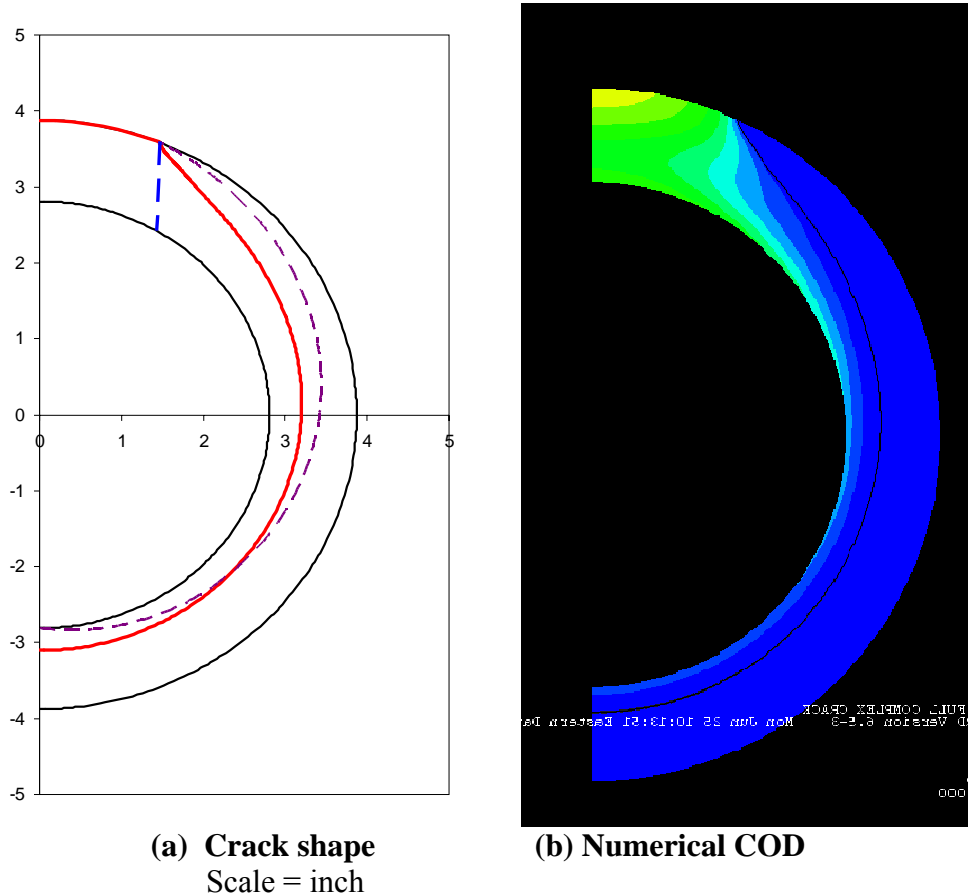
Figure 12 Crack length approximations for SQUIRT calculations

2.3.4   *Crack morphology parameters*

The SQUIRT code contains a COD-dependent crack morphology model for leak-rate calculations. This model is described in detail in References 17 and 18. In essence, this model assumes that the pressure drops that occur as the fluid passes over the crack morphology are dependent on the opening of the crack. The effect is simply illustrated in Figure 13. For large values of COD, the fluid passes directly across the global roughness, which induces the pressure drops. However, if the COD is small, the fluid must weave around the grain boundaries and the pressure drops are dominated by the change in flow path and local grain surface roughness. The relationships between these effects are given in detail in Reference 18 and are fully encoded in the current version of SQUIRT. Even though this procedure has not been fully validated experimentally, computational fluid mechanics work [19] suggests that this procedure is appropriate for modeling the pressure loss across tortuous crack morphologies.

14
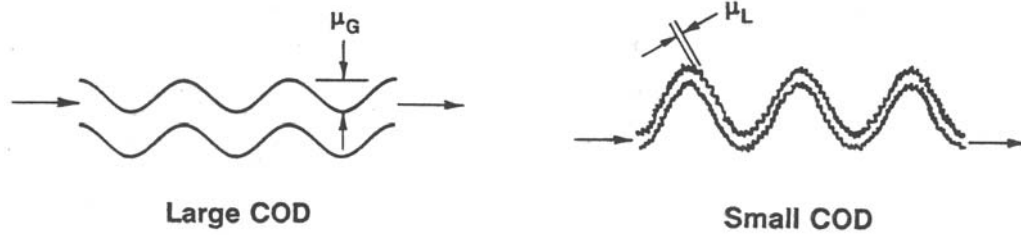
Figure 13 Effect of COD on crack morphology parameters

Within the current version of SQUIRT, the key crack morphology parameters are:

μ_L - Local roughness,
μ_G - Global roughness,
n_{tL} - Number of turns in flow path when the crack is tight ($\delta/\mu_G < 0.1$),
K_G - Global path deviation factor, ratio of flow path to pipe thickness, and
K_{G+L} - Local path deviation factor, ratio of flow path to pipe thickness.

The SQUIRT code has three types of cracking mechanisms:

IGSCC   -   Intergranular stress corrosion crack,
Fatigue   -   Fatigue crack, and
PWSCC   -   Primary water stress corrosion crack.

Table 1 gives the mean values of the crack morphology parameters for the three different crack mechanisms as determined from cracks removed from service. For the analyses conducted in this effort, the PWSCC crack morphology parameters with the COD-dependence behavior were used.

Table 1 Mean values of crack morphology parameters used in SQUIRT (from Ref. 20)

Crack Morphology Variable	IGSCC	Fatigue	PWSCC[††]
μ_L, μm	4.699	8.814	16.86
μ_G, μm	80.010	40.513	113.9
n_{tL}, mm⁻¹	28.2	6.73	5.94
K_G	1.07	1.017	1.009
K_{G+L}	1.33	1.06	1.243

[††] For PWSCC these values are for cracks that are traveling parallel to the dendritic grain structure, see Reference 20

3. K-Verification and Model Convergence Results

3.1 Description of Analyses

As described in Section 2 of this report, the subcritical crack growth that is calculated in this effort is driven by the stress intensity factors at every crack tip (nodal) location along the crack front. The same basic procedure is used in both PipeFracCAE and the industry code FEACrack. Therefore, it is essential to verify the K-solutions from both the Emc^2 and DEI computer codes. In the present effort, three different cases were considered. First, a semi-elliptical (idealized) surface crack under tension, bending, and internal pressure was considered. The Emc^2 and DEI K-solutions were compared and these solutions were also compared with the Anderson [21] solution. In addition, a semi-elliptical surface crack under tension, bending, internal pressure, and welding residual stress was considered. As a final step, an arbitrary (non-idealized) surface crack under tension, bending, and internal pressure was considered.

In addition to the K-verification, model convergence studies were conducted. For this study, the time increment was varied for the crack growth analyses. The time and crack shape at leakage was compared.

3.2 K-Verification

3.2.1 *Semi-elliptical surface crack under tension, bending, and internal pressure*

In order to verify the stress intensity solutions along the crack front for semi-elliptical surface cracks, FE analyses were performed for models only with internal pressure, axial tension, and bending moment (no WRS). These results were compared with the Anderson [21] solution and the results provided by DEI in their Phase I effort [22].

Table 2 lists the four cases considered in this effort, where the outer pipe diameter, D_o = 7.75 inches and the wall thickness, t = 1.29 inches. These cases were selected from a subset of the 36 DEI analyses that most closely matched conditions for the Wolf Creek cases considered.

The mesh generator developed by Emc^2, PipeFracCAE, was employed to generate the FE model. Figure 14 shows an example mesh generated from PipeFracCAE. A quarter symmetric model was used. Twenty-noded brick elements were used for the model. The crack tip elements were collapsed at the crack front and the midside nodes nearest the crack tip were moved to the quarter point location to generate the $r^{(-1/2)}$ singularity at the crack tip.

Table 2 Crack geometries of four cases considered for validation

Case	R_i/t	a/t	a	$2c_i/a$	2θ (deg)
3	2.004	0.1	0.129	15	42.9
15	2.004	0.3	0.387	5	42.9
18	2.004	0.3	0.387	21	180.1
20	2.004	0.3	0.387	30	257.3

Below are the loading conditions used in this effort:

- internal pressure : 2.235 ksi
- axial tension : 2.0 ksi
- effective global bending moment : 277.5 in-kips

The internal pressure was applied to the inner surface of the pipe and also 100% of the internal pressure was applied to the crack face to simulate crack-face pressure loading. Axial tension and a bending moment were applied at the end of the pipe as a pressure loading.

The elastic modulus and the Poisson's ratio were set to 30×10^6 psi and 0.3, respectively.

The stress intensity factor, K, was directly obtained from ABAQUS. In ABAQUS, the interaction integral method [23] is used to extract the K values. The K_I value was determined as the mean value of the 2nd to 5th contours along the crack front.

Figure 15 shows the K values along the crack front for the four cases considered in this effort. In this figure, results provided by DEI are also plotted for comparison. As shown in Figure 15, the two results match well along the crack front except near the free surface. Since it is difficult to numerically calculate the K value at the free surface point, the K value is typically extrapolated from the K values near the free surface. In their Phase I effort, DEI linearly extrapolated the path independent J-integral values near the free surface for the points where the path dependence was high. These results are shown in Figure 16. As shown in this figure, the extrapolated K values do not follow the trends of the previous K values along the crack front. Figure 16 also shows the K values calculated by Emc^2, where the J-integral path independence was valid very close to the free surface (difference was less than 5%). This was possibly due to the fine mesh used near the free surface [see Figure 14(c)]. The K value at the surface point was extrapolated by using a 4th order polynomial fit. Table 3 compares the K values at the free surface and the deepest points calculated by DEI and Emc^2 and also these values are compared with the Anderson solution. As summarized in Table 3, the K values agree well at the deepest point whereas the values at the free surface location show some difference. Such difference is due to the different extrapolation method used to estimate the K value at the free surface.

17
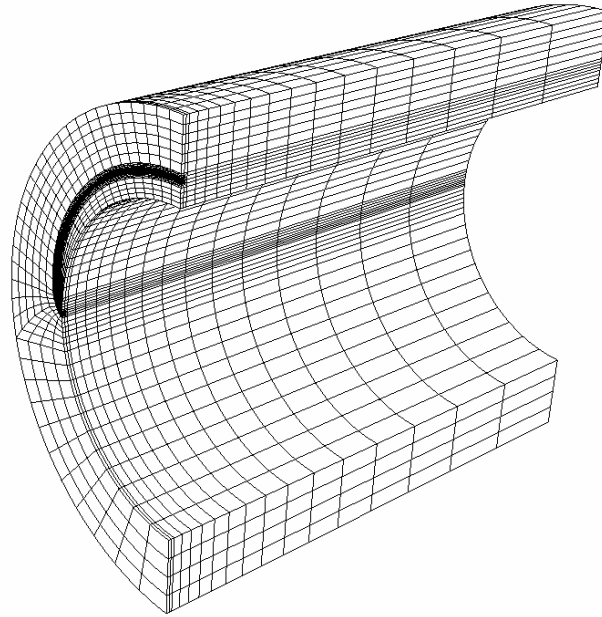
(a) Overall view
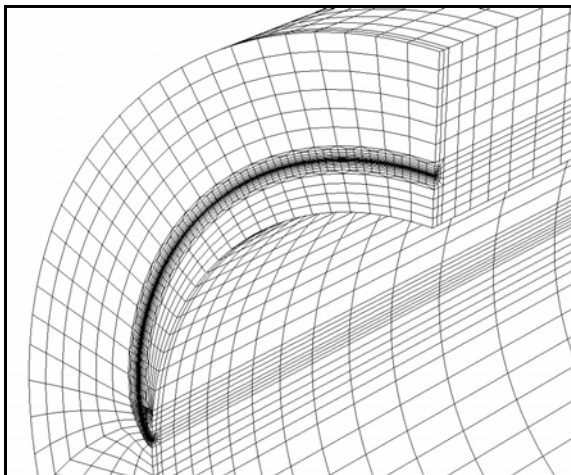
(b) Close-up view near crack front
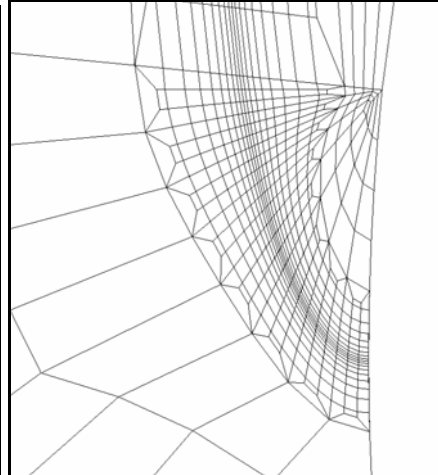
(c) Close-up view near surface point

Figure 14   Example of FE mesh employed in the present study (Case18)
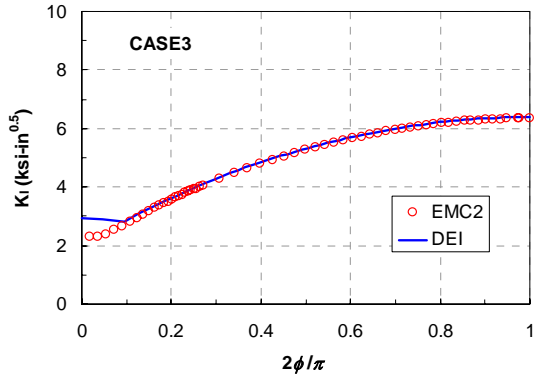
(a) Case 3
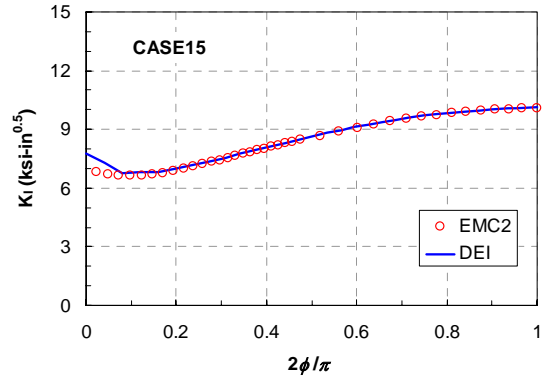
(b) Case 15
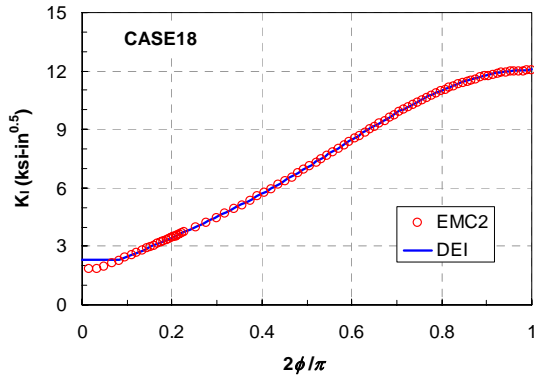
(c) Case 18
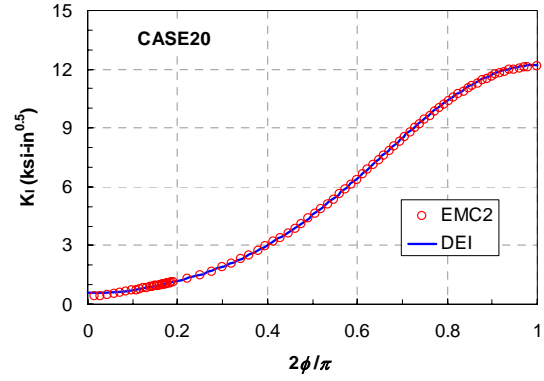
(d) Case 20
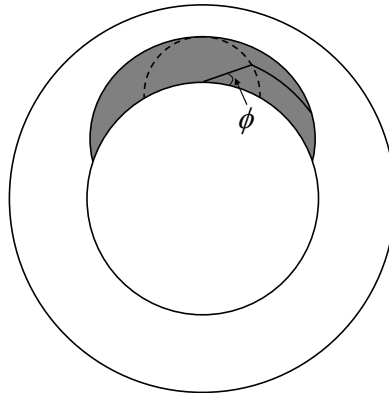
(e) Definition of angle (ϕ) along the crack front

Figure 15 Calculated K values along the crack front

(a)

(b)

(c)

(d)
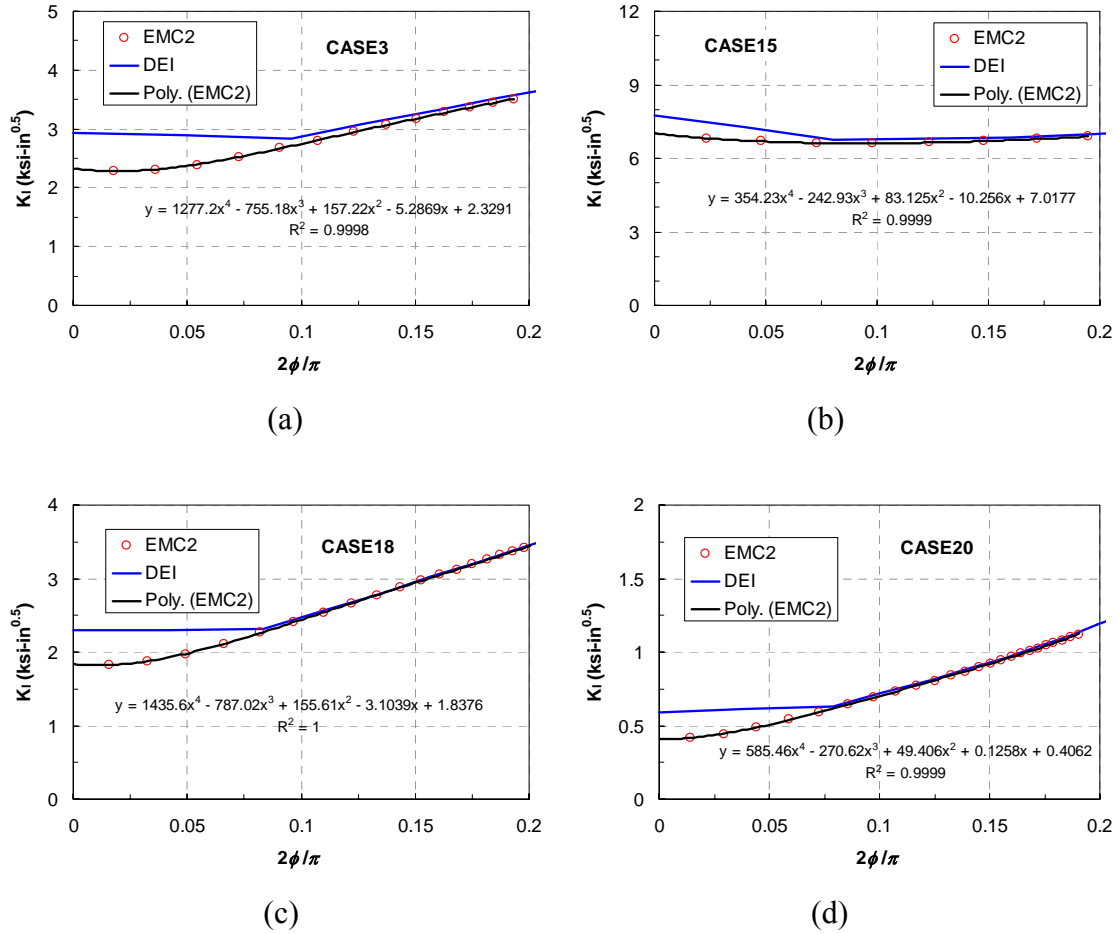
Figure 16 Extrapolation of K value at the surface point

Table 3   Comparison of K_I values at surface and deepest points

	Anderson	**(ksi-in$^{0.5}$)**	**DEI**	**(ksi-in$^{0.5}$)**	**Emc^2**	**(ksi-in$^{0.5}$)**
	K_{surf}	**K_{deep}**	**K_{surf}**	**K_{deep}**	**K_{surf}**	**K_{deep}**
Case3	2.6	6.2	2.9	6.4	2.33	6.35
Case15	7.2	9.9	7.8	10.1	7.02	10.05
Case18	2.4	12.2	2.3	12.1	1.84	12.01
Case20	1.5	13	0.6	12.2	0.41	12.14

3.2.2 *Semi-elliptical surface crack under tension, bending, internal pressure, and welding residual stress*

As part of the K-verification, FE analysis was conducted for the indication found in the Wolf Creek relief nozzle DM weld. The purpose of this effort was to verify the stress intensity solutions along the crack front for an idealized crack (semi-elliptical crack) in a complex stress

20

field, i.e., tension, bending, internal pressure, and welding residual stress. All of the geometry, loads, and assumptions are identical to those presented in DEI Phase I report [22], except for those presented below. For these analyses, PipeFracCAE was employed to generate the FE model where the semi-elliptical crack was modeled using the arbitrary crack-front option. The model generated for this analysis is shown in Figure 17.
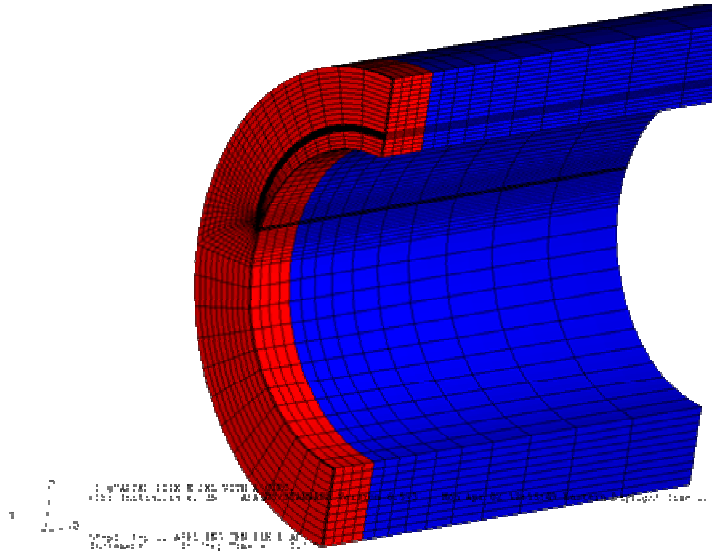
Figure 17   FE model used for K-verification of semi-elliptical surface crack under complex stress field

In the DEI Phase I analyses, the WRS field initially developed by Emc^2 for the relief nozzle flaw[‡‡] was simulated numerically through an elastic FE analysis by imposing a temperature field on the crack plane and in the weld metal. In their analyses, a constant temperature was imposed on all nodes from the crack plane to the end of the simulated weld, which had an axial location of 1 inch from the crack plane. The coefficient of thermal expansion was then modified by nodal location until the required stress field was obtained. For the material outside of the weld, the thermal expansion coefficient was set to zero. This allowed the stress to relax and return to zero far from the crack plane. This numerically simulated stress field was added to the normal operating conditions, and was used to drive the crack in their Phase I analyses.

In order to verify these calculations, Emc^2 conducted similar analyses. However, the development of the stress fields was handled in a slightly different manner[§§]. In this case, the entire FE model had the same coefficient of thermal expansion, but the temperature field was adjusted to produce the required stress field at the crack plane. The temperature field at the crack plane was used at every axial location from the crack plane to the end of the simulated weld, i.e., 1-inch away from the crack plane. Beyond the 1-inch location, the nodal temperatures were set to the initial condition.

[‡‡] This WRS was based in ASME Section XI efforts for IGSCC cracking in the HAZ of stainless steel welds
[§§] Note that in later analyses, DEI adopted the Emc^2 procedure for applying the thermal loads in the crack growth analyses

Figure 18 shows the stress field at the crack plane. In this figure, the x-axis is the normalized distance from the ID surface, while the y-axis is the axial welding residual stress. The solid line in this figure represents the stress field used in the original NRC scoping analyses. The dashed line represents the DEI simulated WRS field. Note that the stress on the ID is underpredicted, at 30% though-wall is overpredicted, and at 80% through wall is again underpredicted. The solid squares in this figure represent Emc^2 predictions of the WRS (Case 1). Finally, the open triangles represent the Emc^2 estimate of the DEI calculated WRS (Case 2). In this case, we attempted to match the DEI predictions and not the original curve fit from the scoping analysis.
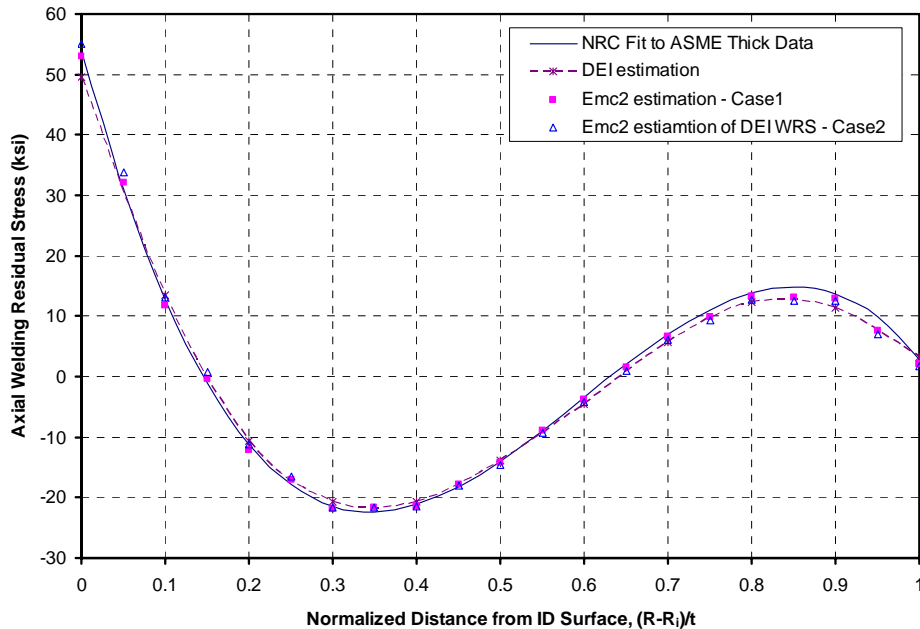
Figure 18 Welding residual stress field at the crack plane

Figure 19 illustrates a comparison of the K values for the semi-elliptical surface flaw as a function of pipe circumferential position relative to the symmetry plane for the three residual stress cases shown in Figure 18.   Note that for the Emc^2 Case 2 results, the residual stresses were generated to match the DEI simulated stresses as closely as possible, where for the Case 1 results, the residual stresses were generated to match the original stresses used in the scoping analyses. When the Emc^2 welding residual stresses match those of DEI, the K-values are very similar along most of the crack front, but deviate slightly at the free surface. However, when the Emc^2 WRS matched those of the original scoping analysis, the Emc^2 K-values were lower than the DEI values by about 13% along the entire crack front.
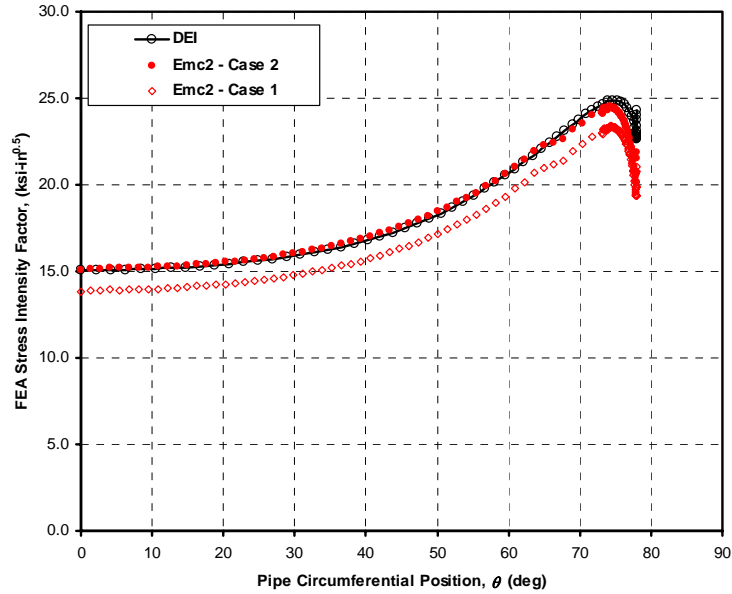
Figure 19 Comparison of DEI and Emc^2 K-solution for semi-elliptical surface crack in relief nozzle

A closer view of the K-values at the free surface is shown in Figure 20. As shown in this figure, the results compare well until the transition to the free surface begins. At the free surface, the K-values vary by about 15%. It is suspected that this difference is due to the estimation of the welding residual stress since the comparison of K-values for semi-elliptical flaws under only membrane and global bending loads showed excellent agreement between the Emc^2 and DEI results.
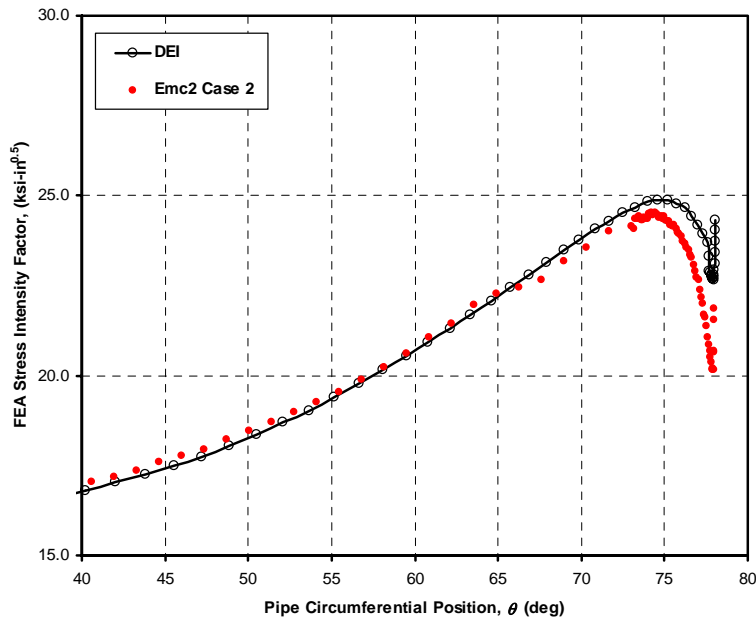
Figure 20 Comparison of K-solution at free surface

The effects of stress redistribution can be examined by the results shown in Figure 21. In this figure, the symbols represent the K values from the Emc^2 analyses where temperature was used to predict the welding residual stress at the crack plane and the decay of that stress along the axial length of pipe. The solid line in this figure, represents the application of the crack plane residual stress field at the end of model, i.e., the residual stress does not decay with axial distance. As shown in this figure, the K-values are identical which indicate that for this size crack in this residual stress field, redistribution has no affect on the driving force.
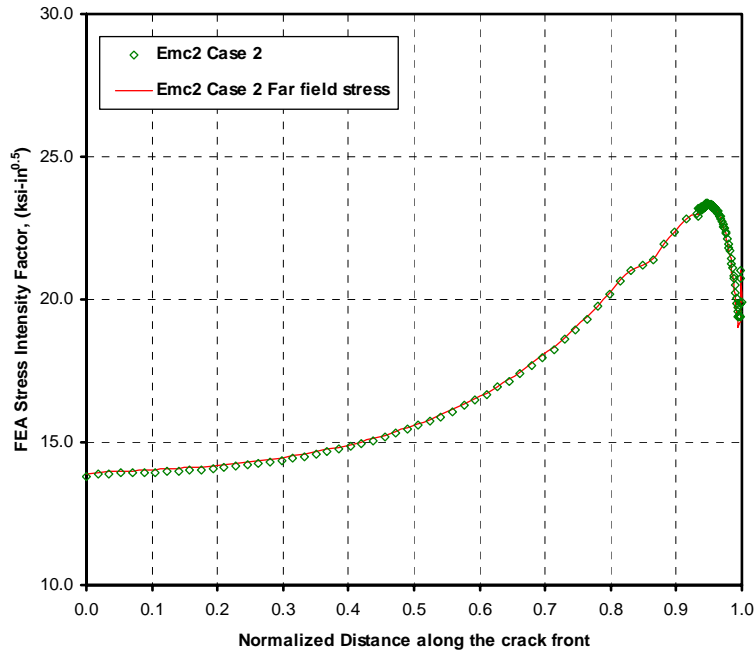
Figure 21 Effects of residual stress redistribution

3.2.3   Arbitrary surface crack under tension, bending, and internal pressure

As final step of K-verification, continuous, non-ideal crack fronts were generated using a modified Bessel function to verify the K-solutions from both the Emc^2 and DEI computer codes. These crack fronts are shown in Figure 22. In this figure, the "alpha" term is the order of the Bessel function. Also included in this figure is an additional crack front (Extra Case) suggested by DEI that is still continuous but much less ideal as compared to the Bessel function. For these verification analyses, the Wolf Creek relief line geometry and loads were considered. No welding residual stress was used in these analyses. Figure 23 shows the four crack front shapes on the Wolf Creek relief line geometry.
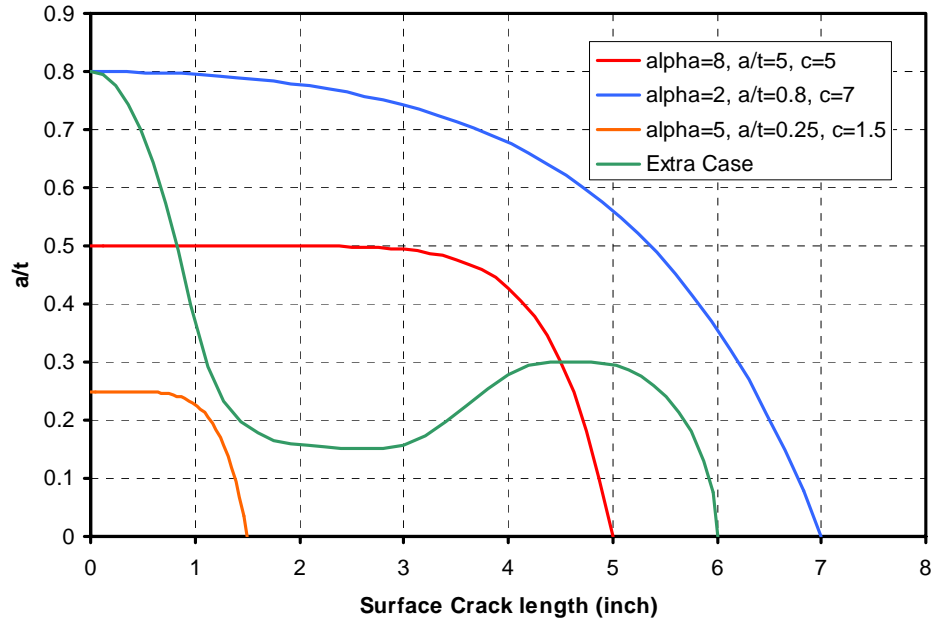
Figure 22 Crack fronts suggestged for the K-verification study
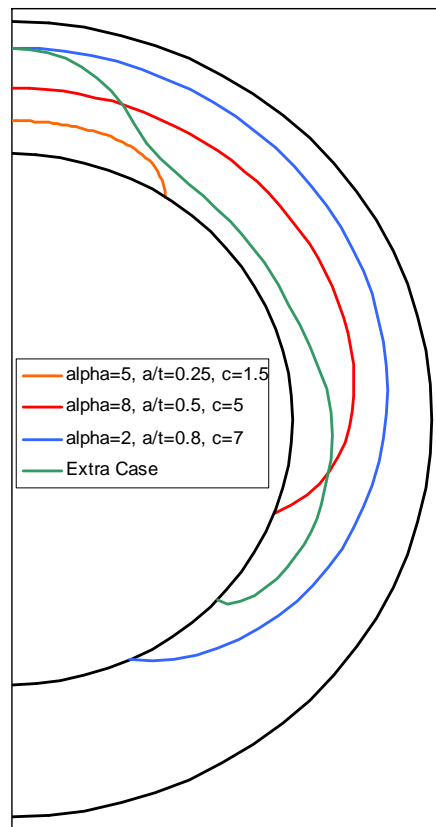
Figure 23 Crack front shapes on Wolf Creek Relief nozzle geometry

Using PipeFracCAE and ABAQUS, the K-solutions for these cracks were generated along the crack front as shown in Figure 24. In this figure, results provided by DEI are also plotted for comparison. As shown in this figure, the comparisons are excellent between the two independent calculations.
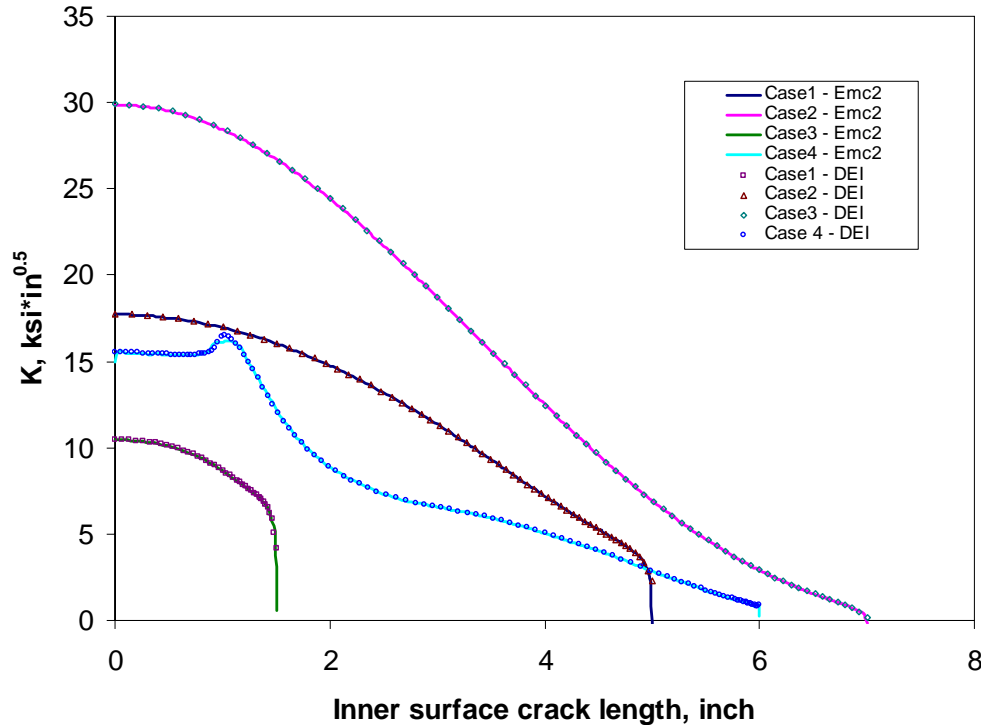
Figure 24 Comparison of Emc^2 and DEI K-solutions for K-verification study

3.3   Model Convergence

In order to verify that the inputs used in the crack growth analyses were producing a converged solution, a model convergence study was completed. In the Emc^2 analyses, the crack growth is controlled not only on time, but also on maximum crack extension per increment. For instance, a one month time step can be used with 0.05-inch crack growth increment. In this case, the crack will be grown for one month at the specified inputs, however, if that growth exceeds 0.05 inch, the time step will be reduced until it does not exceed that value. For this study, the Phase I case (See Section 5.1) was run with a time increment of 1 month and 0.25 month. In these cases, the average crack growth increment was 0.09 inch and 0.02 inch respectively. The results of the crack growth predictions are shown in Figure 25. This figure illustrates that there are some slight differences in crack growth, but the times to leakage only differed by about 3%, which is slightly better than the 5% claimed by DEI in their convergence study. Therefore, it is assumed that the model is converged within these time and crack growth increments.
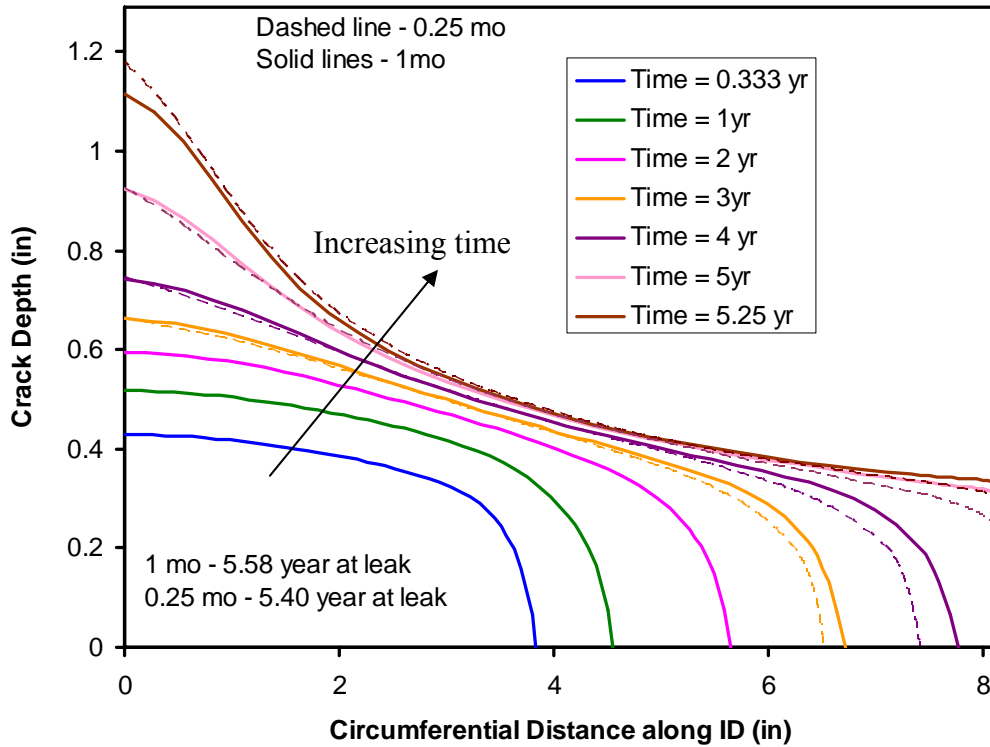
Figure 25 Time increment comparison for Phase I calculations

4. Welding Residual Stress Results

In this section of the report, the confirmatory welding residual stress analyses are discussed. As described in the industry's report [2], the welding residual stress analyses conducted were chosen to investigate the range of nozzle to safe end welds in the as-welded conditions and in the presence of weld repairs. All of the geometry and welding details were retrieved by the industry through a survey conducted as part of the industry's effort. For the confirmatory analyses presented here, the geometries used were identical to those used by the industry; however, the material properties, mesh development, and analysis procedures were unique.

4.1   Description of Cases

The nozzles analyzed in this effort consisted on the pressurizer surge, relief/safety and spray nozzles. For the nine plants affected by the possible acceleration in inspection/mitigation schedule, seven were Westinghouse designs, while the remaining two were CE designs. Therefore, in the analyses conducted both Westinghouse and CE designs were considered.

For the safety/relief nozzle cases, two geometries were used in the modeling effort. These geometries, labeled Type 1a and Type 2b [2] represent the typical relief/safety geometry with and without an ID liner. For the purposes of the confirmatory analyses, the Type1a geometry was chosen in this effort. The industry conducted the following cases with the relief/safety nozzle geometry.

- Nozzle butt weld alone with and without safe-end weld,

- Nozzle butt weld with weld buildup at safe end ID with safe-end weld,
- Nozzle butt weld with liner fillet weld with safe-end weld,
- Nozzle butt weld with 0.75-inch deep x 360 degree ID weld repair (3D solution) without safe end weld, and
- Nozzle butt weld with 0.75-inch deep x 20 degree ID weld repair with no safe end weld.

In the industry's analyses, it was assumed that the safety/relief analyses were representative of the smaller spray nozzle welds; therefore, no spray nozzle analyses were conducted.

For the surge nozzle, two geometries were also considered, i.e., Type 8 and Type 9 [2] with the following analyses conducted:
- Type 8 nozzle butt weld alone with and without the stainless steel safe-end weld,
- Type 8 nozzle butt weld with 5/16-inch x 360 degree ID weld repair with the safe-end weld, and
- Type 9 nozzle butt weld alone without the safe-end weld.

The Emc^2 confirmatory analyses focused on the Type 1a safety/relief nozzle with and without the stainless steel safe-end weld and the Type 8 surge nozzle with and without the 5/16-inch repair and with and without the safe-end weld. These analyses were conducted in a purely axi-symmetric manner, which assumes that the resulting residual stresses do not vary circumferentially.

4.2 Description of Emc^2 analysis procedures

Emc^2 has been conducting welding simulation analyses for years and is the main NRC contractor conducting welding simulations for the J-welds in CRDM nozzles. The approach used in the predictions of welding residual stresses and strains is based on extensive knowledge of the welding process and has been refined as the commercial finite element codes have been updated and improved. In all of the Emc^2 welding analyses, thermo-elastic-plastic FE simulations were performed to simulate welding the subject butt welds. The formation of the welding residual stress is a result of the thermo-mechanical deformation process during welding. In this study, the heat flow and mechanical deformation during welding were simulated using a sequentially coupled approach [24,25,26]. In such approach, the transient heat-transfer analysis was conducted to solve the temporal and spatial distribution of the temperature in the model, and then the computed thermal history was used as input as thermal loading in the subsequent mechanical analysis calculating the residual stress field. Temperature-dependent mechanical properties were utilized and isotropic hardening was assumed. The effects of melting, solidification, and annealing were simulated in the analysis. Heat transfer to the environment is assumed to occur on all free surfaces of the model. The justifications of the sequentially coupled modeling approach were provided elsewhere [11, 27,28].

The welding heat flow was modeled as a heat-conduction problem. Temperature-dependent thermal conductivity and specific heat values were used. Typically, the welding arc is treated as a volumetric moving heat source, taking the double-ellipsoidal distribution proposed by Goldak et al. [29]. However, such moving source analyses can be very computationally intense [30]. In the axisymmetric models assumed in this effort, the welding heat was effectively applied simultaneously over the weld length.

The welding simulation was performed on a pass-by-pass basis following the weld sequence described for butt weld. A weld pass was activated only when it was deposited. The analysis procedure included not only the pass-by-pass welding steps, but also other essential fabrication steps that would be expected to have strong effects on the stresses in the butt weld: back chipping, last pass welding, hydrotesting, and application of operating temperature.

As mentioned, temperature-dependent material properties were used for simulating welding residual stress, including the thermophysical and mechanical properties of the materials involved in butt weld fabrication. Great care was taken to ensure that the material properties used in the weld simulation analysis were as realistic as possible. The material properties necessary for the butt weld stress analysis were collected from various sources in the open literature and through data exchanges with industry. These data were originally developed for the CRDM effort conducted at Emc[2] [31]. In addition, the temperature-dependent stress-strain curves for Alloy 182 solution-annealed weld metal [up to 1,255°K (1,800°F)] and carbon steel SA-508 [up to 1,033°K (1,400°F)] were experimentally determined at ORNL through that CRDM effort. Table 4 shows a summary of the mechanical properties at 315C. An example of the temperature dependent stress-strain curves for the Alloy 182 material is shown in Figure 26.

Table 4 Mechanical properties for Emc[2] weld analyses at 315C

Material	Use	Elastic Modulus, GPa	Poisson's Ratio	σ_y, MPa
SA-508	Nozzle	183.15	0.30	268.9
Alloy 182	Weld and butter	203.16	0.32	162.8
SS309/304/316L	Cladding, SS weld, Safe end	176.29	0.30	148.8
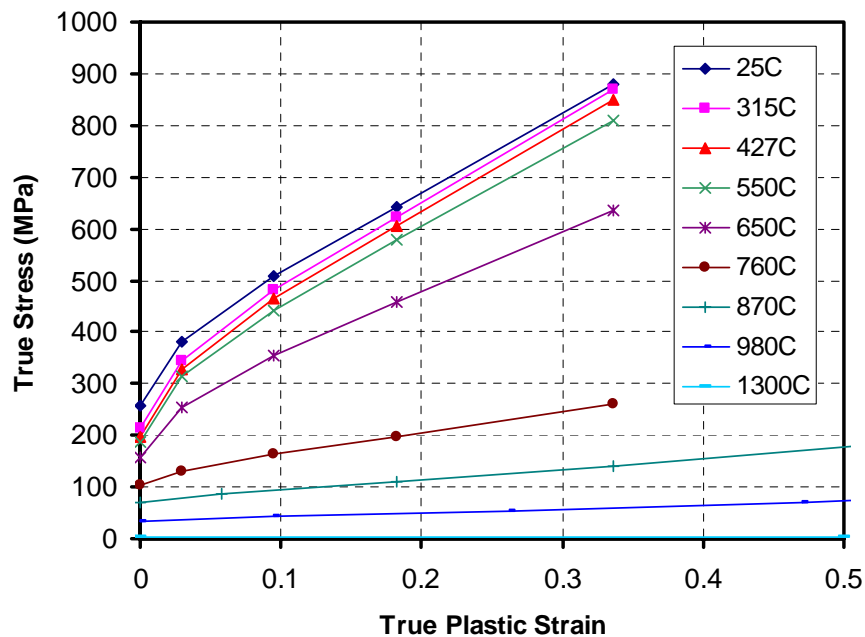
Figure 26 True stress-strain curves for Alloy 182 weld metal

4.3 Modeling assumptions

In all of the welding analyses conducted in this program, modeling assumptions were necessary. Since the exact details of the welding procedures were not available, these assumptions were necessary in order to complete the analyses. The following assumptions were used in all analyses:

- An axi-symmetric assumption was used for all welds in the Emc^2 study.
- Typical size weld beads were simulated in all cases. The size of the weld beads was developed from investigation of micrographs of other similar welds. The number of weld passes was generated from the dimensions and the typical weld bead size. DEI assumed a different weld bead size, see Figure 27.
- The effects of the butter welding and post-weld heat treat were ignored. It was assumed the butter was in a stress free state when the main welding occurred. DEI made the same assumption. This is a reasonable assumption since past work [11] has shown that after welding and post-weld heat treatment, the stresses in the butter are typically small.
- All of the welds modeled were U-groove type welds, i.e., the butter and the safe end butted together with a 0.07-inch land, which was melted when the first weld pass was deposited. This land was later removed by a back chipping process and a last pass weld was re-deposited on the ID. In these analyses, it was assumed that this land was 0.1-inch inches for all nozzles. The land was not modeled for the stainless steel safe-end welds.
- The back chipping process for land removal and repair process was numerically simulated using an element removal process. The effect of grinding/cold work due to this process was not simulated.
- A linear spring was used at the end of the stainless steel pipe to simulate the stiffness of the remaining pipe system. The stiffness used corresponded to a length of approximately 60 feet.
- Isotropic hardening was used in all analyses.

(a)   **(b)**
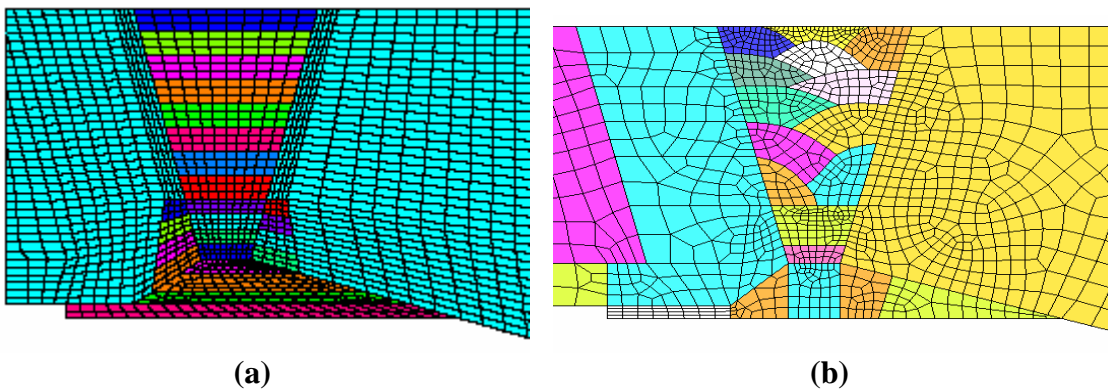
Figure 27 Comparison of DEI (a) and Emc^2 (b) WRS mesh for surge line illustrating weld bead geometry

4.4 Relief nozzle results

The geometry for the Type 1a relief nozzle was provided to Emc^2 by DEI and is shown in Figure 28, while the axi-symmetric finite element model generated is shown in Figure 29.

Figure 28 Geometry for the relief nozzle WRS analyses
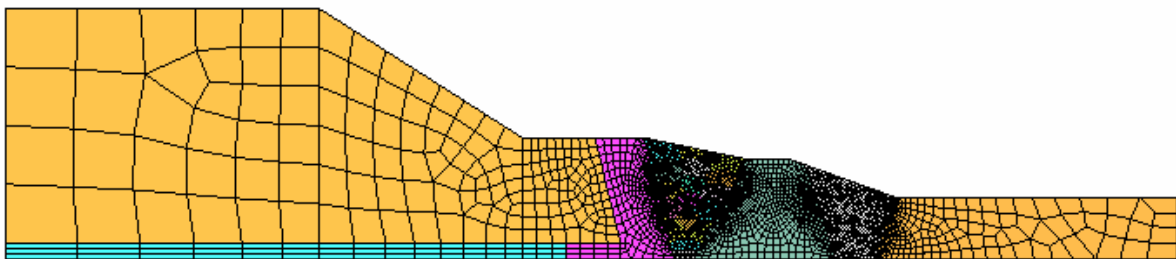
Figure 29 Emc^2 relief nozzle mesh

In addition, the details of the mesh for both the main DM weld and the stainless steel safe-end weld are shown in Figure 30. In this figure, each weld pass is given a separate color so that the weld pass details are illustrated.

The following sequence was followed in the relief nozzle welding simulation analyses:
- Each pass of the main DM weld was deposited from the ID to the OD in a left-to-right sequence.
- The land (0.1") was removed from the ID using an element removal technique.
- The last pass was deposited on the ID in one weld pass.
- The stainless steel weld was deposited from the ID to the OD in a left-to-right sequence. (Note this step was omitted in some of the analyses).

31

- A hydrotest was simulated at a pressure of 2,794 psi (1.25*2,235 psi) at ambient conditions.
- The model was then taken to operating temperature (653F).

| (a) Main weld | (b) Stainless steel safe end weld |
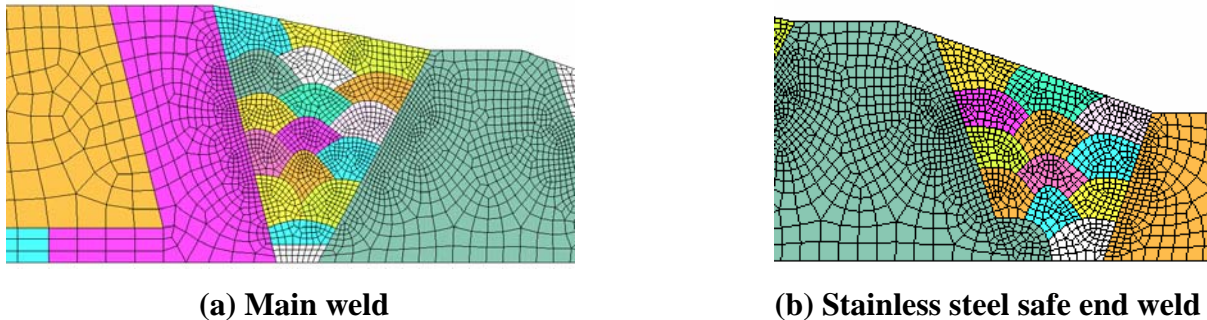
Figure 30 Emc^2 relief nozzle weld mesh details

For the relief nozzle analyses, the cases with and without the stainless steel safe-end weld were considered. In addition, since the analysis in this report deals with circumferential crack growth, only axial stresses are reported. An example of an axial stress (in MPa) contour plot for the relief nozzle case without the stainless steel safe-end weld is shown in Figure 31. This figure illustrates that high ID axial stress is in the butter adjacent to the DM weld. The arrow shown in this figure represents the linear path that best approximates the maximum stress path. This arrow goes through the highest tensile stress on both the ID and OD, while going through the smallest compressive stress at the mid thickness. This path will be used to compare axial stresses for the other relief nozzle runs.

A comparison of the axial stresses from the DEI (open symbols) and Emc^2 (solid symbols) analyses for the relief nozzle are given in Figure 32. Also included in this figure are the residual stresses assumed in the original scoping study. A comparison of the welding residual stresses without the stainless steel safe end weld for the DEI and Emc^2 analyses can be made by comparing the open symbols in Figure 32.   These results indicate that the stresses are similar when the analysis is conducted without the stainless steel safe-end weld. In fact, the Emc^2 stresses are slightly higher on the compressive side, but slightly lower on the tensile side. In addition, the Emc^2 stress field crosses from tension-to-compression at a slightly higher through-thickness location, suggesting that it may be slightly more limiting in a crack growth sense.

The results with the stainless steel safe-end weld modeled are given by the solid symbols in Figure 32. For these results, it appears that there is a large difference between the ID stresses for the Emc^2 and DEI analyses when the safe end weld is added. The DEI results show a tensile stress of over 200 MPa on the ID surface, while the Emc^2 results show a slight compressive stress. However, the results are very similar through-out the rest of the wall thickness. It is suspected that the difference is due to the safe-weld weld modeling. In the Emc^2 analyses, a linear spring is added to the end of the stainless steel pipe to represent the compliance of the piping system. It is assumed that the piping system is a straight section of pipe. In the DEI analyses, no piping system compliance is modeled, but the nodes at the end of the stainless pipe are coupled in the axial direction. This procedure models the pipe movement as if the pipe was continuous, but does not estimate the system compliance. Since the addition of the stainless steel

weld creates through thickness bending, the piping system compliance will be important. However, at this point, further analyses would be required to determine the differences shown in ID stress. In addition to the system compliance, other issues, such as the stainless steel weld sequencing, may affect the stress in the DM weld.
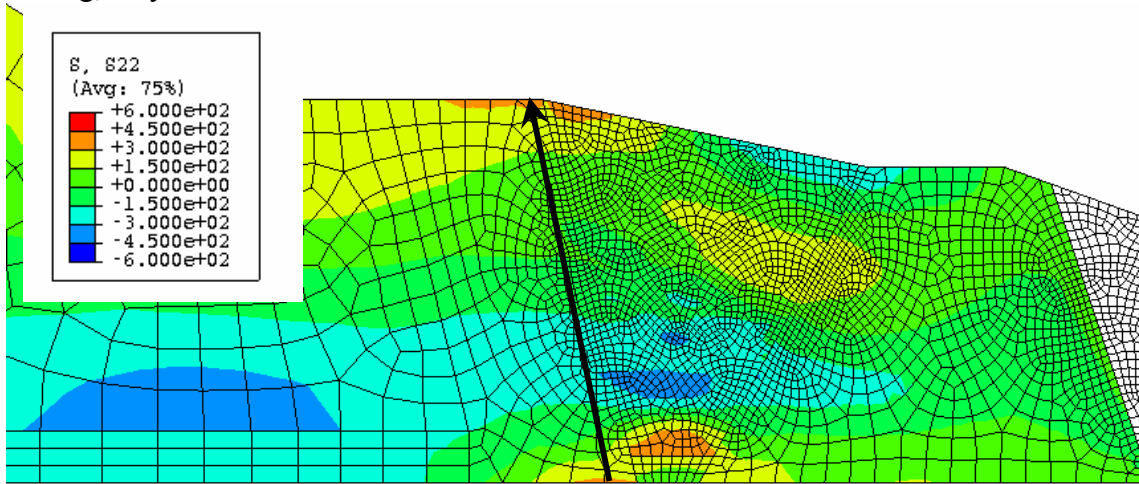
Figure 31 Axial stress for relief nozzle case without stainless steel weld at 653F (Arrow is maximum stress path)
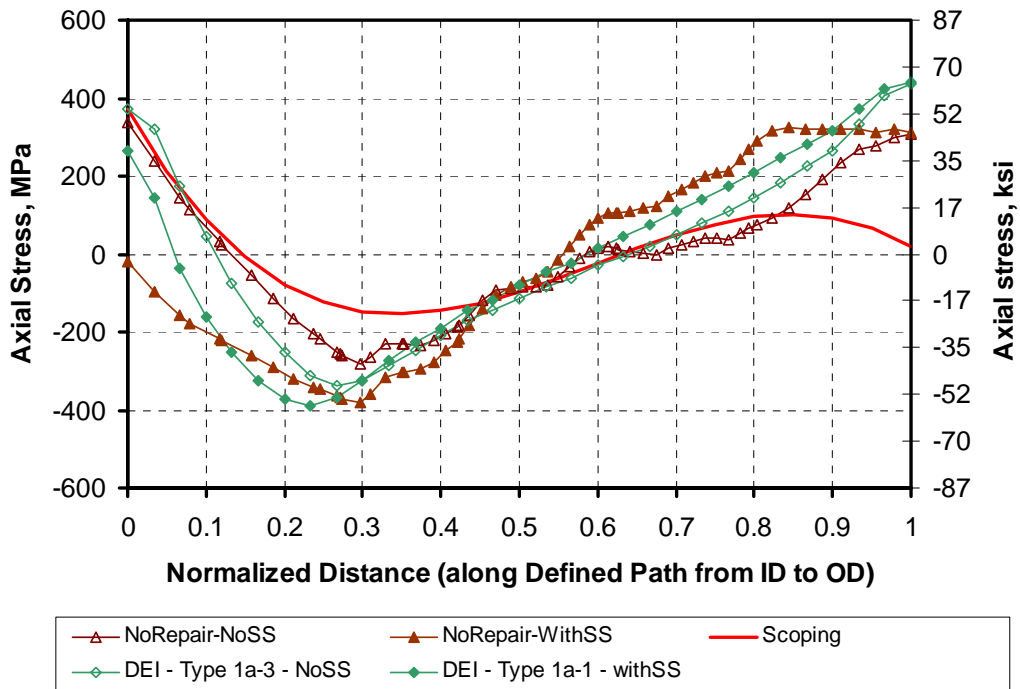
Figure 32 Comparison of axial stress results for relief nozzle case (Triangle symbols = Emc^2, diamond symbols = DEI)

4.5 Surge nozzle results

The geometry for the Type 8 surge nozzle was provided to Emc^2 by DEI and is shown in Figure 33, while the axi-symmetric finite element model generated is shown in Figure 34.
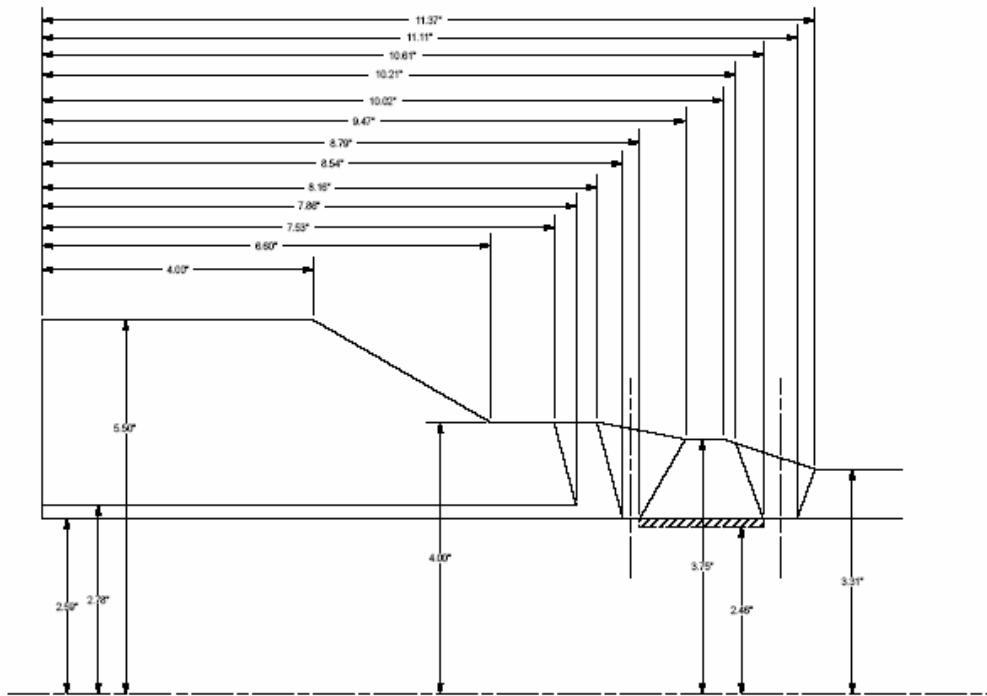
The details of the Emc^2 mesh for both the main DM weld and the stainless steel safe-end weld are shown in Figure 35. In this figure, each weld pass is given a separate color so that the weld pass details are illustrated. In addition, the section highlighted in Figure 35a represents the area removed for the repair analysis.
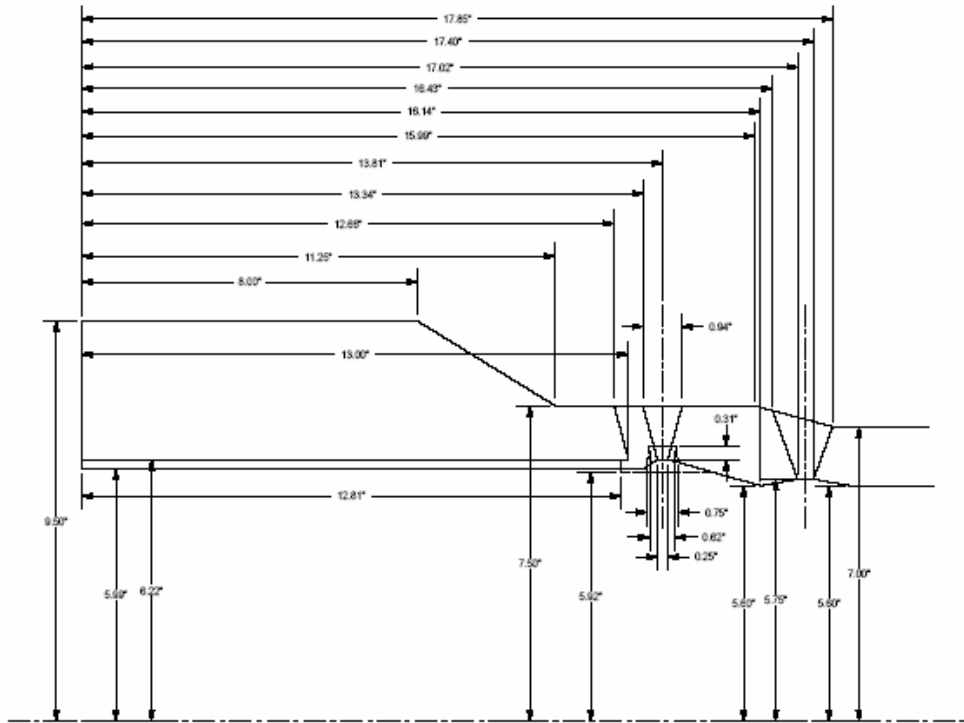
Figure 33 Geometry for the surge nozzle WRS analyses
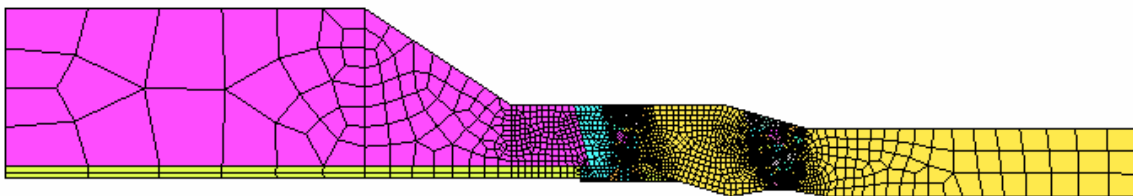
Figure 34 Emc^2 surge nozzle finite element model

(a) Main weld   **(b) Stainless steel safe-end weld**
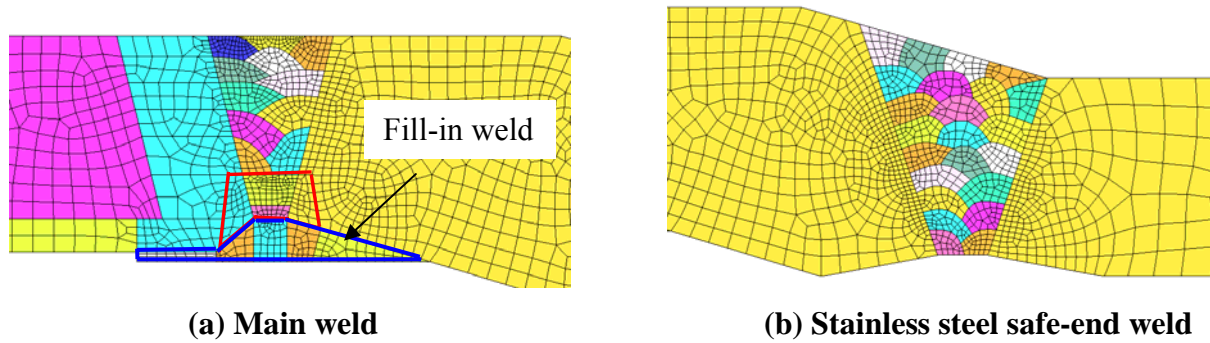
Figure 35 Emc² surge nozzle weld details

The following sequence was followed in the surge nozzle welding simulation analyses:
- Each pass of the main DM weld was deposited from the ID to the OD in a left-to-right sequence.
- The land (0.1") was removed from the ID using an element removal technique.
- The last pass was deposited on the ID in one weld pass.
- For certain cases, the weld repair area was removed using an element removal technique. The repair was made in three weld passes with either a left-to-right or right-to-left sequence. The repair was always assumed to be centered within the weld and not centered on the fusion line.
- The fill-in weld*** was added in five passes with either a left-to-right or right-to-left sequence.
- The stainless steel weld was deposited from the ID to the OD in a left-to-right sequence. (Note this step was omitted in some of the analyses).
- A hydrotest was simulated at a pressure of 2,794 psi (1.25*2,235 psi) at ambient conditions.
- The model was then taken to operating temperature (644F).

In addition, the following individual welding residual stress calculations were considered for the surge nozzle analyses:
- Main DM weld including the safe-end weld
  - With no repair (0.1-inch last pass) - left to right sequence
  - With no repair (0.1-inch last pass) - right to left sequence
  - With repair (5/16 inch) – left to right sequence
  - With repair (5/16 inch) – right to left sequence
- Main DM weld excluding the safe-end weld
  - With no repair (0.1-inch last pass) - left to right sequence
  - With no repair (0.1-inch last pass) - right to left sequence
  - With repair (5/16 inch) – left to right sequence
  - With repair (5/16 inch) – right to left sequence

An example of the axial stress (in MPa) contour plot for the surge nozzle with a left-to-right weld sequence but without the repair and stainless steel safe-end weld is shown in Figure 36,

_____

*** The fill-in weld is used to seat the thermal sleeve in the Westinghouse surge nozzles.

while the similar run but with a right-to-left weld sequence is shown in Figure 37 In each of these cases, the arrow represents the linear path that best approximates the maximum stress path in the weld material. This arrow goes through the highest tensile stress on both the ID and OD, while going through the smallest compressive stress at the mid thickness. It should be noted the weld sequence not only changes the magnitude of the stresses but also the path with the maximum stress.
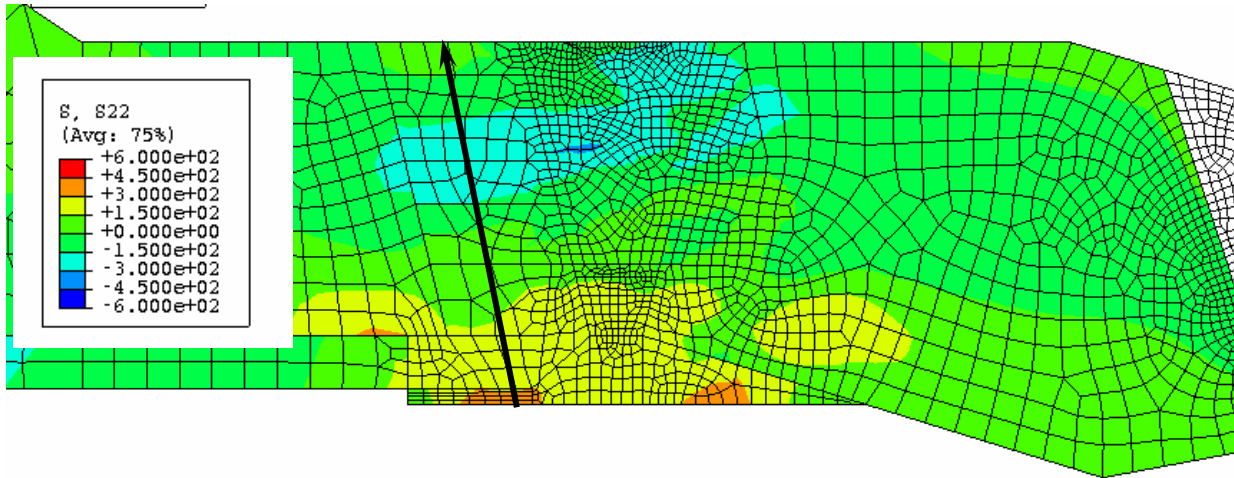
Figure 36 Axial stress for surge nozzle case without stainless steel weld at 644F with left-to-right weld sequence and no repair. (Arrow indicates the path of maximum stress in the weld material)
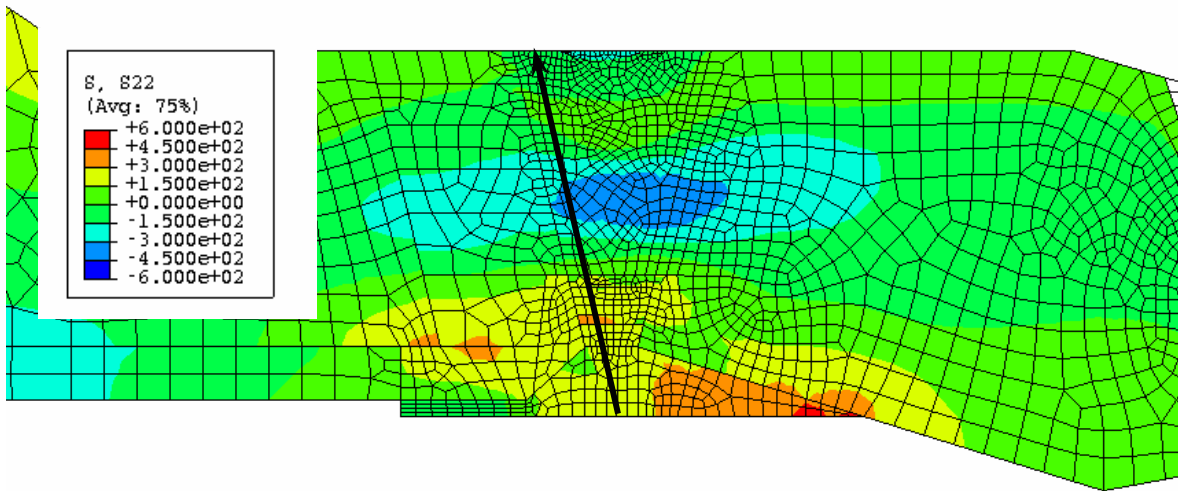
Figure 37 Axial stress for surge nozzle case without stainless steel weld at 644F with right-to-left weld sequence and no repair. (Arrow indicates the path of maximum stress in the weld material)

36

Figure 38 shows a similar contour plot as shown in Figure 36, but includes the weld repair. As with the weld sequencing, the addition of the weld repair also moved the location of the maximum stress path from the butter to more centered in the weld.
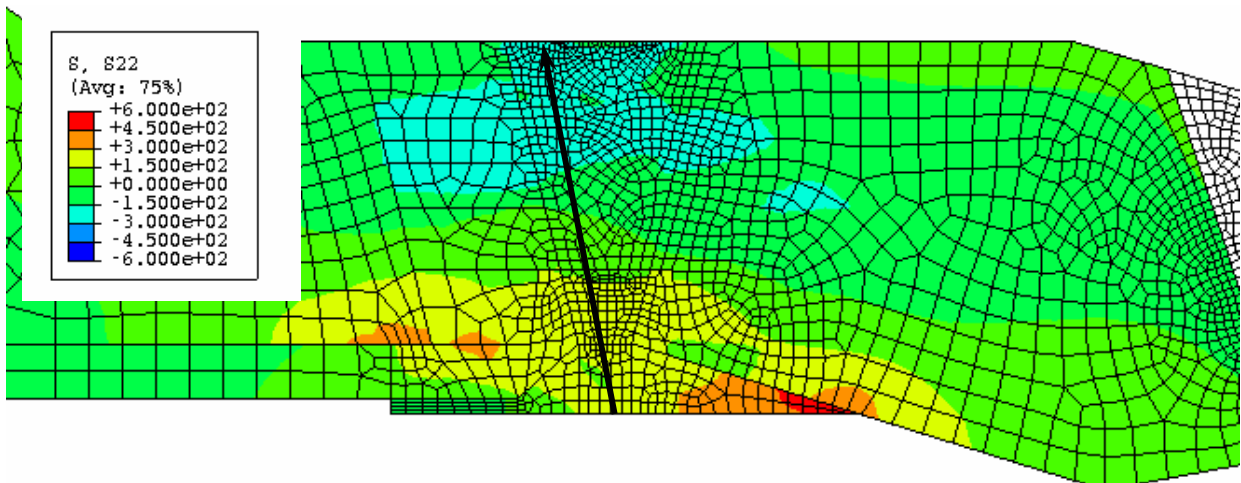
Figure 38 Axial stress for surge nozzle case with weld repair but without stainless steel weld at 644F. (Arrow indicates the path of maximum stress in the weld material)

A comparison of the axial stresses (solid symbols = Emc², open symbols = DEI) along the paths described above for the surge nozzle case with no repair and with and without stainless steel safe-end weld is given in Figure 39. Also included in this figure is the surge nozzle welding residual stress profile used in the scoping analyses. As was described in Reference 1, the scoping analysis surge nozzle WRS was developed by Battelle in the LB-LOCA contract for a slightly different geometry than analyzed here. For the cases without the stainless steel safe-end weld (triangles), the results are relatively close. The Emc² analysis results tend to be slightly higher than the DEI results, especially before the ID tension transitions to compression. The ID stresses from the Emc² analyses were very similar in magnitude to those used in the scoping analysis. Overall the trends from the scoping analysis results tend to fall between those calculated by Emc² and DEI. However, when the stainless steel safe end weld is considered (circles), larger differences in the results are present.   The differences between the Emc² and DEI results occur on the ID and can again be attributed to the modeling of the compliance of the piping system. As was similar with the relief analyses, the Emc² analysis assumes a system compliance by use of a linear spring at the end of the model, while the DEI analysis assumes no compliance. The pipe system compliance is important since the added resistance may affect the axial and local bending stress generated during the stainless steel welding process.

A comparison of the surge nozzle results with the weld repair are shown in Figure 40. In this figure the results from DEI are only with the stainless steel safe-end since they did not complete an analysis with repair and without the stainless steel weld. The comparisons in the figure are very similar to those in Figure 39 and the same conclusion can be drawn about the comparisons.
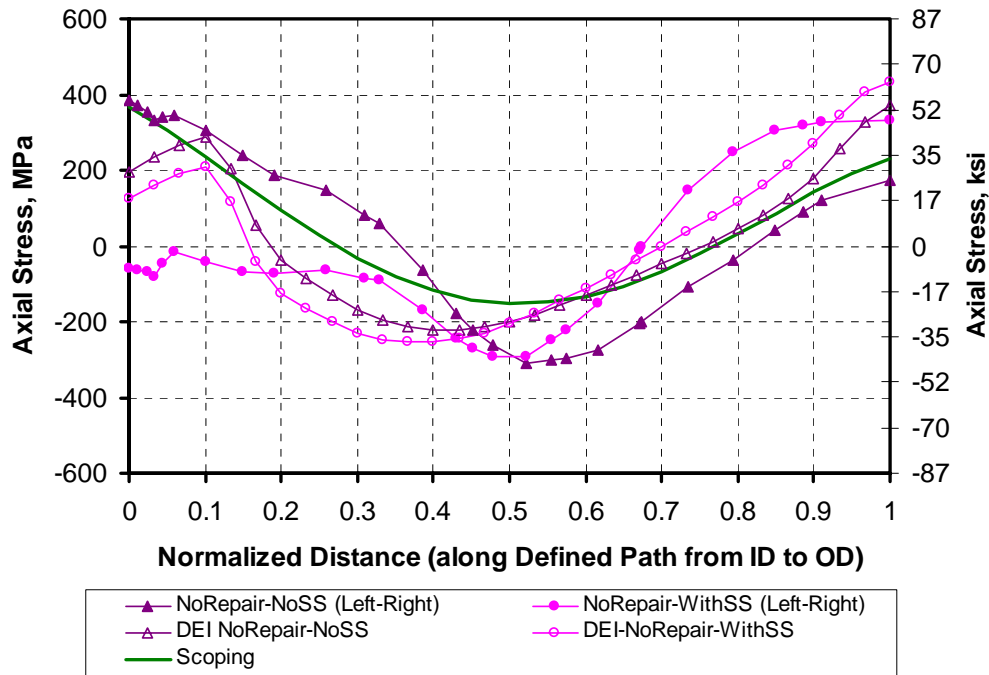
Figure 39 Comparison of surge nozzle WRS (left-to-right weld sequence) with no repairs with and without stainless steel safe-end weld at operating temperature (Solid symbols = Emc^2, open symbols = DEI)
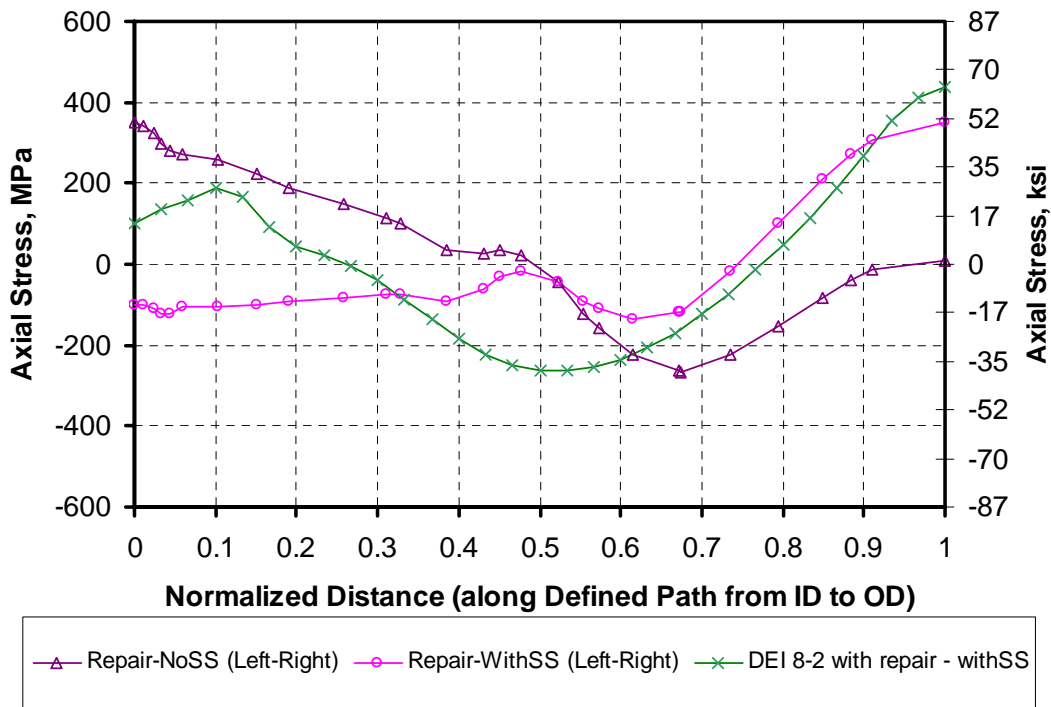
Figure 40 Comparison of surge nozzle WRS (left-to-right weld sequence) with repair and with and without the stainless steel safe-end weld at operating temperature

The effect of the weld sequencing is further explored in Figure 41. In this figure, the results without the stainless steel safe-end weld are shown for both DEI (diamond symbols) and Emc^2 (triangle symbols). The Emc^2 results include both the left-to-right (open symbols) and right-to-left (closed symbols) weld sequence. Note that the weld sequence in the DEI results is undefined since each weld pass spanned the entire width of the weld, whereas the Emc^2 analyses used reasonably sized weld beads and was able to change the weld fill-in sequence during the welding process. Also note that each of these stresses come from a different location in the weld. In the Emc^2 analysis, the maximum path was chosen for a particular analysis, with the weld sequence affecting the location of this path. Even with these stipulations, the trends in the results are similar. The weld sequence appears to affect the stresses on the ID by about 100 MPa (14.5 ksi), with the left-to-right sequence producing higher stresses. There is an additional 100 MPa difference in the ID stresses when DEI weld sequence is considered. The largest difference in the results is the through-thickness location where the ID stresses pass into compression. For the Emc^2 right-to-left sequence, this occurs at a distance of 45% of the wall thickness from the ID, while the Emc^2 left-to-right sequence, this point occurs at 35% of the wall thickness. For the DEI sequence, this transition happens quickly, the ID stresses become compressive after 18% of the wall thickness. It is suspected that the location of this transition from tension to compression will have a direct impact on when/if a growing PWSCC crack will arrest.
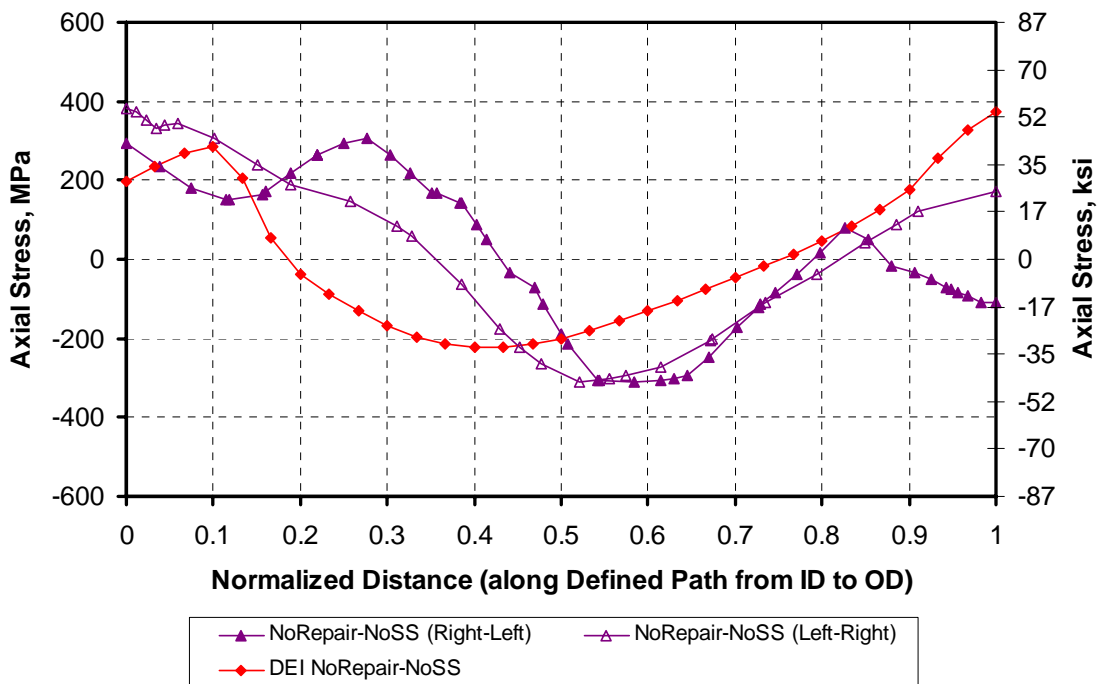
Figure 41 Effect of fill-in weld sequence for surge nozzle WRS at operating temperature (Triangle symbols = Emc^2, diamond symbols = DEI)

Since the figures previously presented were determined from the maximum stress paths for each individual finite element run, it was prudent to compare these stresses across the same path to determine if the welding stresses calculated by DEI are confirmed with these analyses. The path chosen to make these direct comparisons is shown in Figure 42. The path chosen was vertical in nature and located 0.25 inch from the top of the main DM weld toward the butter.
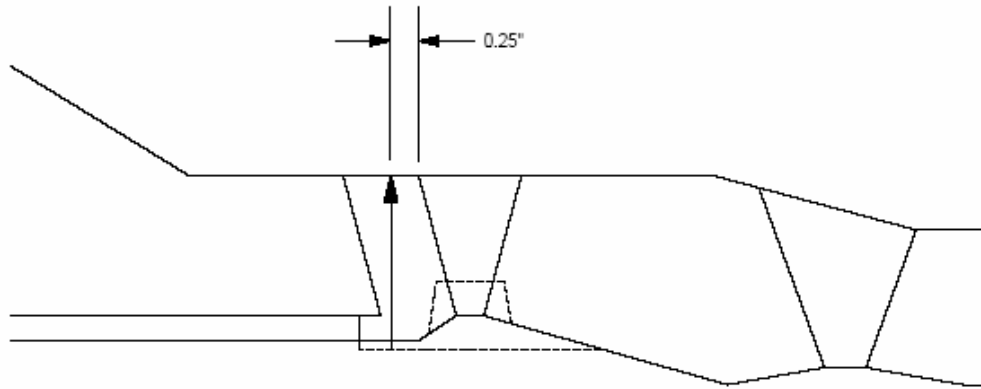
Figure 42 Location of section for direct comparison of surge nozzle results

A comparison of the axial stress values along the path given above for the surge nozzle without weld repair and before the fill-in weld is given in Figure 43. As shown in this figure, the comparison of stress is very good, with less than 10 ksi difference on the ID surface. However, when the fill-in weld is added, large differences occur, as shown in Figure 44. This figure is very similar to Figure 41, but all stress values are taken along the path shown in Figure 42.   This figure again illustrates the effect of the weld sequencing on the final welding residual stress. Therefore it is very important to properly model the weld sequence to make accurate predictions of welding residual stress.
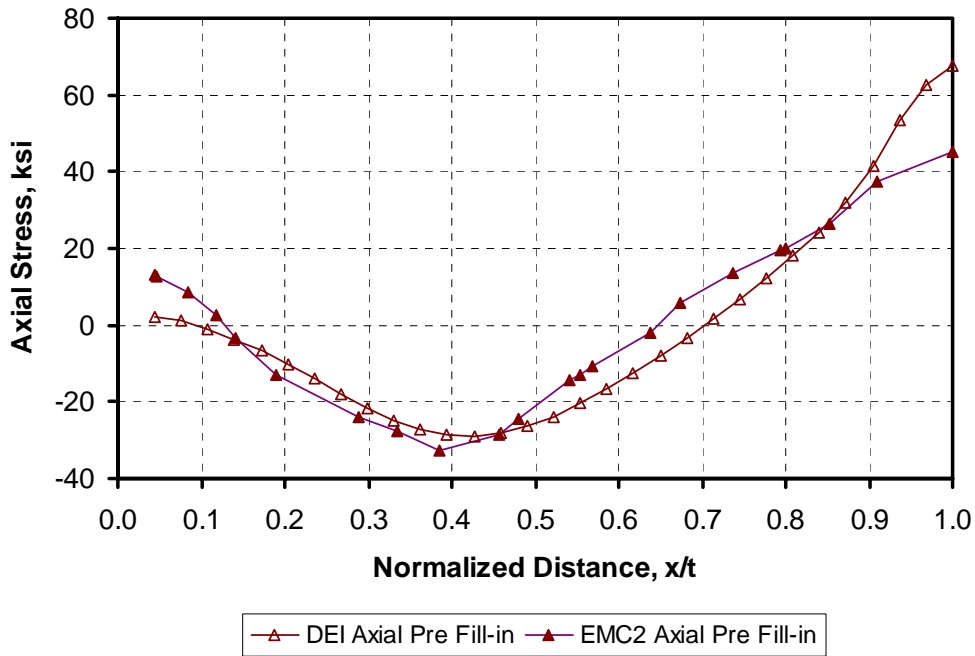
Figure 43 Comparison of surge nozzle axial residual stresses before fill-in weld
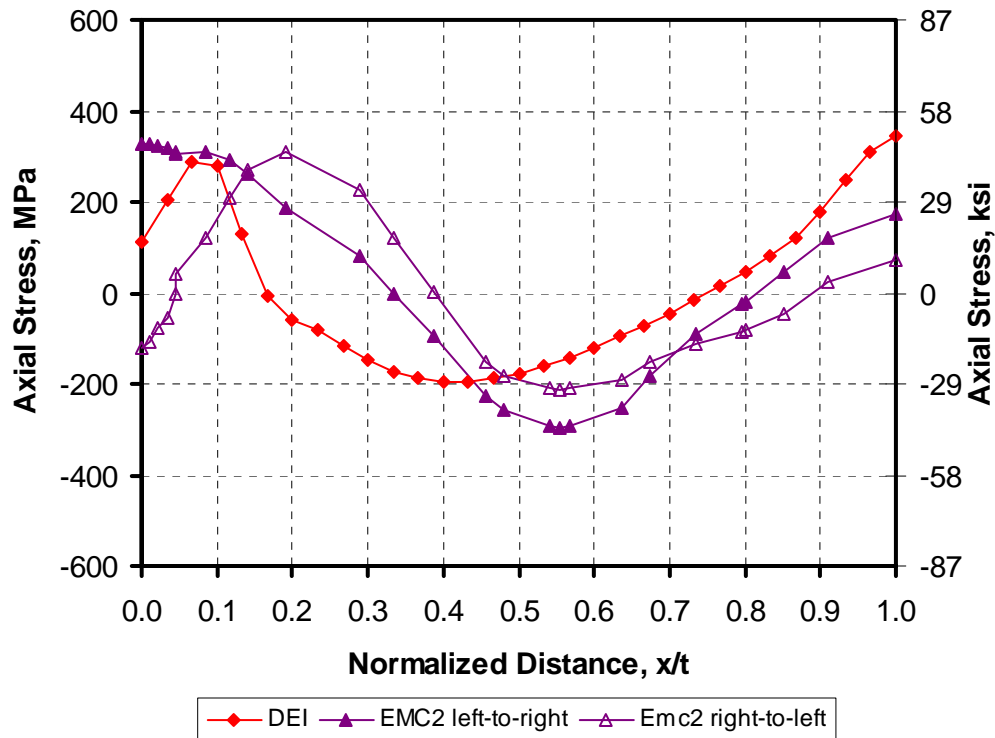
Figure 44 Comparison of surge nozzle axial residual stress with no safe end weld, and no repair along path described in Figure 42 at operating temperature

4.6 EU report validation

As a first attempt at validation of the welding residual stress predictions, Battelle, Emc^2 and DEI conducted an additional set of welding residual stress analyses. In this small effort, the DM weld mock-up conducted by the European Commission Joint Research Centre's (JRC) Institute for Energy was analyzed. The EU project [32] investigated a wide range of issues related to the structural integrity assessment of a stainless steel weld joining stainless steel and low alloy steel components. Also in this effort, a series of round-robin exercises that compared predicted welding residual stress distributions to those measured from the aforementioned welded joint mockup was conducted. Complete details of the mockup geometry, welding process, and material properties were made available to all participants in the round-robin. The welding residual stress analysis results for each participant were compared to the through-wall stresses measured by neutron diffraction (ND).

In this effort, the problem statement [33] that was delivered to the EU round-robin participants was used by Battelle, Emc^2, and DEI for conducting similar analyses. A description of the Emc^2 analyses results and the comparison of the Battelle, Emc^2 and DEI results to the EU round robin participant results and the ND results are given in Appendix A.

5. Confirmatory Results

The purpose of this section of the report is to compare and contrast the crack growth analyses conducted by Emc^2 with those conducted by DEI. As noted previously, the confirmatory results presented in this section were calculated separately from the DEI effort with the computer code

PipeFracCAE that was written by Emc^2 specifically for this purpose. DEI had no direct influence on the development or output of the PipeFracCAE code. The same holds true for Emc^2 influence on the industry's FEACrack code.

This section of the report will first begin by discussing the results of the Phase I effort, then transition to the confirmatory Phase II calculations. This section will conclude with a short discussion on the differences between the results.

5.1 Phase I results

The Phase I effort in this program was to verify the usability of these unique crack growth codes, by re-analyzing the critical case from the NRC staff's original Wolf Creek scoping analysis [1]. As mentioned earlier, in that report, it was shown that the Wolf Creek relief line was the limiting case, in that the 21:1 indication aspect ratio found in that DM weld may rupture before leakage when reasonable ASME Section XI assumptions were made. To demonstrate the level of conservatism brought on by using a semi-elliptical flaw assumption in the crack growth analysis, all of the loads, geometry, and the welding residual stress profile used in the scoping analysis were retained in the Phase I calculations. As explained in Section 2 of this report, the crack growth analysis procedure is linear elastic in nature; therefore, the welding residual stress profile can be incorporated into the fracture model by use of an equivalent temperature distribution over the weld length. Depending on mesh size and density, there may be some differences in how this temperature distribution resolves into elastic stresses in the model. For instance, in the Phase I analyses, the resultant residual stresses from the Emc^2 and DEI analyses can be compared against the residual stress definition, see Figure 45. In this figure, the open and solid circle represent the resultant welding residual stress on the crack plane in the Emc^2 model at the 0 degree (crack center) and 180 degree locations. The solid triangle represents the DEI welding stress at 180 degrees in their model. The results show a good comparison.

However, if the axial extent of the welding residual stresses are investigated, larger differences are noticed as shown in Figure 46. In this figure, the open symbols represent the Emc^2 results while the solid symbols represent the DEI results. The difference in the stresses can be attributed to the mesh density differences in the models.

As part of the confirmatory analyses, Emc^2 completed two runs of the Phase I problem. The first was with a welding residual stress that best matched the Phase I DEI welding residual stress assumptions (called DEI fit), and the second was the Emc^2 best fit (called Emc^2 fit) to the cubic trend labeled "ASME WRS" in Figure 45.

42
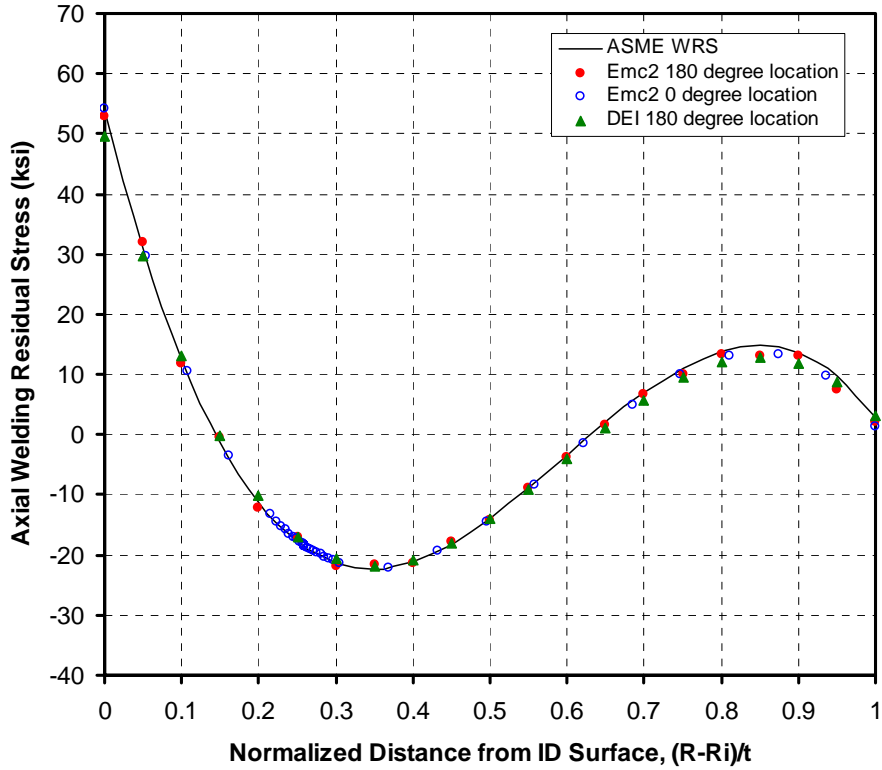
Figure 45 Through-thickness weld residual stress profile used in Phase I calculations
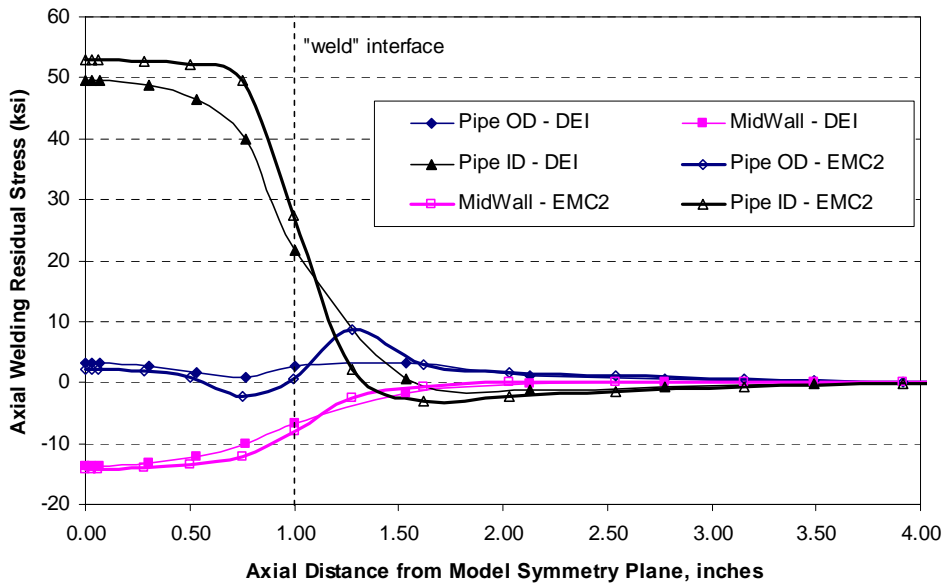
Figure 46 Axial extent of welding residual stress assumed in Phase I calculations

The crack profiles for the two Phase I runs conducted in this effort are given in Figure 47 and Figure 48 for the Emc² fit and DEI fit of the WRS respectively. As shown in these figure, the crack profile shapes are very similar, but the times to first leakage are different by 1.2 years. Further investigation of this difference indicated that the curve fit of the WRS results in the

43

compressive zone were responsible for this difference. At this point, the K-values are approaching zero, and a slight under or overestimation can have a large impact on the time to leakage.
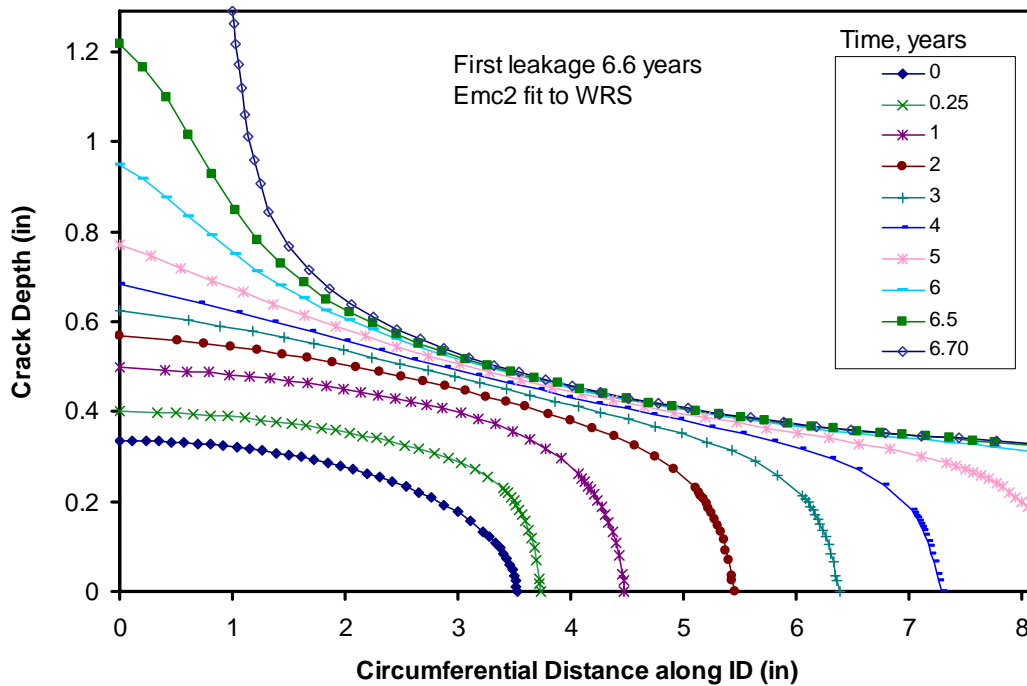
Figure 47 Crack profiles from the Emc² Phase I calculations using Emc² WRS fit
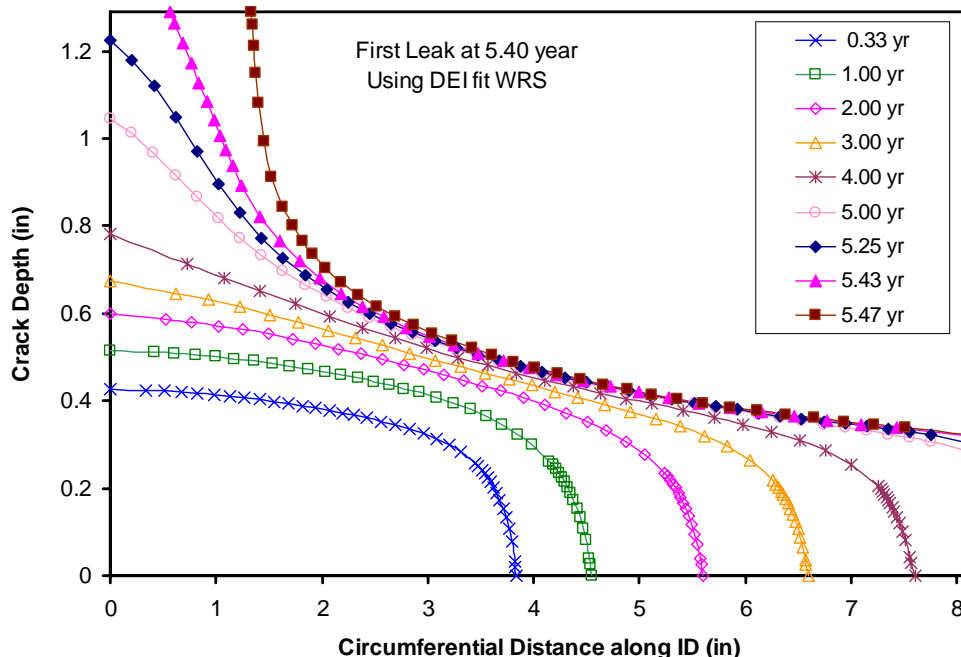
Figure 48 Crack profiles from the Emc² Phase I calculations using DEI WRS fit

However, even though the times to leakage are different, the crack shapes near leakage are almost identical, as illustrated in Figure 49. In this figure, the crack profiles near leakage are plotted using both the DEI fit and Emc² fit to the WRS. Even though these cracks happen at

different times, the shapes are near identical. This fact indicates that even though these differences in WRS fit affect the time to leakage, the load margin on critical crack size and further growth of the through-wall crack will not be affected by these difference in the WRS fit.
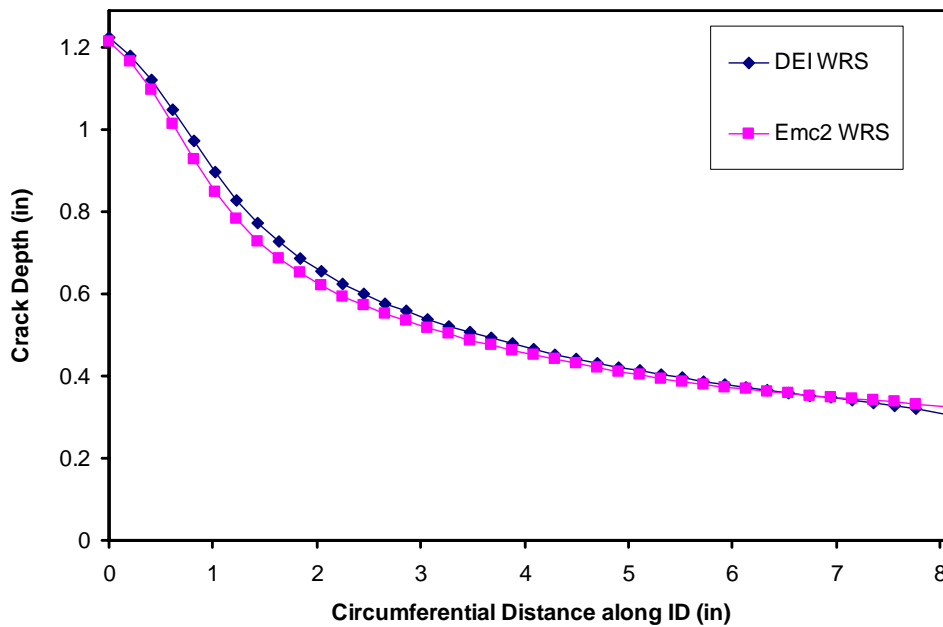
Figure 49 Comparison of crack profile prior to leakage

The calculations made in this effort can be directly compared to those calculated by DEI in their report [2]. As stated in Section 4.4 of their report [2], they also got varying times to crack initiation when slight changes in the WRS were made. These differences also did not affect the shape of the crack at leakage. As a direct comparison, when DEI used the WRS fit that is labeled DEI fit in this report, they calculated a time to leakage of 5.36 years as compared to 5.40 years calculated by Emc^2. This is in excellent agreement and confirms that the computer codes are outputting very similar crack growth predictions for similar inputs.

One other aspect from this Phase I work was the investigation of the load margin on critical crack size for the surface crack at first leakage. This study was necessary since the original scoping study claimed that the surface crack would be critical for these conditions. For the flaw shape just before leakage, the actual crack profile and the semi-elliptical assumptions are compared in Figure 50. For this crack, the natural crack shape has a crack stability load margin of 2.7, which illustrates the level of conservatism in making semi-elliptical assumption in this type of analyses. The level of conservatism can also be estimated by comparing the crack areas. In this case, the natural forming crack has a crack area that is 57% of the semi-elliptical crack. Eliminating the semi-elliptical assumption clearly reduced the conservatism in this type of analysis.

45
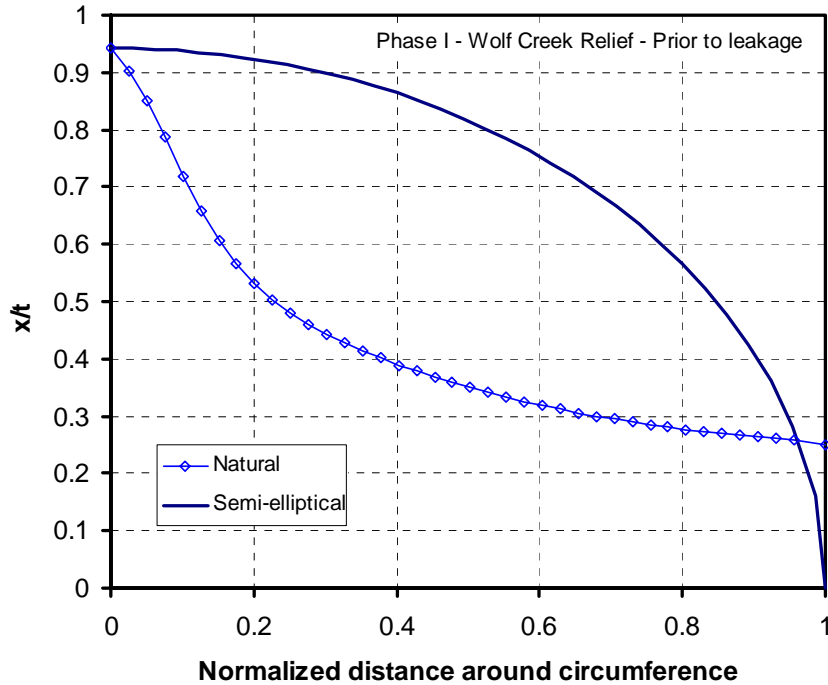
Figure 50 Comparison of semi-elliptical and natural forming crack shape

In addition, the margin between leakage and rupture can be calculated using the procedures listed in this report. For the Phase I case, the margin and leak-rate results are shown in Figure 51. In this figure, the Emc^2 fit to the WRS was used; however, the case with the DEI fit was also run with only minimal difference[†††] between the results.   The results in Figure 51 suggest there is almost 4 months between the first leakage and rupture of the relief nozzle.

Also shown in Figure 51 are the DEI results from the Phase I study. At first leakage, both the leakage rate and the margin on critical crack size were very similar. However, the Emc^2 results decreased quicker than the DEI results. As discussed in the next section of this report, this difference is due to the crack front shape assumption made at first leakage. In the DEI analyses, the crack front at first leakage is much more rounded, while the crack from the Emc^2 analyses is more sharp causing higher K-values and faster growth rates. This difference is further discussed in Section 5.3.1.

[†††] No difference was noted since after leakage, the time between leakage and rupture is more controlled by the bending moment from operational stresses than the residual stress.
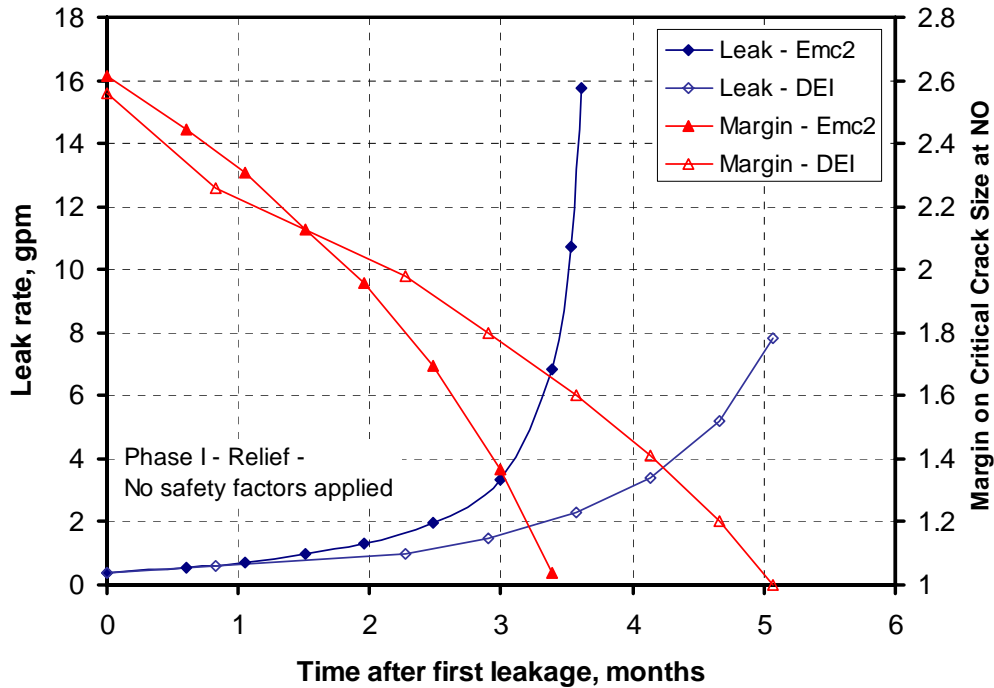
Figure 51 Margin and leak rate results for the Phase I calculations

5.2   Description of Phase II cases analyzed

The Phase II analysis matrix was developed by DEI, EPRI and their expert panel with review and comments from the NRC staff and Emc[2]. DEI was the main developer of the matrix, with its development and review presented at public meetings throughout the first half of 2007. The purpose of these analyses presented in this report is to confirm some of the results generated by DEI. It is not the purpose of these analyses to replicate every run and conditions in their program, but to check to make sure their results are reasonable. Throughout the development of this test matrix, there were many detailed discussions on technical topics pertaining to how to correctly conduct these analyses. Agreement on all technical points was not possible, and many compromises were necessary due to the time constraints in this program. Because of these compromises, a couple of points need to be addressed:

- All of the loads and geometries were generated by industry and are fully documented in Reference 2. A few of the plant specific drawings were reviewed by the NRC staff and Emc[2], but for the majority, these values were not confirmed by the NRC staff or Emc[2].
- The critical crack size was calculated per Section 2.2 of this report.
- Due to analyses conducted by the industry, and as discussed in Section 3.2.2, the only secondary stresses assumed in these analyses are the normal thermal expansion (which includes normal stratification) stresses. Other secondary stresses, such as transient thermal stratification stresses, are assumed to be relieved for critical crack size calculations, and assumed not to impact subcritical crack growth calculations.   As discussed, on average, the normal thermal loads are on average 59 percent of the limiting thermal loads.
- Occurrence of SSE loading is assumed to have a small probability over the short time period in question, and is therefore not considered in these analyses.

47

- The crack is assumed to grow subcritically per the MRP-115 [34] 75th percentile crack growth law in these confirmatory analyses. DEI conducted sensitivity analyses on both the crack growth coefficient and exponent. It also assumed that linear-elastic fracture mechanics controls the subcritical crack growth. As will be discussed later, the stress intensity solutions at through-wall penetration may be very high and some ductile tearing may occur. This is neglected in these analyses.

The analyses conducted in this confirmatory effort were conducted in stages. First, confirmatory analyses were conducted for certain cases in the overall DEI analysis matrix [2]. From these cases, critical cases were identified, and other parameters were varied to aid in the understanding of the impact of these parameters on the margin between leakage and rupture. In all cases, Emc^2 conducted the crack growth analyses completely independent of the DEI analyses.

Table 5 gives the details for the cases run for the confirmatory analyses. The case labeled P1 is the result from the Phase I analysis. The second column in this table lists the corresponding DEI analysis case number. The detailed description of the geometry configurations and Plant ID is given in Reference 2. The DEI case S10b is not included in Reference 2, but is discussed in Reference 35.

Table 6 gives the loads, welding residual stress cases, and the initial crack sizes for each of the confirmatory analyses conducted. A couple of notes about the welding residual stress cases shown:
- ASME - Emc^2 Mod - Emc^2 fit – This residual stress field is the same one used in the original Emc^2 scoping analysis. It is labeled Emc^2 fit since the Phase I work showed that the DEI and Emc^2 curve fits of this residual stress field did not produce the exact same results. The reason for this discrepancy, as described earlier, is a difference in finite element mesh density. The thermal strain procedure used to estimate these residual stresses in the crack growth models make the estimation of stresses somewhat mesh size dependent. Therefore some difference in the comparisons may occur because of this modeling difference.
- ASME - Emc^2 Mod - Emc^2 fit - 1" weld – This is the same stress field as the previous bullet, but the length of the weld assumed in this case is a total of one inch instead of the two inch length used in the other analyses.
- DEI - Type 8 without SS weld – All of the residual stress field labeled this way, i.e., DEI/Emc^2 – Type XX, etc., were taken from the finite element analyses conducted in this program. For instance, DEI – Type 8 without SS weld is the DEI finite element analysis results for the Type 8 geometry without taking credit for the stainless steel safe-end weld. In all cases, the curve fitting and implementing via the thermal strain approximation was performed by Emc^2.
- Emc^2 - Type 8 with SS weld (modified) – In this one case, a residual stress field was chosen that was not directly calculated by the finite element analyses. To investigate the sensitivity of WRS on the surge nozzle results, the Emc^2 case with a stainless steel safe-end weld was modified to have a slightly higher ID stress, see Figure 52.
- DEI – repair without SS weld – In this one case, DEI supplied Emc^2 with temperature distributions and resultant stress distributions for a limited extent (40 degrees) ID repair case they constructed for the surge nozzle. Emc^2 took the temperatures and applied them

to the Emc^2 surge model. The resultant stress fields are compared in Figure 53. In this figure, the "repaired" stress field is applied over 40 degrees centered at the top of the pipe. The "unrepaired" stress field is applied over 280 degrees centered on the bottom of the pipe. The remaining 40 degrees (20 degrees on each side of the symmetry plane) is the transition between the two aforementioned stress fields. The resultant stresses were shown to be in equilibrium across the entire cross section. The results show some slight differences in the stress which can be attributed to the differences in the meshes used.
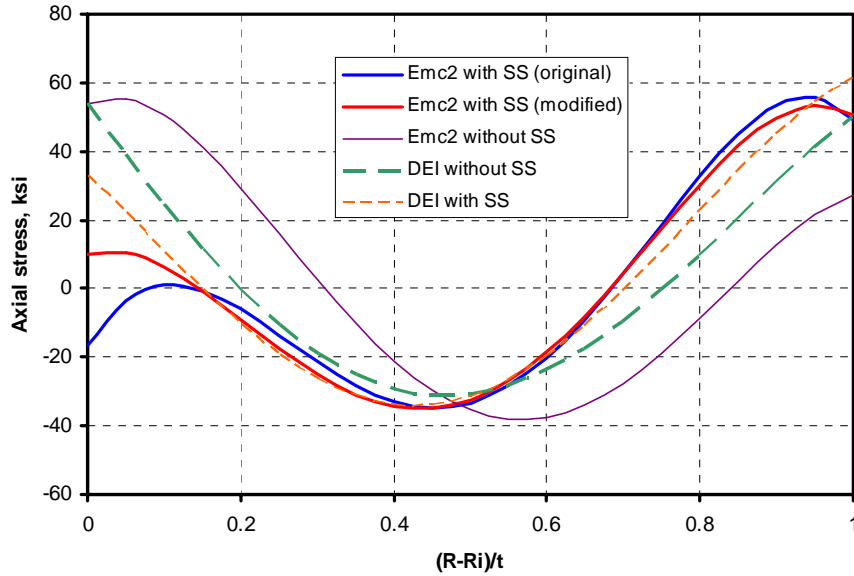
Figure 52 Welding residual stress field used for surge nozzle analyses
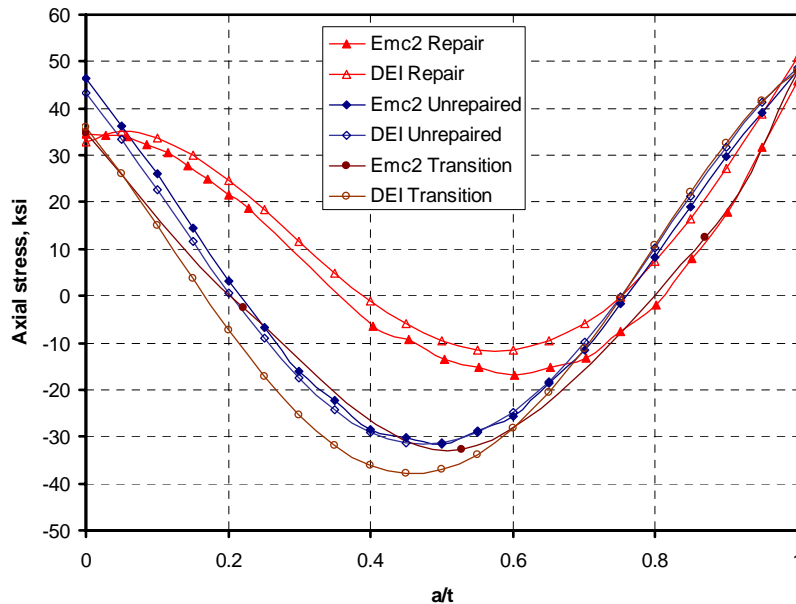
Figure 53 Comparison of resultant stress fields for ID repair case

Along with the cases that were meant to directly confirm the DEI results, additional cases were conducted in order to understand the sensitivity of key parameters. Since it is not

49

directly obvious what the pertinent varied parameter is in each case, the following lists the variations in the critical cases:

- Case 6 was found to be the critical case for the safety/relief/spray nozzles.
    - Case 6-1 and Case 6-2 varied the initial flaw size (21:1 with a/t=26% for Case 6-1 and 6:1 with a/t=10% for Case 6-2), keeping everything else constant.
    - Case 6-3 was identical to Case 6-1 except the initial flaw was placed on the bottom of the pipe instead of on the top. This case was meant to further investigate the effect of crack placement. Note that the placement of the crack on the bottom of the pipe was simulated by reversing the sign of the applied moment (See Table 6)
    - Case 6-4 was identical to Case 6, except the WRS was assumed to occur over a 1-inch weld as compared to the 2-inch weld assumed in Case 6.
- Case 17 was found to be the critical case for the surge nozzle.
    - Case 17 and 17-2 were identical to cases run by DEI (Case S1b and 17b respectively).
    - Case 17-1 was the same as Case 17 except used the Emc^2 WRS without the stainless steel safe-end weld.
    - Case 17-3 is identical to Case 17-2 except used the Emc^2 WRS without the stainless steel safe-end weld.
    - Case 17-4 is identical to Case 17 except with the DEI WRS with the stainless steel safe-end weld.
    - Case 17-5 is identical to Case 17-2 expect the initial flaw was placed on the bottom of the pipe instead of the top. Note that the placement of the crack on the bottom of the pipe was simulated by reversing the sign of the applied moment (See Table 6)
    - Case 17-6 is identical to Case 17 except used the Emc^2 WRS with the stainless steel safe-end weld.
    - Case 17-7 is identical to Case 17 except used the Emc^2 modified WRS with the stainless steel safe-end weld.
    - Case 17-8 is identical to Case 17-2 except with the DEI WRS with the stainless steel safe-end weld.
    - Case 17-9 and 17-10 are identical to Case 17 but with lower bending moment specific to Plants B and C, respectively.
    - Case 17-11 is identical to Case 17 except the WRS used was identical to the surge nozzle limited extent ID repair case conducted by DEI.
    - Case 17-12 is identical to Case 17 except the bending moment used after through-wall crack penetration was decreased to 2205.57 in-kips.
- An additional case was run for Case 9 to investigate the initial flaw size approximation.
- An additional case was run for Case 11 since the original case used the incorrect bending moment for direct comparison to DEI.
- An additional case was run for Case 19, since using a Type 8 WRS without stainless weld is not appropriate for a CE geometry.

Table 5 Confirmatory analyses matrix

Case #	DEI Case #	Nozzle Type	Geometry Configuration	Plants	R_o (in)	t (in)	R_i/t
P1	P1	S&R	Type 1a	AEH	3.875	1.290	2.004
1	1c	S&R	Type 1a	AEH	3.875	1.290	2.004
1-1	1b	S&R	Type 1a	AEH	3.875	1.290	2.004
3	3c	S&R	Type 1a	AEH	3.875	1.290	2.004
6	6c	S&R	Type 2a/2b	BCG	3.875	1.065	2.638
6-1	38c	S&R	Type 2a/2b	BCG	3.875	1.065	2.638
6-2	-	S&R	Type 2a/2b	BCG	3.875	1.065	2.638
6-3	-	S&R	Type 2a/2b	BCG	3.875	1.065	2.638
6-4	35c	S&R	Type 2a/2b	BCG	3.875	1.065	2.638
9	-	S&R	Type 3	DI	4.000	1.405	1.847
9-1	9c	S&R	Type 3	DI	4.000	1.405	1.847
10	10c	spray	Type 4	AE	2.905	0.900	2.228
11	-	spray	Type 4	AE	2.905	0.900	2.228
11-1	11c	spray	Type 4	AE	2.905	0.900	2.228
15	15c	spray	Type 7	DI	2.595	1.045	1.483
17	S1b	surge	Type 8	AEHBCG	7.500	1.580	3.747
17-1	-	surge	Type 8	AEHBCG	7.500	1.580	3.747
17-2	17b	surge	Type 8	AEHBCG	7.500	1.580	3.747
17-3	-	surge	Type 8	AEHBCG	7.500	1.580	3.747
17-4	-	surge	Type 8	AEHBCG	7.500	1.580	3.747
17-5	-	surge	Type 8	AEHBCG	7.500	1.580	3.747
17-6	-	surge	Type 8	AEHBCG	7.500	1.580	3.747
17-7	-	surge	Type 8	AEHBCG	7.500	1.580	3.747
17-8	-	surge	Type 8	AEHBCG	7.500	1.580	3.747
17-9	-	surge	Type 8	AEHBCG	7.500	1.580	3.747
17-10	-	surge	Type 8	AEHBCG	7.500	1.580	3.747
17-11	S10b	surge	Type 8	AEHBCG	7.500	1.580	3.747
17-12	-	surge	Type 8	AEHBCG	7.500	1.580	3.747
19	-	surge	Type 9	DI	6.530	1.470	3.442
19-1	19b	surge	Type 9	DI	6.530	1.470	3.442
20	20b	surge	Type 9	DI	6.530	1.470	3.442

5.3 Phase II results

As mentioned before, the purpose of the Phase II results in this effort is to confirm the industry's analysis results and to investigate some of the issues that may have not been fully discussed in the industry's report.

Table 7 presents the overall results for the Phase II confirmatory analyses. In this table, the first column is the case number and the second column is the corresponding DEI case number. The next four columns are margins and times at first leakage and 1gpm leakage. The final four columns are time and leakage for a crack size with a 1.2 and 1.0 load margin on critical crack size. The selection of a load margin on failure of 1.2 was chosen by the industry as one of their evaluation criteria. It was used here for comparison purposes only.

Table 6 Loads, welding residual stress profiles and initial crack shapes for the confirmatory analyses

Case #	DEI Case #	p (ksi)	Temp (F)	F_{axial} (kips)	M (in-kips)	WRS Case	2c/a	Depth (%tw)
P1	P1	2.235	653	52.33	277.5	ASME - Emc^2 Mod - Emc2 fit	21	26%
1	1c	2.235	653	45.64	209.28	ASME - Emc^2 Mod - Emc^2 fit	360°	10%
1-1	1b	2.235	653	45.64	209.28	DEI - Type 1 S&R without SSWeld	360°	10%
3	3c	2.235	653	45.64	178.90	ASME - Emc^2 Mod - Emc^2 fit	360°	10%
6	6c	2.235	653	52.44	252.14	ASME - Emc^2 Mod - Emc^2 fit	360°	10%
6-1	38c	2.235	653	52.44	252.14	ASME - Emc^2 Mod - Emc^2 fit	21	26%
6-2	-	2.235	653	52.44	252.14	ASME - Emc^2 Mod - Emc^2 fit	6	10%
6-3	-	2.235	653	52.44	-252.14	ASME - Emc^2 Mod - Emc^2 fit	21	26%
6-4	35c	2.235	653	52.44	252.14	ASME - Emc^2 Mod - Emc^2 fit - 1"weld	360°	10%
9	-	2.235	653	47.94	201.91	ASME - Emc^2 Mod - Emc^2 fit	21	26%
9-1	9c	2.235	653	47.94	201.91	ASME - Emc^2 Mod - Emc^2 fit	360°	10%
10	10c	2.235	653	26.96	72.78	ASME - Emc^2 Mod - Emc^2 fit	360°	10%
11	-	2.235	653	26.96	61.48	ASME - Emc^2 Mod - Emc^2 fit	360°	10%
11-1	11c	2.235	653	26.96	66.98	ASME - Emc^2 Mod - Emc^2 fit	360°	10%
15	15c	2.235	653	17.49	55.65	ASME - Emc^2 Mod - Emc^2 fit	360°	10%
17	S1b	2.235	644	247.70	2750.77	DEI - Type 8 without SS weld	360°	10%
17-1	-	2.235	644	247.70	2750.77	Emc^2 - Type 8 without SS weld	360°	10%
17-2	17b	2.235	644	247.70	2750.77	DEI - Type 8 without SS weld	21	26%
17-3	-	2.235	644	247.70	2750.77	Emc^2 - Type 8 without SS weld	21	26%
17-4	-	2.235	644	247.70	2750.77	DEI - Type 8 with SS weld	360°	10%
17-5	-	2.235	644	247.70	-2750.77	DEI - Type 8 without SS weld	21	26%
17-6	-	2.235	644	247.70	2750.77	Emc^2 - Type 8 with SS weld	360°	10%
17-7	-	2.235	644	247.70	2750.77	Emc^2 - Type 8 with SS weld (modified)	360°	10%
17-8	-	2.235	644	247.70	2750.77	DEI - Type 8 with SS weld	21	26%
17-9	-	2.235	644	247.70	2629.32	DEI - Type 8 without SS weld	360°	10%
17-10	-	2.235	644	247.70	1687.89	DEI - Type 8 without SS weld	360°	10%
17-11	S10b	2.235	644	247.70	2750.77	DEI- ID repair without SS weld	360°	10%
17-12	-	2.235	644	247.70	2205.57	DEI - Type 8 without SS weld	360°	10%
19	-	2.235	644	180.96	2034.30	DEI - Type 8 without SS weld	360°	10%
19-1	19b	2.235	644	180.96	2034.30	DEI - Type 8 with SS weld	360°	10%
20	20b	2.235	644	180.96	682.65	DEI - Type 8 with SS weld	360°	10%

Table 7 Phase II confirmatory results

		Leak				Crack Size			
		TW Penetration		1gpm leak		Load Margin = 1.2		Load Margin = 1	
Case #	DEI Case #	Time (yr)	Load Margin	Delta Time (mo)	Load Margin	Delta Time (mo)	Leakage (gpm)	Delta Time (mo)	Leakage (gpm)
P1	P1	6.6	2.61	1.56	2.1	3.21	4.8	3.42	7.3
1	1c	20.16	3.45	3.28	2.46	5.46	5.80	5.68	8.65
1-1	1b	Arrest	Arrest	Arrest	Arrest	Arrest	Arrest	Arrest	Arrest
3	3c	29.40	3.68	4.48	2.55	6.90	6.80	7.34	9.20
6	6c	4.13	2.20	1.03	1.79	2.16	6.25	2.34	11.00
6-1	38c	4.09	2.43	N/C	N/C	N/C	N/C	N/C	N/C
6-2	-	5.44	2.60	N/C	N/C	N/C	N/C	N/C	N/C
6-3	-	9.95	2.08	0.52	1.80	1.26	3.75	1.44	6.25
6-4	35c	3.26	2.07	0.59	1.81	1.30	5.50	1.48	9.40
9	-	125.36	4.25	7.40	2.51	9.58	4.26	9.80	7.40
9-1	9c	119.18	4.27	7.50	2.50	10.40	6.25	10.8	10.00
10	10c	51.36	3.96	5.40	2.48	7.25	4.30	7.60	12.50
11	-	Arrest	Arrest	Arrest	Arrest	Arrest	Arrest	Arrest	Arrest
11-1	11c	Arrest	Arrest	Arrest	Arrest	Arrest	Arrest	Arrest	Arrest
15	15c	Arrest	Arrest	Arrest	Arrest	Arrest	Arrest	Arrest	Arrest
17	S1b	1.30	1.00	0.00	1.00	N/A	N/A	0.00	10.86
17-1	-	SC critical	N/A	N/A	N/A	N/A	N/A	N/A	N/A
17-2	17b	1.36	1.80	N/C	N/C	N/C	N/C	N/C	N/C
17-3	-	0.53	1.62	0.00	1.62	N/C	N/C	N/C	N/C
17-4	-	5.80	1.53	0.13	1.50	1.07	20.90	1.39	65.00
17-5	-	9.07	0.80	N/A	N/A	N/A	N/A	0.00	29.17
17-6	-	Arrest	Arrest	Arrest	Arrest	Arrest	Arrest	Arrest	Arrest
17-7	-	Arrest	Arrest	Arrest	Arrest	Arrest	Arrest	Arrest	Arrest
17-8	-	6.15	1.64	0.06	1.58	N/C	N/C	N/C	N/C
17-9	-	1.39	1.05	0.00	1.05	N/A	N/A	0.00	2.38
17-10	-	2.84	1.38	0.00	1.38	0.64	6.40	0.94	18.20
17-11	S10b	0.86	1.37	0.00	1.37	0.31	12.40	0.62	33.00
17-12	-	1.30	1.19	0.00	1.19	N/A	N/A	0.48	10.00
19	-	1.36	1.07	N/A	N/A	N/A	N/A	0.00	2.27
19-1	19b	9.50	1.60	0.30	1.58	1.48	16.00	1.79	55.00
20	20b	Arrest	Arrest	Arrest	Arrest	Arrest	Arrest	Arrest	Arrest

N/C = Not Calculated

N/A = Not Available

The results shown in Table 7 were extracted from the individual runs for each case. The results for a 1gpm leaking crack and a crack at a load margin 1.2 were chosen since those cases were specified in the DEI report as the basis for their evaluation criteria. DEI did not supply the

leakage rate and margin as a function of time for every case, therefore direct comparison can only be made for a few cases. For every case conducted in this effort where crack growth occurred between a 1gpm leakage and a load margin of 1.0, a plot of the leakage rate and margin as a function of time was generated and is given in Appendix B.

5.3.1   Direct confirmatory results

A direct comparison of the DEI and Emc^2 Phase II analyses results is shown in Table 8. This table shows three comparisons, i.e., time to first leakage, critical crack size load margin at a leakage of 1gpm and time between 1gpm leakage and a critical crack size load margin of 1.2. For the time to first leakage comparison, when arrests did not occur, the time estimated by Emc^2 was always longer than the time estimated by DEI. On average the estimates by Emc^2 were about 12% higher, expect for cases 9-1 and 10, which were much higher. For those cases, the results were investigated further, and it was determined that the residual stresses caused the crack to slow down. In fact the K-solution was approaching zero, and it took many years before it began to increase. As mentioned in the Phase I work, the arrest behavior of these cracks can be influenced by the fit to the welding residual stress, if those stresses produce a stress intensity near zero. In this effort, Emc^2 fit and implemented these welding residual stresses into the crack growth code independently of DEI. This difference in WRS fit and the mesh differences cause the difference in time to leakage and arrest versus non-arrest behavior of Cases 11-1, 17-8 and 19-1. Interestingly, in one case (11-1) Emc^2 predicted arrest where DEI did not, while in two cases (17-8 and 19-1) DEI predicted arrest, while Emc^2 did not. This illustrates the uncertainty in the curve fit for the welding residual stress, as it is implemented into these crack growth codes.

Table 8 Comparison of Emc^2 and DEI results

Case #	DEI Case #	Time at first leakage (yr)		Load Margin at 1gpm leak		Time since 1gpm leak to 1.2 margin on load (Month)	
		DEI	Emc^2	DEI	Emc^2	DEI	Emc^2
P1	P1	5.36	6.6	1.98	2.1	2.33	1.65
1	1c	17.4	20.16	2.24	2.46	3.63	2.18
1-1	1b	Arrest	Arrest	Arrest	Arrest	Arrest	Arrest
3	3c	26.3	29.40	2.40	2.55	4.17	2.42
6	6c	3.4	4.13	1.70	1.79	1.37	1.13
6-4	35c	2.9	3.26	1.62	1.81	1.07	0.70
9-1	9c	32.2	119.18	2.50	2.50	4.80	2.90
10	10c	21.2	51.36	2.07	2.48	2.43	1.85
11-1	11c	25.3	Arrest	2.08	Arrest	2.43	Arrest
15	15c	Arrest	Arrest	Arrest	Arrest	Arrest	Arrest
17-1	S1b	1.2	1.30	1.03	1.00	0.00	0.00
17-2	17b	1.2	1.36	1.71	1.80	1.17	N/A
17-8	17a	Arrest	6.15	Arrest	1.58	Arrest	N/A
17-11	S10b	0.50	0.86	1.36	1.37	0.43	0.31
19-1	19b	Arrest	9.50	Arrest	1.58	Arrest	1.18
20	20b	Arrest	Arrest	Arrest	Arrest	Arrest	Arrest

For the critical crack margins at crack size that gives a leakage of 1 gpm, the Emc^2 analyses were higher on average by 7%. These are reasonable differences for the differences in assumptions made by Emc^2 and DEI. However, the biggest differences are seen in the time between the 1gpm leakage and when the load margin reaches 1.2. On average the DEI results are higher than the Emc^2 results by 30%. In order to investigate this difference, the trends of leakage and margin as a function of time for both the DEI and Emc^2 analyses for Case 6c and 35c (Emc^2 Case 6 and 6-4) are shown in Figure 54 and Figure 55, respectively.
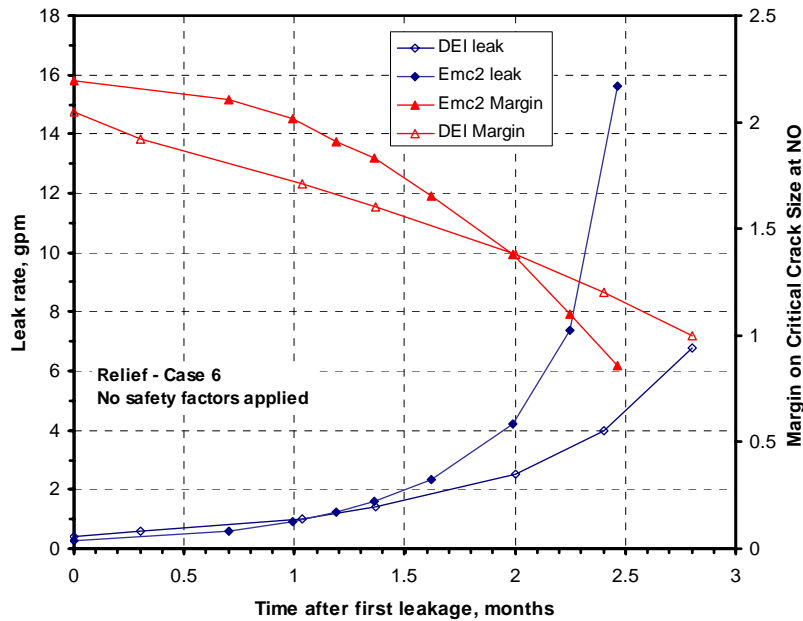

Figure 54 Comparison of Emc^2 and DEI results for Case 6 (6c) (NO = Normal operating stresses)

In each of these figures, the solid symbols are the Emc^2 results and the open symbols are the DEI results. In terms of margin, the Emc^2 results are always higher than the DEI results at first leakage, but then appear to decrease more rapidly than the DEI results. The leakages are relatively consistent up to about 2 gpm, but then begin to diverge with the Emc^2 results becoming much larger than the DEI results. The differences in the leak rates are most probably due to the crack length assumptions made in the calculations, and the differences in the leak rates codes for the 100% steam calculations. As described earlier, in the Emc^2 analyses, since SQUIRT allows the input of the OD and ID crack length and COD, the ID crack length was assumed to be the actual ID crack length and equal to the OD crack length. The results from these two cases were averaged. As an example, the results from Case 6 are shown in Figure 56. In this figure, the diamond symbols are the Emc^2 SQUIRT calculations with the ID length of the crack equal to the ID circumference (long ID) in the first case, and equal to the OD crack length (short ID) in the second case. There is some difference between these cases, with the DEI results falling between these cases up to about 2gpm. However, after that point, the Emc^2 results are still much higher than the DEI results. In addition, if the leak rates are compared at the same load margin on critical crack size, the Emc^2 leakage rates are higher than the DEI results. The difference is due to the 100% steam flow models in PICEP and SQUIRT.

In order to check the elastic COD calculated with the finite element model, the same leak rate calculations were conducted with SQUIRT, but using the GE/EPRI method for calculating the

COD (elastic and plastic contributions to the COD). These results are shown in Figure 57. The GE/EPRI solution gave COD values that were similar for the smaller crack lengths, but larger for the longer crack lengths. This difference is due to the elastic-plastic contribution that is not accounted for the elastic FE analyses conducted in this effort. In no cases were the calculated COD values much less than the Emc^2 FE generated COD values as was suggested by the DEI results in Figure 56.
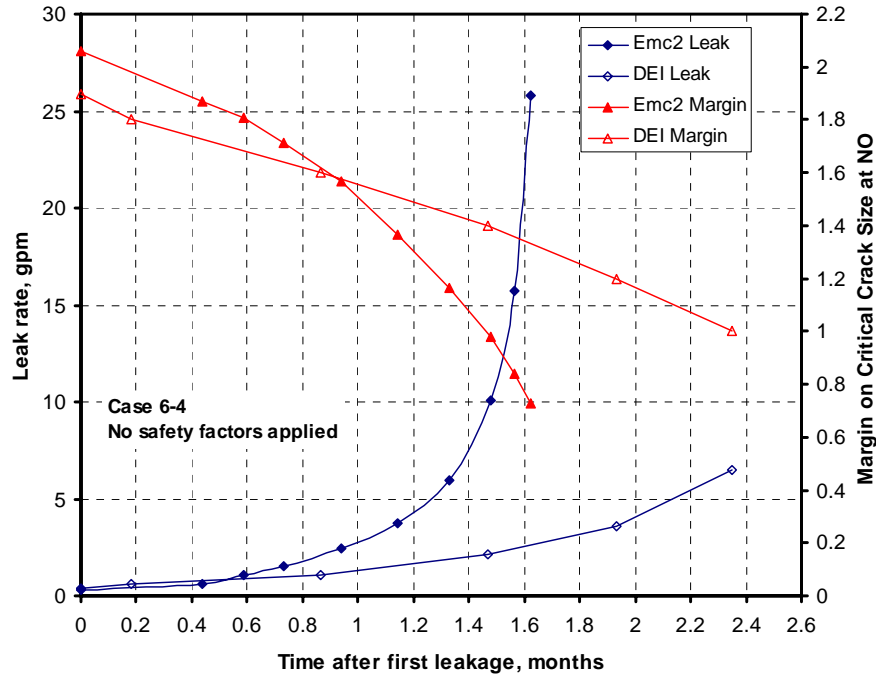
Figure 55 Comparison of DEI and Emc^2 results for Case 6-4 (35) (NO = Normal operating stresses)
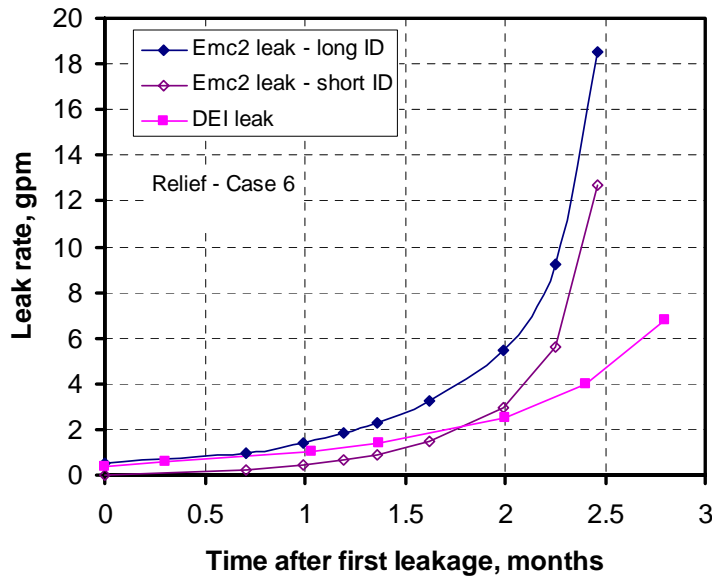
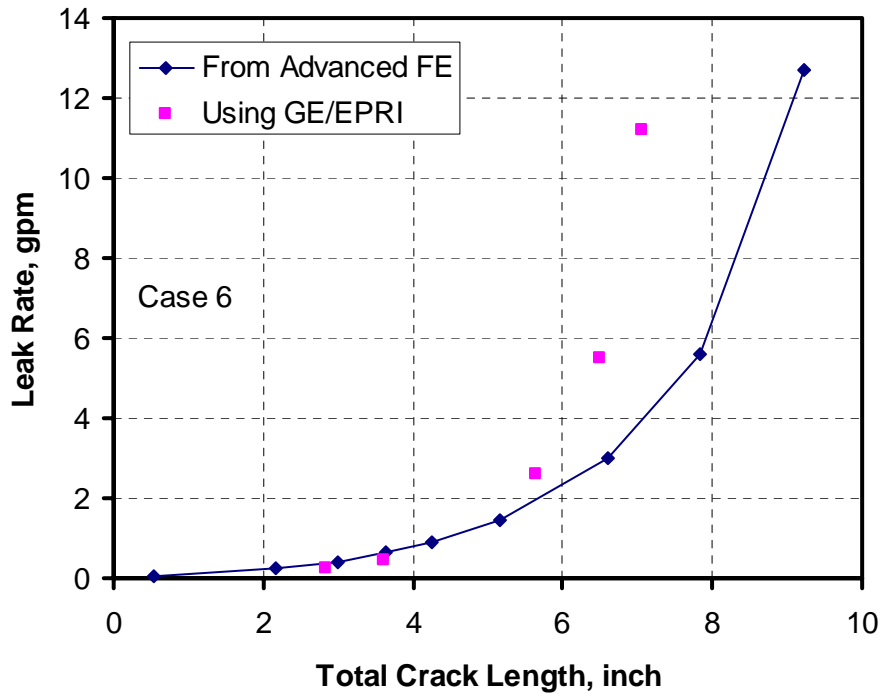**Figure 56 Comparison of leak rates for Case 6**

56

Figure 57 Comparison of leak rates calculated with COD values from Emc^2 elastic FE analysis and GE/EPRI (elastic-plastic) for Case 6

The differences seen in the critical crack size margin, suggest that the Emc^2 crack at first leakage is smaller than the DEI crack at first leakage, but the rate of crack growth in the Emc^2 analyses is greater. Quality assurance checks of the critical crack size calculations were carried out and it was shown through several examples, that the same limit load was calculated for identical cracks within about 1%. Therefore, the crack evolution with time was investigated for Cases 6 and 35, as shown in Figure 58. In this figure, the solid symbols are the DEI results, while the open symbols are the Emc^2 results. As expected, the OD crack length at first leakage is much shorter in the Emc^2 analysis then in the DEI analysis, but the trends suggest that the cracks are growing at different rates. It is possible that the number of crack growth steps may be causing the difference. Note that the same crack growth procedure was used in the Emc^2 analysis for both the surface and complex crack growth. For the Case 6 analysis, the DEI results showed a total of 53 steps between first leakage and 1.0 margin on load, while the Emc^2 analysis showed only 25 steps. However, for Case 35, the DEI analysis results showed a total of 26 steps between first leakage and 1.0 margin on load, while the Emc^2 analysis showed 49 steps. Since the trends between the Emc^2 and DEI results are the same regardless of whether Case 6 or 35 are considered, this difference in number of steps does not affect the results. In fact, if Case 35 is looked at in detail, the average OD crack growth per increment was 0.064 inch for DEI and 0.068 inch for Emc^2. Therefore, if the crack growth increment per step is similar, but the times are different, the K-values must be higher in the Emc^2 case in order to drive the crack faster during these growth increments. Further investigation would be required to confirm this statement.
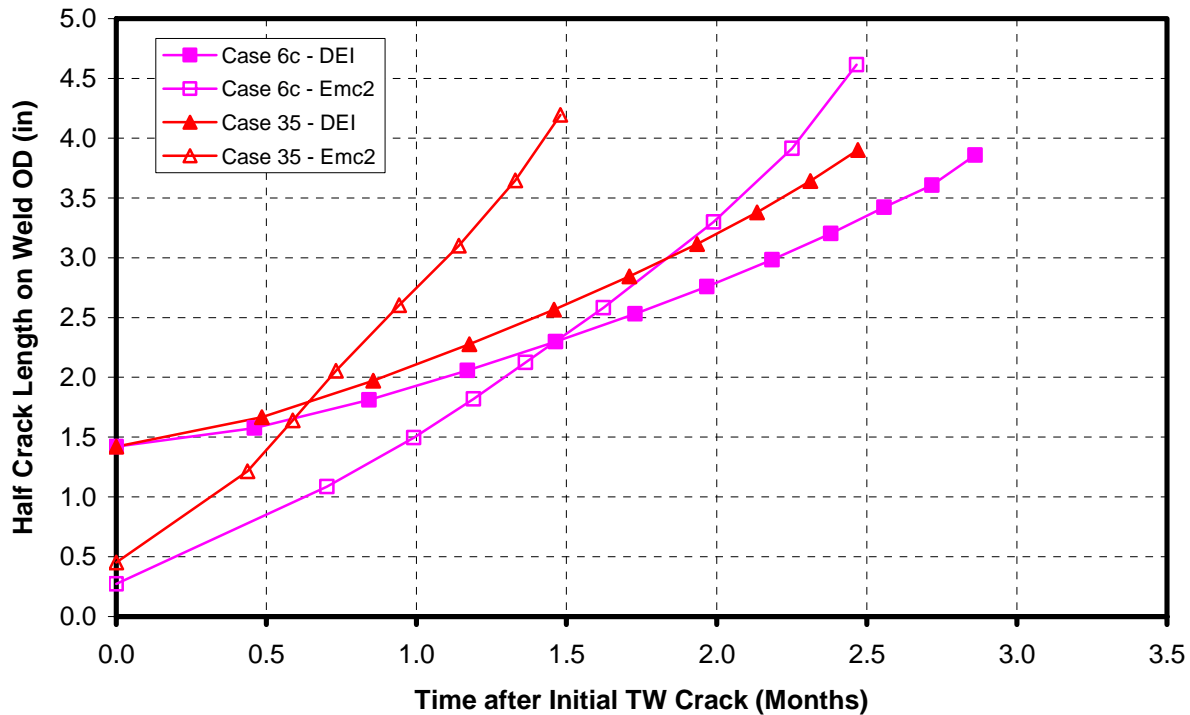
Figure 58 Comparison of crack length as a function of time for Case 6 (6c) and 6-4 (35)

5.3.2   Other cases

In addition to the direct comparisons, some additional cases were run in order to investigate input parameters that may not have been completely addressed in the industry report. Case 6 was shown to be the limiting case for the safety, relief and spray nozzles. So for this case, the initial crack size and the length of the welding residual stress zone were varied. The results of those additional analyses are given in Table 9. In this table, Case 6-1 and 6-2 have the same inputs as Case 6 except the length of the initial flaw was decreased to 2c/a=21, a/t=26% for Case 6-1 and 2c/a=6, a/t=10% for Case 6-2. These results both show that Case 6 is the limiting crack size case. In both Cases 6-1 and 6-2, the margin at first leakage is greater than that for Case 6. Since the margins at first leakage were greater, these cases were terminated since the margins on critical crack size would be larger than that for Case 6. In addition, neither Case 6-1 nor Case 6-2 went 360 degrees before going through-wall. However, for Case 6-3, the crack from Case 6-1 was placed on the bottom (minimum bending) of the pipe with all other inputs the same. This crack grew around the circumference and became through-wall at a much longer time, i.e., 10 years as compared to 4 years, but was more critical than Case 6.   This difference is due to the fact that the crack actually penetrates the wall thickness at about 20 degrees from top-dead-center, resulting in a longer leaking crack than Case 6. In addition, the time between leakage and margin of 1.2 is also greatly reduced.

Putting the crack on the bottom is one way to account for the variability in the crack initiation location of the flaws. The probability is higher that a crack will initiate at the highest load location, i.e., at the location of maximum moment. However, the probability is not zero that a

crack may form at any location with a tensile stress. Therefore, the possibility of a crack initiating at the bottom of the pipe needs to be accounted for in these analyses.

Case 6-4 investigated the effect of modifying the axial extent in the finite element model where the temperature gradient is placed to simulate the welding residual stresses. In Case 6-4, the axial extent was reduced from 2 inches to 1 inch. In this case, this difference decreased the time from through-wall penetration to a margin of 1.2 by about 35%. Similar results by DEI showed only a 25% decrease in time. Superposition suggests that these two results should be identical. Further investigation of these results illustrate that the differences in the calculated stress fields from the applied thermal gradients and the approximation made at first through-wall crack penetration account for these differences.

Table 9 Case 6 sensitivity cases

Case #	M (in-kips)	WRS Case	2c/a	Depth (%tw)	TW Penetration		1gpm leak		Margin=1.2		Margin =1	
					Time (yr)	Margin	Delta Time (mo)	Margin	Delta Time (mo)	Leakage (gpm)	Delta Time (mo)	Leakage (gpm)
6	252.14	ASME - Emc2 Mod - Emc2 fit	360°	10%	4.13	2.20	1.03	1.79	2.16	6.25	2.34	11.00
6-1	252.14	ASME - Emc2 Mod - Emc2 fit	21	26%	4.09	2.43	N/C	N/C	N/C	N/C	N/C	N/C
6-2	252.14	ASME - Emc2 Mod - Emc2 fit	6	10%	5.44	2.60	N/C	N/C	N/C	N/C	N/C	N/C
6-3	-252.14	ASME - Emc2 Mod - Emc2 fit	21	26%	9.95	2.08	0.52	1.80	1.26	3.75	1.44	6.25
6-4	252.14	ASME - Emc2 Mod - Emc2 fit - 1"weld	360°	10%	3.26	2.07	0.59	1.81	1.30	5.50	1.48	9.40

N/C = Not Calculated

Case 17 was the limiting case for the surge nozzle analyses. Table 10 shows a summary of the additional cases run to compliment Case 17. In this table, the results have been sorted by welding residual stress assumption and then by load and crack shape. The first two rows are Cases 17-4 and 17-8. These cases were run with the DEI Type 8 welding residual stress with the stainless steel safe end weld, see Figure 52. If a 360 degree, 10% deep crack is assumed (Case 17-4), a margin of 1.5 was calculated at a 1gpm leakage, with about 1 month between that time and a critical crack size load margin of 1.2. If a 21:1 flaw with a/t=26% is considered, those margins increase. In contrast, if the Emc^2 Type 8 welding residual stresses with the safe-end weld was used, the crack arrests. In addition, if the ID stress of this residual stress field is increased to 10 ksi, the crack still arrests (Case 17-7).

The next five cases use a more conservative WRS distribution, i.e., the DEI Type 8 WRS without the stainless steel safe-end weld. For these cases, when a 360 degree, 10% deep flaw was assumed, the flaw at first leakage had a load margin for failure of only 1.0, and a leakage of about 11 gpm. If a 21:1 flaw that was 26% deep was assumed, the load margin for failure at leakage was increased to 1.8 with a first leakage of 2.25 gpm. This margin is very similar to the 1.7 load margin at first leakage calculated by DEI for this same case. To investigate the effect of a lower bending stress on this result, Cases 17-9 and 17-10 were conducted with bending stresses corresponding to Plants B and C, respectively, while Case 17-12 was conducted with a bending moment after through-wall penetration between Cases 17-9 and 17-10. For Cases 17-9 and 17-10, both the time to first leakage and the load margin at failure was increased from Case 17. In addition, the decreased bending moment after through-wall penetration in Case 17-12 increased the margin and time between leakage rupture as compared to Case 17.

Table 10 Case 17 Sensitivity Cases

Case #	M (in-kips)	WRS Case	2c/a	Depth (%tw)	Leak TW Penetration Time (yr)	Leak TW Penetration Margin	Leak 1gpm leak Delta Time (mo)	Leak 1gpm leak Margin	Crack Size Margin=1.2 Delta Time (mo)	Crack Size Margin=1.2 Leakage (gpm)	Crack Size Margin=1 Delta Time (mo)	Crack Size Margin=1 Leakage (gpm)
17-4	2750.77	DEI - Type 8 with SS weld	360°	10%	5.80	1.53	0.13	1.50	1.07	20.90	1.39	65.00
17-8	2750.77	DEI - Type 8 with SS weld	21	26%	6.15	1.64	0.06	1.58	N/C	N/C	N/C	N/C
17-6	2750.77	EMC2 - Type 8 with SS weld	360°	10%	Arrest	Arrest	Arrest	Arrest	Arrest	Arrest	Arrest	Arrest
17-7	2750.77	EMC2 - Type 8 with SS weld (modified)	360°	10%	Arrest	Arrest	Arrest	Arrest	Arrest	Arrest	Arrest	Arrest
17-2	2750.77	DEI - Type 8 without SS weld	21	26%	1.36	1.80	1.36	1.80	N/C	N/C	N/C	N/C
17	2750.77	DEI - Type 8 without SS weld	360°	10%	1.30	1.00	0.00	1.00	N/A	N/A	0.00	10.86
17-9	2629.32	DEI - Type 8 without SS weld	360°	10%	1.39	1.05	0.00	1.05	N/A	N/A	0.00	2.38
17-12	2205.57	DEI - Type 8 without SS weld	360°	10%	1.30	1.19	0.00	1.19	N/A	N/A	0.48	10.00
17-10	1687.89	DEI - Type 8 without SS weld	360°	10%	2.84	1.38	0.00	1.38	0.64	6.40	0.94	18.20
17-5	-2750.77	DEI - Type 8 without SS weld	21	26%	9.07	0.80	N/A	N/A	N/A	N/A	0.00	29.17
17-3	2750.77	EMC2 - Type 8 without SS weld	21	26%	0.53	1.62	0.00	1.62	N/C	N/C	N/C	N/C
17-1	2750.77	EMC2 - Type 8 without SS weld	360°	10%	SC critical	N/A	N/A	N/A	N/A	N/A	N/A	N/A
17-11	2750.77	DEI-repair without SS weld	360°	10%	0.86	1.37	0.00	1.37	0.31	12.40	0.62	33.00

N/C = Not Calculated
N/A = Not Available

Case 17-5 is identical to Case 17-2 expect the initial flaw was placed on the bottom of the pipe instead of on top of the pipe centered on the maximum moment. This case simulates the possibility of the crack initiating at a location other than at the maximum moment location. As shown in Table 10, this flaw took nine times longer to leak, but had a lower load margin at first leakage.

The next two cases are identical to Cases 17-4, and 17-8 expect the Emc^2 Type 8 WRS without the stainless steel safe-end weld was used. This WRS is assumed to be conservative. For the case with the 21:1 flaw that was 26% deep, the flaw became through-wall very quickly, but had a load margin at leakage that was similar to the other cases. When the 360 degree flaw that was 26% deep was used with this WRS, the surface flaw was critical before leakage.

The final case, 17-11, was identical to Case 17 except the 40 degree, ID repair weld WRS solution was used. This case illustrates that the limited extent ID repair caused the crack to go through-wall quicker and have more margin on failure than without the repair. It should also be noted that the repair simulated in this case was only 5/16 inch deep. A deeper limited extent ID weld repair would increase the local ID stress and tend to increase the margin on critical crack size further.

5.4 Discussion

For all of the cases analyzed, the DEI results presented in their report were confirmed. There were some distinct difference in the times between leakage and rupture, i.e., the Emc^2 times were always less by about 30 percent. The differences must be due to the shape of the crack at first leakage.   Other than the confirmed results, the critical case for the relief/safety/spray nozzle geometries is Case 6, while Case 17 is the critical case for the surge nozzle geometry. The extra cases run that were associated with Case 6 illustrated how the variability in the WRS solution affect the results of these analyses. Slightly changing how the same residual stress field is

applied to the model gave a 35% decrease in the time between 1gpm leakage and a load margin of 1.2. In addition, the decay in WRS away from the crack plane in the crack growth model was never directly compared to the actual simulated axial extent of the WRS field. It is unknown if using the applied temperatures to simulate the WRS in the fracture model correctly captures the behavior away from the crack plane.

The possibility of multiple crack initiations or initiation occurring at a location other than at the maximum moment location were investigated with the extra cases run that were associated with Case 17. These cases illustrated that if a 21:1 flaw (or shorter) was located at the maximum moment location, the flaw would leak with considerable load margin on critical crack size at 1gpm, and sufficient time between leakage and a load margin on critical crack size of 1.2. However, if a 360 degree flaw that is 10% deep is assumed to model multiple crack initiations, the flaw would be near critical at first leakage. In addition, if the flaw initiated at a location other than at the maximum moment, i.e., at the bottom of the pipe, the flaw could grow completely around the ID of the pipe before leakage, and would again be near critical at first leakage. If the bending load is decreased after through-wall crack penetration, as it may be due to the relief of displacement-controlled loads, the margin at critical crack size increases significantly. In addition, if a limited extent ID repair is present, the crack will grow quickly through-wall and have more margin on critical crack size than the case without the repair.

6. Applicability of Analysis Methodology

The purpose of this section of the report is to make overall conclusions about the applicability of this advanced FEA methodology for making predictions of leak and rupture for postulated defects in pressurizer nozzles. The applicability of this methodology pertains only to the case at hand, i.e., the nine subject plants that may have to inspect their pressurizer nozzles prior to Spring 2008. This section is not meant to address the overall and global applicability of this analysis procedure and methodology.

6.1 Improvements over Standard Analyses

In order to address the applicability of this work, the direct improvements made over standard crack growth analyses are first discussed. In this case, the standard analysis considered is a typical ASME Section XI type analysis.

6.1.1 *Removal of idealized crack shape assumption*

Probably the main improvement made to the typical Section XI-type analysis is the removal of the idealized crack shape assumption. In Section XI analyses, standard K-solutions are used to analyze indications found in service. In addition, in most probabilistic piping leak/rupture fracture mechanics codes, this same assumption is employed. These K-solutions are developed through detailed elastic finite element analyses of idealized cracks in pipes. Surface cracks are usually modeled with a semi-elliptical assumption and through-wall cracks are modeled with a radial crack front. As discussed in Section 5.1, the Phase I result of this program strongly suggested that the semi-elliptical surface crack assumption is highly conservative when considering the combination of loads used in this program. Therefore, eliminating this conservatism is a large step toward improving predictions of both leakage and rupture.

6.1.2   Detailed WRS solutions

Even though Section XI requires that inclusion of welding residual stress in the crack growth analyses, there is no guidance on how to calculate these values. ASME Section XI IWB-3460 contains an approximation for through-thickness welding residual stresses. However, this WRS was for BWR piping and was actually measured from the sensitized HAZ of the lower strength stainless steel pipe and not the higher strength Alloy 182 weld metal. Currently, weld metal WRS fields are not available in the Code.   In this program, geometry specific welding residual stress analyses were conducted for both unrepaired and repaired geometries.   These analyses were conducted not only by the industry, but also by Emc^2. Having this type of information for the subcritical crack growth analyses greatly increases the reliability of these predictions.

6.1.3   Predictions of leak rate using FE calculated COD

In typical Section XI-type analyses, J-estimation schemes are used to predict the crack opening displacement needed for leak-rate analyses. These estimation schemes are based on idealized type cracks and may not represent the true crack opening. In the current analyses, the crack opening displacements used in the leakage calculations were extracted directly from the advanced finite element model results. Therefore, the elastically calculated crack opening for the complex leaking cracks was used in making leakage predictions. This is significant improvement over using crack opening displacements based on estimation scheme predictions. However, for very large cracks, elastic-plastic FE analyses are needed for accurate predictions of the COD. Using the elastic COD values would underpredict the leak rate for large flaws.

6.1.4   Sensitivity analyses

To account for the differences in the load for these specific plants, the sensitivity analyses include cases where the load was varied for each geometry. An industry survey was conducted and a range of design loads was developed for each nozzle configuration. Calculations were performed varying the bending and membrane stresses and their impact on the margins and leak rates was addressed. This comprehensive look at the loads is an improvement over flaw analyses where only one set of loading is considered.

6.2   Conservatisms

In addition to the improvements made to the standard crack growth analyses, there were several major conservatisms that were present in these analyses. These conservatisms add confidence to the calculated times between leakage and rupture.

6.2.1   Use of stainless steel base metal flow strength properties in critical crack size calculations

As discussed in Section 2.2, the critical crack size calculation in this project was based on the Net-Section-Collapse criteria for arbitrary shaped flaws, with a Z-factor adjustment to account for elastic-plastic fracture. Analyses conducted by Emc^2 in another effort [8], show that for the analyses conducted the appropriate stress-strain curve to use in analyzing flaws in DM welds is a function of the location of the flaw within the weld, i.e., distance relative to the base metal. These analyses also indicated that if the crack was near the stainless steel safe end, the lower strength stainless steel controlled the failure. In the analysis of postulated defects presented in Section 5, it was assumed that the stainless steel base metal flow properties controlled the collapse of the pipe net section. The welding residual stress analyses conducted suggest that the

highest ID stress is within the buttered region, which is closer to the higher strength carbon steel than the lower strength stainless steel. Therefore, using the stainless steel flow properties in the Net-Section-Collapse analyses is conservative for predicting the failure of cracks in the buttered region of DM welds.

The degree of conservatism can be illustrated by the example shown in Figure 59. In this case, the flow stress was modified per Reference 1. In the modified case, the crack was assumed to be in the center of the weld. This gave an appropriate flow stress that was between that of the stainless steel safe end and the nozzle material. This result indicates that the load margin on critical crack size is increased by about 13 percent. If the crack was closer to the carbon steel nozzle, the margin may be increased by as much as 17 percent. In order to reduce the conservatism, it is appropriate to increase the critical crack size load margin by 13% to account for the actual flow stress that will control collapse for flaws in the butter region.
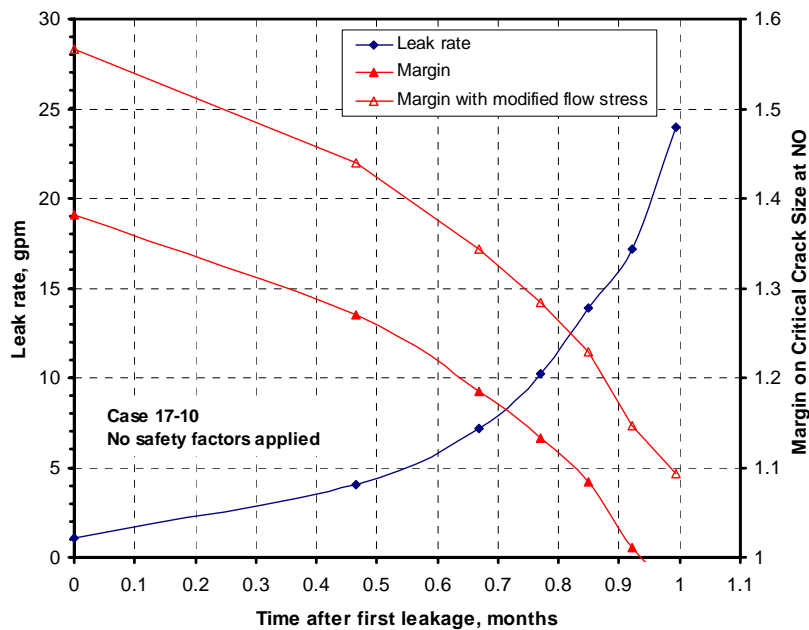
Figure 59 Comparison of results for Case 17-10 with a modified flow stress

6.2.2   Secondary stress relief

The industry conducted analyses that show that displacement-controlled stresses on the cracked pipe section are relieved due to the rotation of the crack before the cracked section becomes critical. In one case (Appendix B of Reference 2), an elastic surge-line piping analysis was conducted with all of the appropriate displacement-controlled stresses. Rotational degrees of freedom were released from the node at the DM weld location, and the resultant rotation was 2 degrees. Some experimental results for complex cracks suggest that maximum load was reached at a 2 degree rotation, suggesting that the maximum displacement-controlled loads can not take the pipe beyond the critical rotation. In other analyses (Appendix C of Reference 2), idealized through-wall cracked pipes were analyzed with different simulated compliances with both load controlled and displacement-controlled moments using elastic-plastic finite element analyses. These results show that the reduction in the displacement-controlled stresses was a function of the system compliance and the size of the crack, indicating that for these analyses the

63

displacement-controlled loads would be relaxed as the crack length is increased. In addition, when the crack reached about 50 percent of the circumference, the elastic-plastic J-integral along the crack began to approach zero compared to the high elastic value of J. This point again supports a reduction in the displacement-controlled stresses as the crack reaches limit conditions.

As noted earlier, in all of these analyses, the normal thermal loads were used, and the higher transient thermal stratification stresses were assumed to be relaxed. Figure 2-10 of Reference 2 shows a ratio of the normal thermal loads to the limiting thermal loads for each of the nine plants. The results are presented in this figure for membrane stress only, bending stress only and bending plus membrane. If the bending only data (since the largest contributor to displacement-controlled stresses is bending) is investigated, it shows that on average, for the plants in question, the normal thermal loads are about 59 percent of the limiting thermal loads. For most cases conducted by DEI and Emc^2, the cracked area at critical size ranged from 50 to 60 percent of the pipe cross-sectional area, which would illustrate from Figure C-10 of Appendix C of Reference 2 that the appropriate moment knock-down factor would be between 40 and 50 percent[‡‡‡]. Therefore, on average, using only the normal thermal loads in the analysis would be conservative. On a plant specific basis, from Figure 2-10 of Reference 2, it can be seen that Plants B, G, H and I were conservatively analyzed using the normal thermal stresses only. The analyses of Plants C, D and E were only slightly conservative since the normal thermal bending loads were between 40 and 50 percent of the limiting thermal bending load. Plant A seems to be the least conservative, since its normal thermal bending loads are only 26 percent of the limiting thermal bending loads. However, Plant A is bounded by Plant G, which has the same overall nozzle geometries and higher loads.

6.2.3 *No credit taken for transition time to leaking TWC*

In these analyses, as the growing surface crack approaches through-wall penetration, an assumption is made in the shape of the resulting through-wall crack at the OD surface. Due to meshing difficulties, any ligament that is less than 5-10 percent of the thickness is eliminated. If the surface crack is stable, and the material is tough, the local ligament ahead of the crack may be very small before local ligament instability occurs. By making the assumption that the crack goes through-wall when its depth reaches between 90 and 95 percent of the thickness, no credit is taken for the transition time.

6.2.4 *Initial flaw size*

One of the main assumptions in these analyses is that there is one flaw and that flaw is centered on the maximum moment. The flaw sizes chosen for these analyses was relatively large, i.e., either a 21:1 flaw with a depth of 26% of the wall thickness or a 360 degree flaw with a depth of 10 percent of the wall thickness. These size flaws were chosen to attempt to conservatively account for multiple crack initiations. Using this assumption will lead to very conservative times to leakage. However, for most of the cases (excluding the surge nozzle), the choice of initial crack size did not affect the shape of the crack at first leakage; therefore it would not affect the margin between leakage and rupture.

[‡‡‡] This result also assumed that a complex crack and a through-wall crack with a 50 percent cracked area have the same elastic-plastic behavior, and the pipe system compliance is properly accounted for by the 60 foot straight pipe assumption.

6.3 Uncertainties

Even though there were many improvements and advancements made to the crack growth analyses in this program, there are still a considerable number of uncertainties that need to be addressed. The impact of these uncertainties can be addressed in sensitivity analyses in some cases, while others may need to be addressed by the use of safety factors.

6.3.1 *Leak-rate calculations*

The calculations of leak rate for this program were conducted using SQUIRT, as described in Section 2.3. The industry used the PICEP code to perform similar calculations. The industry also did a quick sensitivity study with SQUIRT that indicated if the exact same parameters were used, SQUIRT gave higher leak rates.

The SQUIRT code has been validated against laboratory experiments for slits, smooth cracks and IGSCC-type defects [13]. In this validation effort, it was shown that the predicted leak rates fall within a factor of 2 for leak rates greater than about 0.1gpm and within a factor of 10 for leak rates lower than 0.1 gpm. A statistical analysis [2] conducted by David Harris as part of the expert panel for this program, suggested that 95th percentile for leak rate predictions for IGSCC cracks is between 1.5 and 2 for leak rates greater than 0.1 gpm. This result indicates that the leak rate for IGSCC cracks can be predicted within a factor of 1.5-2.0 95% of the time.

However, these leak rates were predicted using well defined and well measured crack morphology parameters. Crack morphologies for SCC flaws should be treated in a statistical manner since the measurement of the morphology parameters used in generating the mean values in Table 1 was carried out on a limited number of samples [20]. Therefore, there is uncertainty in the leak rate calculations associated with statistical variations in the crack-morphology parameters. This affect was also investigated in Reference 36.

Finally, the leak rate validation for actual cracks did not consider the flow across the complex shape of cracks developed in this effort. Both the SQUIRT and PICEP codes assume that the crack has a certain defined shape and that the crack length and COD are equal on the ID and OD (PICEP), or the crack length and COD through thickness is linear between the inputted values on the ID and OD (SQUIRT). As noted in Section 2.3.3, the results from the finite element analyses suggest that the actual crack opening shape is not idealized. In addition, so far there are no experimental results with leak rates from complex crack shapes to definitely know how this unique crack shape affects the flow rate.

6.3.2 *Welding residual stress*

As mentioned earlier, the use of geometry specific welding residual stresses in the crack growth analyses is a large improvement over using the welding stresses presented in the ASME Section XI code that was based on data from IGSCC in HAZ of BWR welds. However, there are uncertainties associated with the use of these case specific welding stresses.

First of all, the stress analysis procedures for predicting welding residual stress in DM welds have not been fully validated. Some comparisons have been performed as part of this effort, and others are planned for the future, but a robust validation is not available at this point. In addition, for the comparison conducted, the differences between not only analyses and the experimental

results, but between the different analyses results is quite large. In fact, for all of the participants in the EU round robin, DEI, Emc^2 and Battelle, the scatter (see Appendix A) in the predictions had a range of approximately 20ksi. This is a considerable uncertainty for a problem that was well defined, and well laid out.

In addition, how the current methodology incorporates the calculated welding stresses may add uncertainty to the final results. As described in Section 2.1, the advanced finite element model using a thermal gradient to simulate the welding stress on the crack plane, and applies this thermal gradient for a 2-inch axial extent. The transition of the stresses from the cracked plane to the far field pipe body is fully defined by the equilibrium state of the model. No comparisons were conducted between the predicted stresses away from the crack plane and those calculated in the welding residual stress model. In one case, an analysis was done where the thermal gradient was applied for only a 1-inch axial extent. This case showed a slight decrease in the margin and illustrated the sensitivity of the results to the stress decay away from the crack plane. The level of uncertainty in this case has not been quantified, but is assumed to have a secondary affect on the results.

6.3.3   Crack growth predictions

The crack growth law used in these analyses was developed by the MRP [34] from a series laboratory sized specimens under well controlled conditions. Since there was a great deal of scatter in the data, a 75th percentile crack growth rate was used as the baseline in these analyses. As a way to address the scatter in the data, DEI conducted sensitivity studies on this issue by using the 95th percentile crack growth rate from the same data. As expected, the margin between leakage and rupture was decreased when the higher crack growth law was employed. However, this procedure to use the laboratory crack growth rates for modeling the behavior of a surface crack in a pipe growing due to PWSCC is not validated. Issues with penetration of the water to the tip of the crack for deep surface cracks by either the tightness of the cracks or corrosion product plugging can make the behavior significantly different than predicted using the laboratory growth rates.

Another assumption in these analyses that adds to the uncertainty in the results is the shape of the crack at through-wall penetration. In Reference 2, it is explained that if any surface crack reaches a depth of 93 percent of the thickness, it is converted to a through-wall crack with any section of the ligament less than 10 percent being removed in the development of the through-wall crack. As illustrated in Figure 4-4 of Reference 2, the resulting through-wall cracks at the OD surface is not necessarily radial, but is probably set for ease of meshing. As described in Section 2.1 of this report, PipeFracCAE transitions a surface crack to a through-wall crack a little more naturally, with the crack front having a shallower angle than that estimated by FEACrack. These differences will produce different stress intensity factors at the OD surface, which will control the growth around the circumference and directly affect the margin.

In addition, the K-values that occur for these complex-type cracks are very high, which may invalidate the linear elastic fracture assumption and the crack growth rate based on K. This possibility adds uncertainty to the analysis results.

6.3.4 Critical crack size

In this effort, the methodology used for the prediction of critical crack size was based on a Z-factor approach for through-wall cracks in DM welds. However, the lack of experiential data for cracks in DM welds adds to the uncertainty in these analyses. The only through-wall crack experiment on a DM weld is cold-leg experiment where a through-wall crack was placed on the fusion line. That experiment showed a Z-factor about equal to those predicted in Reference 8. This lack of experimental data is especially true for complex cracks in DM welds. Past data [9] suggests that the tearing resistance for complex cracks is greatly reduced as compared to through-wall cracks with the same OD crack length. However, the contention by the industry is that these Alloy 182 DM welds are very tough and will not demonstrate the reduction in tearing resistance seen in past tests. So far there is no appropriate experimental data to confirm this statement.

In addition, the treatment of secondary stresses in this effort lends itself to a certain amount of uncertainty. Analyses conducted by the industry indicate some of the displacement controlled stresses would be relieved before the complex crack reaches a limit state. However, the true amount of reduction is unclear since the secondary stress analyses conducted by the industry were based on simplified assumptions. However, based on the results of the analyses in Appendix A and B [2], it is reasonable to consider a reduction in the secondary stresses up to approximately 50 percent.

6.3.5 Crack path

One additional uncertainty in these analyses comes from the assumption that the crack remains planar as it subcritically grows. Typical PWSCC is intergranular and will by definition not follow a straight path. The crack may actually grow faster if allowed to grow non-planar since the most susceptible grain boundaries and the true highest stress will be followed. However, this is very difficult to model, and can be considered secondary in nature.

6.4 Applicability of Methodology

The methodology developed by the NRC staff, Emc[2] and the industry is a large step forward in improving the predictions of crack growth, leakage, and margin for PWSCC cracking in DM welds. The elimination of the semi-elliptical crack-shape assumption significantly reduces the conservatisms in the margin between leakage and rupture predictions, especially for the smaller diameter piping systems. In addition, the detailed welding residual stress solutions developed, and the use of FE predicted COD values in the leak-rate calculations, coupled with the conservatisms in the critical crack size calculations and initial flaw size assumptions add confidence to the results generated.

However, as with any model that is not fully validated, associated uncertainties exist. The residual stress solutions, the crack growth and crack stability models are not fully validated by full-scale experiments. In addition, even though the leak-rate codes have had some SCC validation, leak-rate experiments with PWSCC cracks have not been conducted, and the uncertainty in the PWSCC crack morphology parameters has not been addressed. NRC staff, the industry and Emc[2] used their best engineering judgment to reduce the uncertainties used in this advanced FEA model. As a result, the methodologies developed in this program provide a better and more realistic predictive tool for evaluating flaws in service.

Overall, the methodology developed is applicable for making reasonably accurate predictions of leakage and rupture for active PWSCC cracks in butt welds. The improvements developed in this effort add confidence in the results generated. From a technical point of view, in an assessment of these results relative to the nine subject plants scheduled to perform PDI inspection during the Spring 2008 outage season, the associated uncertainties can be addressed by safety factors.

7. Summary

This report documents the effort conducted by Emc[2] aimed at confirming the industry's results of their advanced FEA evaluation of growth of postulated PWSCC cracks in pressuizer nozzle DM welds. In this effort, Emc[2] independently developed a crack growth computer code, PipeFracCAE, for simulating arbitrary PWSCC growth from an initial flaw size to rupture, simulated welding residual stress in several pressurizer nozzle DM weld locations, verified the industry's FEACrack software by conducting similar analyses with PipeFracCAE, and conducted independent sensitivity studies on critical cases from the industry's sensitivity matrix.

The results from this study confirm the industry's results in that the same trends and behaviors were predicted. However the specific results were slightly different between the Emc[2] and DEI analyses. For a 1gpm crack size, the Emc[2] analyses gave slightly (7%) higher load margins on critical crack size. These are reasonable differences for the differences in assumptions made by Emc[2] and DEI. However, the biggest differences were seen in the time between the 1gpm leakage and when the crack has a margin of 1.2 on the failure stress. For this case, on average, the DEI results are higher than the Emc[2] results by 30 percent. These differences appear to come from the approximation of crack front shape at first leakage.

Overall, the applicability of this methodology for predicting the leak/rupture response of PWSCC in DM butt welds is greatly improved over the typical ASME Section XI-type analysis. Removal of the semi-elliptical crack front assumptions is the largest contributor to this improvement, but the addition of detailed WRS solutions, COD measurements made directly from the FE models, and the detailed sensitivity matrix all add to the confidence in this methodology. However, even though there is conservatism in this analysis procedure, some uncertainty exists. NRC staff, the industry and Emc[2] used their best engineering judgment to reduce the uncertainties used in this advanced FEA model. As a result, the methodologies developed in this program provide a better and more realistic predictive tool for evaluating flaws in service.

8. References

1   Rudland, D.L., Shim, D-J., Xu, H., and Wilkowski, G.W., "Evaluation of Circumferential Indications in Pressurizer Nozzle Dissimilar Metal Welds at the Wolf Creek Power Plant," Summary report to the NRC, April 2007.
2   Materials Reliability Program: Advanced FEA Evaluation of Growth of Postulated Circumferential PWSCC Flaws in Pressurizer Nozzle Dissimilar Metal Welds (MRP-216, Rev. 1) EPRI, Palo Alto, CA: 2007. 1015383.MRP-216, Rev. 1.

3   ABAQUS Users Manual, Version 6.6, Hibbit, Karlsson & Sorensen Inc., Pawtucket, Rhode Island, USA, 2006.

4   Materials Reliability Program (MRP) Crack Growth Rates for Evaluating Primary Water Stress Corrosion Cracking (PWSCC) of Alloy 82, 182, and 132 Welds (MRP-115), EPRI, Palo Alto, CA: 2004. 1006696.MRP-115

5   Wilkowski, G. M., Olson, R. J., and Scott, P. M., "State-of-the-Art Report on Piping Fracture Mechanics," U.S. Nuclear Regulatory Commission report NUREG/CR-6540, BMI-2196, February 1998.

6   "Evaluation of Flaws in Austenitic Steel Piping," (Technical basis document for ASME IWB-3640 analysis procedure), prepared by Section XI Task Group for Piping Flaw Evaluation, EPRI Report NP-4690-SR, April 1986.

7   "Evaluation of Flaws in Ferritic Piping," EPRI Report NP-6045, prepared by Novetech Corporation, October 1988.

8   G. Wilkowski, H. Xu, D.-J. Shim, and D. Rudland, "Determination of the Elastic-Plastic Fracture Mechanics Z-factor for Alloy 82/182 Weld Metal Flaws for Use in the ASME Section XI Appendix C Flaw Evaluation Procedures," Proceedings of ASME-PVP 2007, paper PVP2007- 26733, July 22-26, 2007.

9   Wilkowski, G., Rudland, D.L., Shim, D-J, and Xu, H., "Critical Flaw Size Evaluations for Circumferential Cracks in Dissimilar Metal Welds," Technical note, prepared for the NRC by Emc[2], April 9, 2007.

10   S. Rahman, G. Wilkowski, "Net-Section-Collapse Analysis of Circumferentially Cracked Cylinders—Part I: Arbitrary-Shaped Cracks and Generalized Equations," *Engineering Fracture Mechanics*, Vol. 61, pp. 191-211, 1998.

11   P. Scott and others, "The Battelle Integrity of Nuclear Piping (BINP) Program Final Report," NUREG/CR-6837, Volumes 1 and 2, June 2005.

12   G. Wilkowski, P. Scott, R. Olson, and D. Rudland, "Effect Of Secondary Stresses On Pipe Fracture," Paper PVP2005-71330, Proceedings of ASME-PVP 2005 ASME/JSME Pressure Vessels And Piping Conference, Denver Colorado, July 17-21, 2005.

13   "User's Guide for SQUIRT (Windows Version 1.1)," Battelle Memorial Institute, March 2003.

14   Scott, P.M., Ghadiali,N., Paul,D., Morbitzer, R., Rudland, D., and Wilkowski, G., "Technical Development of Loss of Coolant Accident Frequency Distribution Program, Subtask 1a: Finalize and QA SQUIRT Code," Final report to Nuclear Regulatory Commission, March 2003.

15   Paul, D., and others, "Evaluation and Refinement of Leak-Rate Estimation Models," NUREG/CR-5128, Rev. 1, June 1994.

16   El-Wakil, M., M., *Nuclear Heat Transport*, International Text Book Company, Copyright 1971, Page 362, Figure 12-21.

17   Rahman, S., Ghadiali, N., Paul, D., and Wilkowski, G., "Probabilistic Pipe Fracture Evaluations for Leak-Rate Detection Applications," NUREG/CR-6004, April 1995.

18   Rudland D.L., Wilkowski, G., and Scott, P., "Effects of Crack Morphology Parameters on Leak-rate Calculations in LBB Evaluations," *International Journal of Pressure Vessels and Piping*, 79 (2002) 99-102

19   Kupperman, D.S., Sheen, S.H., Shack, W.J., Diercks, D.R., Krishnaswamy, P., Rudland, D., and Wilkowski, G.M., "Barrier Integrity Research Program," NUREG/CR-6861, ANL-04/26, December 2004.

20   Rudland D., Wolterman, R. and Wilkowski, G., "Impact of PWSCC and Current Leak Detection on Leak-Before-Break," Emc^2 final report to NRC, January 31, 2003.

21   Anderson, T.L., Thornwald, G., Revelle, D.A., and Lanaud, C., "Stress Intensity Solutions for Surface Cracks and Buried Cracks in Cylinders, Spheres, and Flat Plates," Structural Reliability Technology final report to The Materials Property Council, Inc., March 14, 2000.

22   "Phase I Pressurizer Nozzle Dissimilar Metal Weld Crack Growth Calculations Using Advanced FEA," Draft B, Dominion Engineering, Inc., March 2007

23   Shih, C.F., and R.J. Asaro, "Elastic-Plastic Analyses of Cracks in Bimaterial Interfaces: Part I – Small Scale Yielding," Journal of Applied Mechanics, pp. 299-316, 1988.

24   Y.-Y. Wang, Z. Feng, W. Cheng, and S. Liu, "Residual Stress Effects on Crack Driving Force in Multipass Welds," *Pressure Vessel and Piping (PVP) Conference*, San Diego, CA, July, 1998.

25   C. L. Tsai, S. C. Park, and W. Cheng, "Welding Distortion of a Thin-Plate Panel Structure," *Welding Journal*, Vol. 78 No. 5, May 1999, pp. 156s-165s.

26   Z. Feng, X. Wang, C. R. Hubbard, and S. Spooner, "A FE Model For Residual Stresses In Repair Welds," *Residual Stresses in Design, Fabrication, Assessment and Repair*, ASME PVP-Vol. 327, 119-125, 1996.

27   H.D. Hibbitt and P.V. Marcal, "A Numerical, Thermo-Mechanical Model for the Welding and Subsequent Loading of a Fabricated Structure, "*Computers & Structures*, Vol. 3, 1145-1174, 1973.

28   K. W. Mahin, W. Winters, T. M. Holden, R. R. Hosbons, and S. R. MacEwen, "Prediction and Measurement of Residual Elastic Strain Distributions in Gas Tungsten Arc Welds," *Welding Journal*, Vol. 70, 245s-260s, 1991.

29   J. Goldak, A. Chakravarti, and M. Bibby, "A New Finite Element Model for Welding Heat Sources," *Metall. Trans.,* Vol. 15B, 299-305, 1984.

30   Chen, Y., Rudland, D., and Wilkowski, G., "Impact of Welding Sequence on the CRDM Nozzle-to-Vessel Weld Stress Analysis," Proceedings of ASME-PVP 2004: ASME/JSME Pressure Vessels And Piping Conference, Hyatt Regency, La Jolla at Aventine, San Diego, California, July 25 – 29, 2004

31   D. Rudland, G. Wilkowski Y.-Y. Wang, and W. Norris, "Analysis of Circumferential Through-Wall Crack K-solutions for CRDM Nozzles," *International Journal of Pressure Vessels and Piping*, 81 (2004) pp. 961-971

32   Assessment of Dissimilar Metal Weld Integrity: Final Report of the NESC-III Project, EUR 22510 EN, European Commission Joint Research Centre, 2006.

33   NESC-III Project, TG6 2nd (Detailed) Computational Round Robin, NESCDOC TG6 (04) 01, Rev. 2, February 26, 2004

34   Materials Reliability Program (MRP) Crack Growth Rates for Evaluating Primary Water Stress Corrosion Cracking (PWSCC) of Alloy 82, 182, and 132 Welds (MRP-115), EPRI, Palo Alto, CA: 2004. 1006696.

35   Dominion Engineering, Inc., "Supplemental cases S10a and S10b to August 2, 2007 Final Report (MRP-216)," Supplemental presentation slides dated August 6, 2007.

36   Rahman, S., Ghadiali, N., Paul, D., and Wilkowski, G., "Probabilistic Pipe Fracture Evaluations for Leak-Rate-Detection Applications," NUREG/CR-6004, April 1995

Appendix A – EU Welding Residual Stress Validation Results

A.1 Introduction

This appendix describes the Emc^2 effort to simulate the welding residual stress for a dissimilar metal (DM) weld mock-up that was fabricated by the European Commission Joint Research Centre's (JRC) Institute for Energy. The EU project [1] investigated a wide range of issues related to the structural integrity assessment of a stainless steel weld joining stainless steel and low alloy steel components. Also in this effort, a series of round-robin exercises that compared predicted welding residual stress distributions to those measured from the aforementioned welded joint mockup. Complete details of the mockup geometry, welding process, and material properties were made available to all participants in the round-robin. The welding residual stress analysis results for each participant were compared to the through-wall stresses measured by neutron diffraction (ND).

In this effort, the problem statement [2] that was delivered to the EU round-robin participants was used by Battelle, Emc^2, and DEI for conducting similar analyses. Each company conducted an independent analysis of the welding stresses. The results from each lab are compared here, but the details of the DEI [3] and Battelle [4] analyses can be found elsewhere.

A.2 Welding Procedure

Per the problem statement [2], the five steps of the manufacturing process included:

Step 1: Buttering
The ferritic pipe (A508) had an external diameter of 473mm, a wall thickness of 69mm and was about 530mm long. One side of the pipe was machined with a bevel of 25 degrees. The buttering layer consisted of four layers of weld passes using an E308/E309 stainless steel welding electrode, having a total thickness of 12mm. The total number of weld passes was 72.

Step 2: Buttering machining
After the buttering process, the ferritic pipe was machined so that the diameter of the pipe was 467mm with a wall thickness of 64mm. The buttering was also machined down to a final thickness of 7.2mm.

Step 3: Welding
The two pipes, austenitic pipe and ferritic pipe, were held together by spot welds. The austenitic pipe had an external diameter of 467mm, a wall thickness of 73mm and was about 510mm long, having one end machined with a 25 degree bevel. The total number of weld passes was 97.

Step 4: Post Weld Heat Treatment
After welding, the assembly was allowed to cool to room temperature. A heat treatment process was then performed on the entire assembly using an electric resistance furnace.

Step 5: Final Machining
After post-weld heat treatment, the pipe was machined to have a final external diameter of 453mm with a wall thickness of 51mm.

A.3   Emc^2 Finite Element Model

An axi-symmetric finite element model of the weld mock-up was developed and is shown in Figure 1. There were 72 butter weld passes modeled as shown in Figure 2. For this time critical analysis, it was decided to lump several of the butter weld passes in order to increase the computational efficiency of the analysis. The lumped butter weld passes are shown in Figure 3. The total number of the lumped butter weld passes is 15. Figure 3(b) shows the mesh after butter machining (Step 2). The finite element mesh after main welding (Step 3) is presented in Figure 4(a). There were 97 weld passes modeled which were lumped into 20 weld passes as shown in Figure 4(b) to increase the computational efficiency of the analysis. Figure 5 is the mesh after final machining (Step 5). In this model, the total number of 8-noded axi-symmetric elements is 11,000 and the total number of nodes is 12,000. The welding analysis procedures described in Section 4.2 of the main body of the report were used in conducting this analysis.

A.4   Material Properties

In this effort, the DM weld was a stainless steel (308L/309L) connecting a 316L stainless pipe to an A508 carbon steel pipe. This weld is slightly different than the Alloy 182 weld modeled in the main body of this report; however, this weld will serve the purpose of initially validating the welding stress predictions. In the EU report [1], some details of material property values as a function of temperature were available; however, full-stress strain curves were not available. Therefore, it was decided to use the material properties that were available from the analyses conducted in the main body of this report. Since some of the material property data (308/309) needed for this analysis were not used in the main body of the report, the material property data used by Battelle in the VC Summer analysis [5] were used to supplement the data from the main body of the report. Upon comparison, these data are similar to those presented in the EU report.

A.5   Boundary Conditions

The boundary conditions used in the model were selected to match the mock-up procedures. The mock-up was welded on rollers with no axial constraint. These conditions were simulated in the analysis.

A.6   Analysis Assumptions

As with most welding simulation analyses, modeling assumptions are necessary to conduct the analyses in computationally accurate, yet efficient manner. The following assumptions were used in this analysis:

- Mechanical and structural responses are axi-symmetric,
- Effects of weld pass lumping were neglected,
- Elasto-plastic and temperature-dependent material behaviors were included for all the parts involved,
- Stress relaxation due to creep during the heat-treatment process was ignored,
- Element remove and add techniques were used to model weld passes deposit and material machining. Effects of local cold work from the machining process were ignored.
- Metallurgical phase transformation of heat affected zone material was ignored.

A.7   Results and Discussions

The welding residual stress contours after completing the five steps described above are shown in Figure 6 for axial stress and Figure 7 for hoop stress. These results are typical for multi-pass welds. A direct comparison of results between Emc^2, DEI and Battelle[i] are given in Figure 8 through Figure 15. In the first four figures, the results from all three participants are shown; however, only Battelle and Emc^2 results are shown for the last four figures since DEI did not provide results for these paths. Overall, the trends between the three participants were identical, with the Battelle and Emc^2 closer to each other on average. The largest difference comes at 4.25mm from the OD at the weld centerline. In this case, the Emc^2 axial stress is much less than the Battelle or DEI results. It is suspected that the lumping and weld sequencing differences may be contributing to the observed trends.   The axial stresses along the butter centerline are very close for all three cases. This is encouraging since these stresses are usually chosen as the highest stresses in DM weld analyses.   This trend suggests that the differences in the modeling assumptions did not highly influence the axial stresses in the butter region.

A comparison of the Emc^2 results with the EU participant results are shown in Figure 16 through Figure 31. These cases include each path through the weld taken by the EU participants. As with the comparison with DEI and Battelle, the Emc^2 results follow the same trends as the EU participants in all cases. As before, the largest difference occurs at the weld centerline between 4 and 12 mm from the OD surface. Again, this difference is probably due to the modeling differences.

Overall, the scatter between the predictions is on average between 50MPa and 100MPa. When comparing the prediction to the ND measurements, the analyses usually capture the trends and sometimes the magnitudes measured. However, it is necessary to mention that the measured ND hoop stresses are considered more reliable and complete than those in the axial direction, as pointed out in EU report [1]. In addition, the measurements near the OD are more reliable than the ID measurements since the neutron source was only used on the OD surface.

This quick study is the first step at the validation of the welding residual stress procedures and has shown that the Emc^2, Battelle and DEI procedures give generally the same results. In addition, those analysis results match reasonably well with ND measurements and other analyses results from the same problem.

A.8   References

1   Assessment of Dissimilar Metal Weld Integrity: Final Report of the NESC-III Project, EUR 22510 EN, European Commission Joint Research Centre, 2006.
2   NESC-III Project, TG6 2nd (Detailed) Computational Round Robin, NESCDOC TG6 (04) 01, Rev. 2, February 26, 2004
3   Materials Reliability Program: Advanced FEA Evaluation of Growth of Postulated Circumferential PWSCC Flaws in Pressurizer Nozzle Dissimilar Metal Welds (MRP-216) EPRI, Palo Alto, CA: 2007. 1015383.MRP-216

---

[i] The Battelle results presented here are for the case where the stress relaxation due to creep is ignored.   Battelle conducted their analyses with and without relaxation during the heat-treatment process.

4   Brust, F., and Scott, P., "Modeling Results of European Commission Dissimilar Weld Mock-up (NESC-III Project)," Report to the NRC, July 2007.

5   P.Scott, R.Olson, J.Bockbrader, M.Wilson, B.Gruen, R.Morbitzer, Y.Yang, Williams , F. W. Brust, L.Fredette, N.Ghadiali, G.Wilkowski, D.Rudland, Z.Feng, R.Wolterman, 'The Battelle Integrity of Nuclear Piping (BINP) Program Final Report', NUREG/CR 6837, Volumes I and II, June, 2005.

Figure 1 Axi-symmetric finite element model
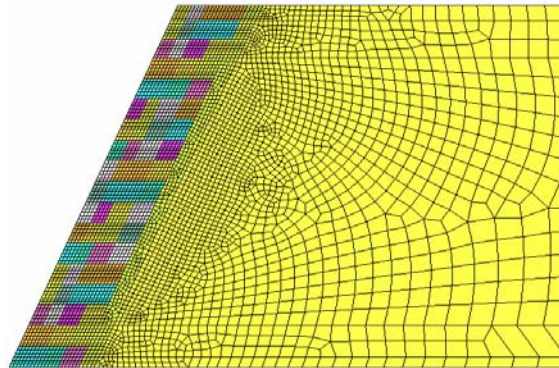
Figure 2 Buttering finite element model before buttering machining

| (a) | (b) |
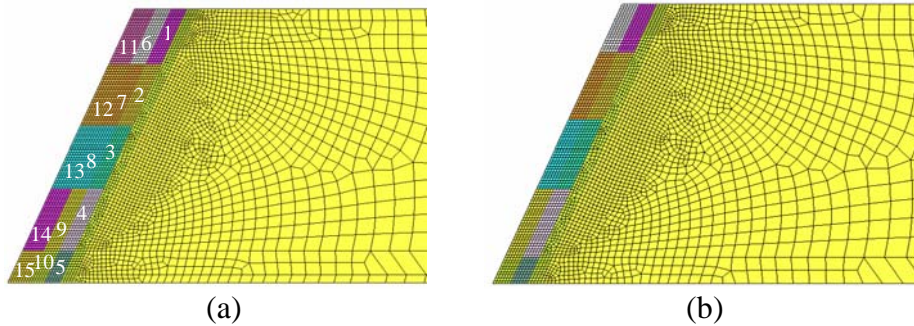
Figure 3 Buttering (lumped) finite element model (a) before buttering machining (b) after buttering machining

(a)　　　　　　　　　　(b)
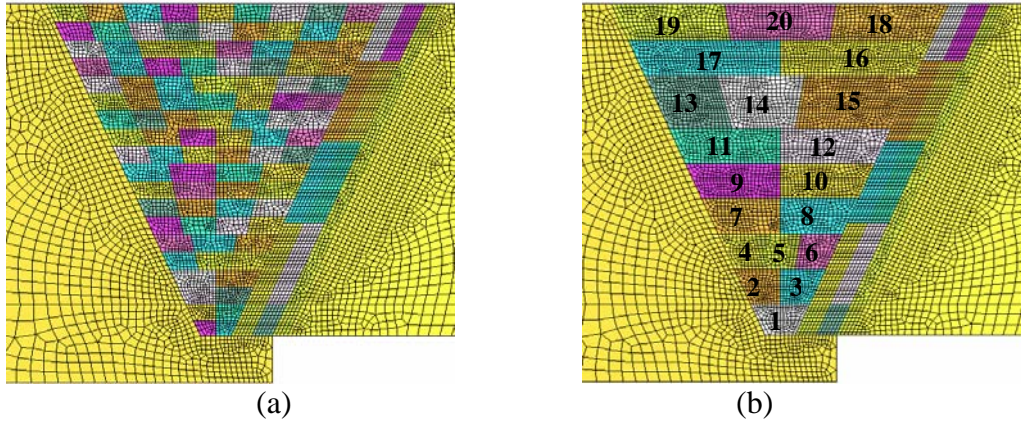
Figure 4 Finite element mesh of weld (a) without lumping (b) with lumping
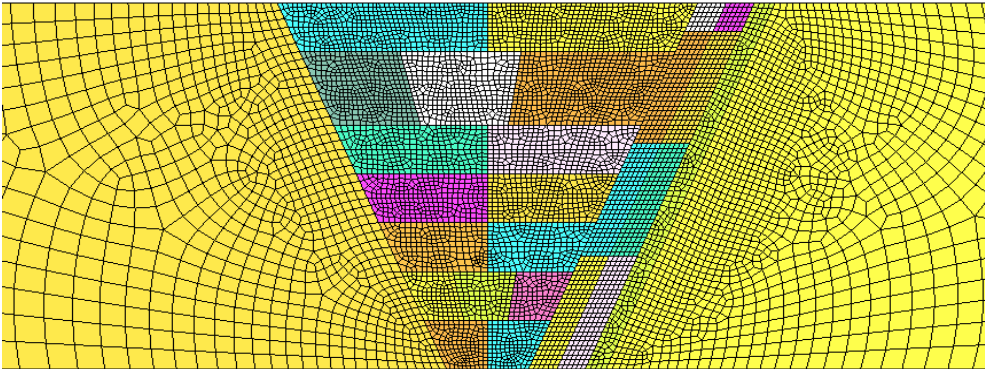
Figure 5 Finite element mesh after final machining
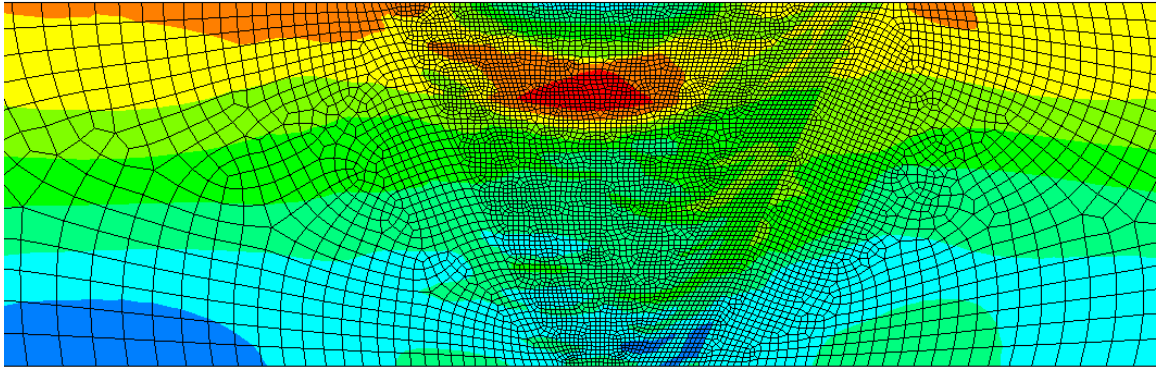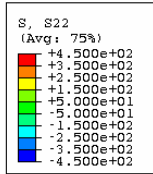
Figure 6 Contour plot of axial stress after final machining
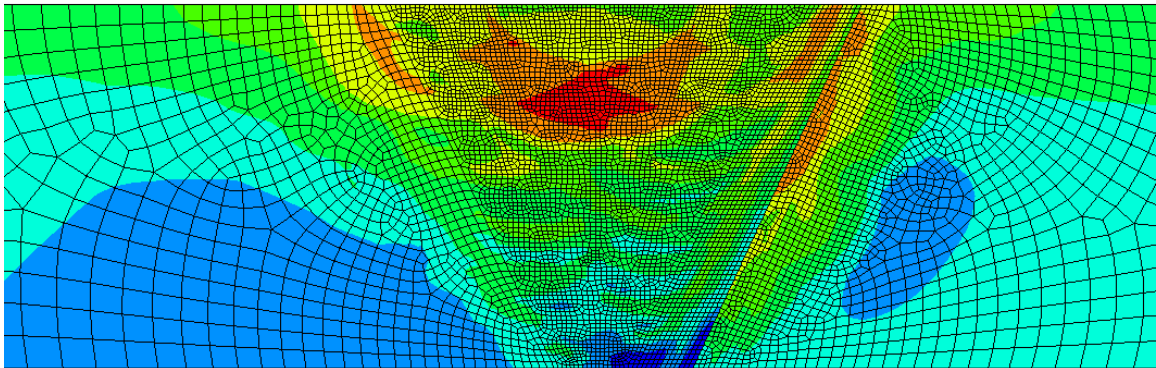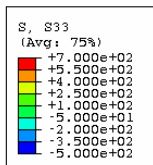
Figure 7 Contour plot of hoop stress after final machining
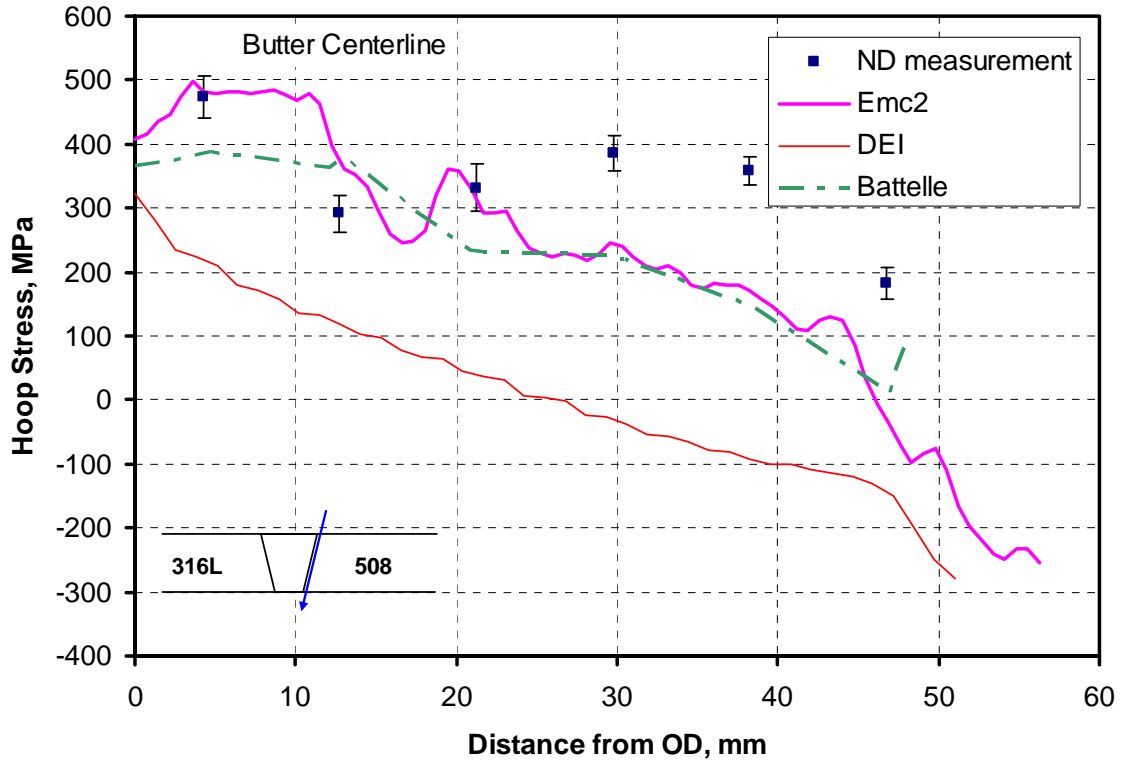
Figure 8 Residual hoop stress comparison with DEI and Battelle along butter center
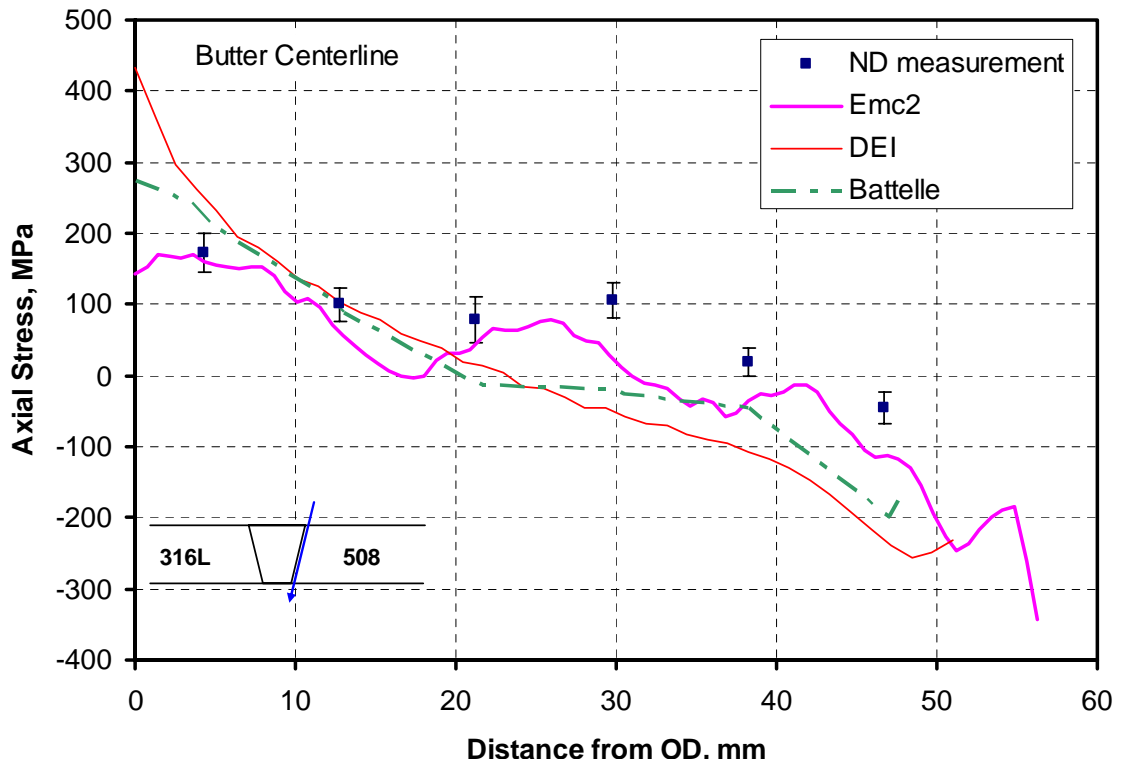
Figure 9 Residual axial stress comparison with DEI and Battelle along butter center

A-9
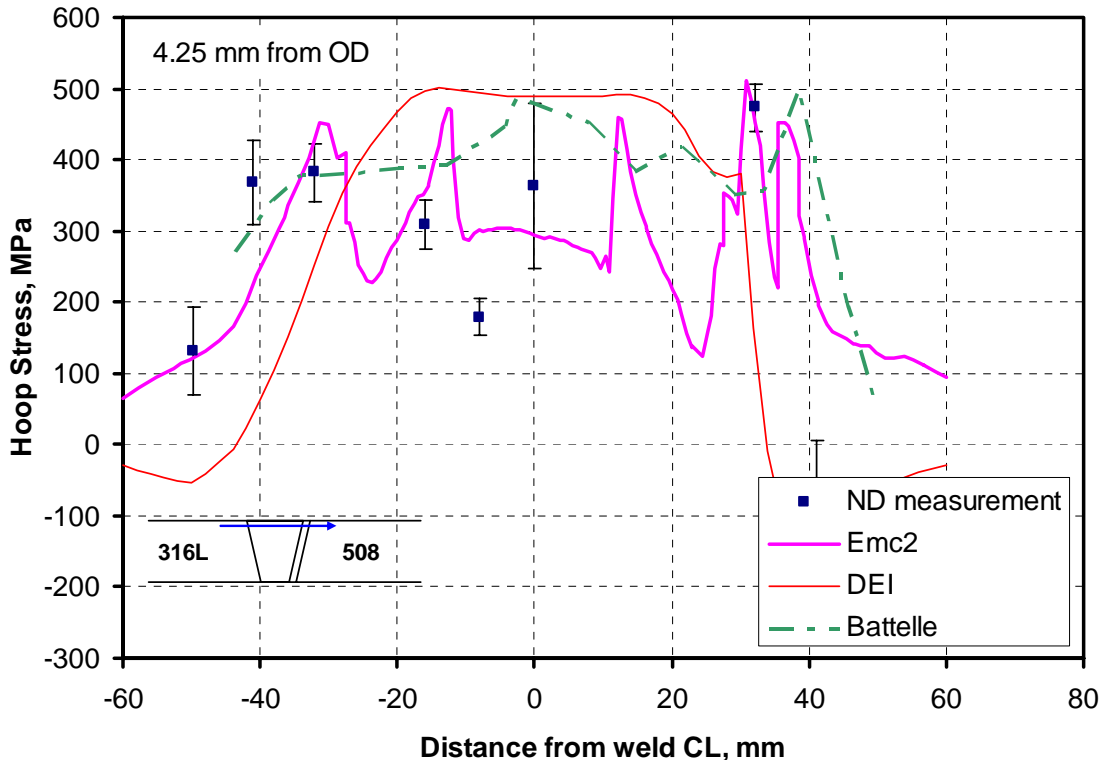
Figure 10 Residual hoop stress comparison with DEI and Battelle at 4.25 mm below OD
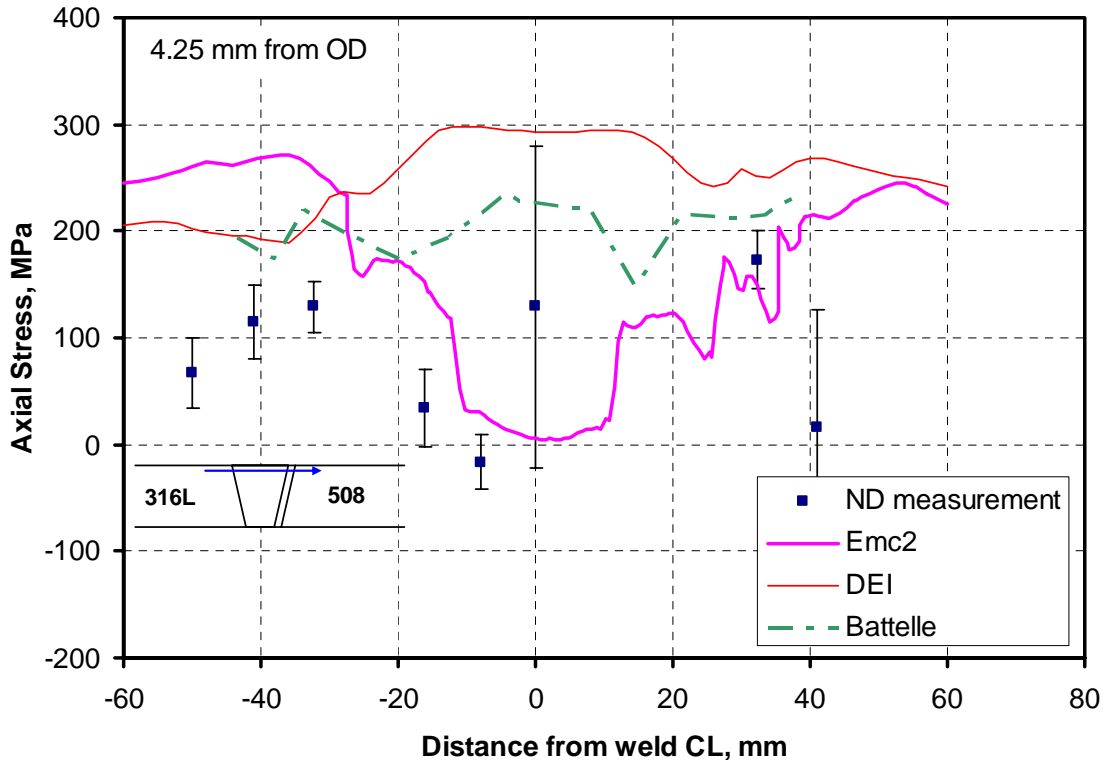
Figure 11 Residual axial stress comparison with DEI and Battelle at 4.25 mm below OD

A-10
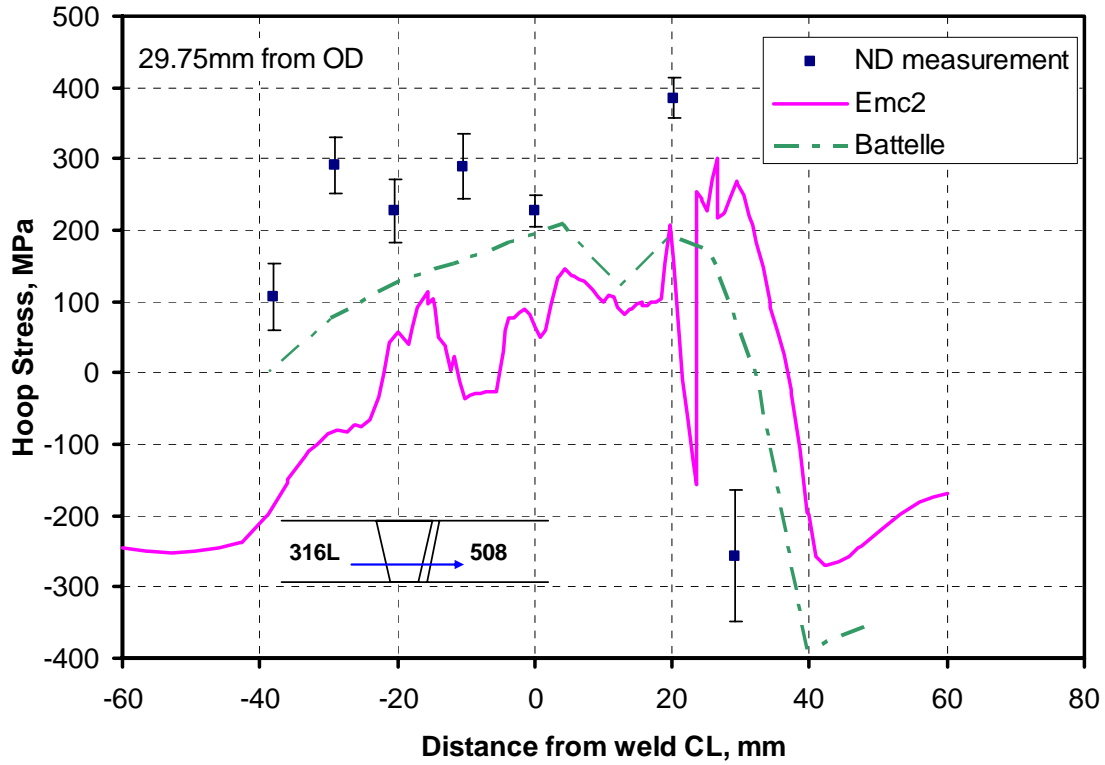
Figure 12 Residual hoop stress comparison with Battelle at 29.75 mm below OD
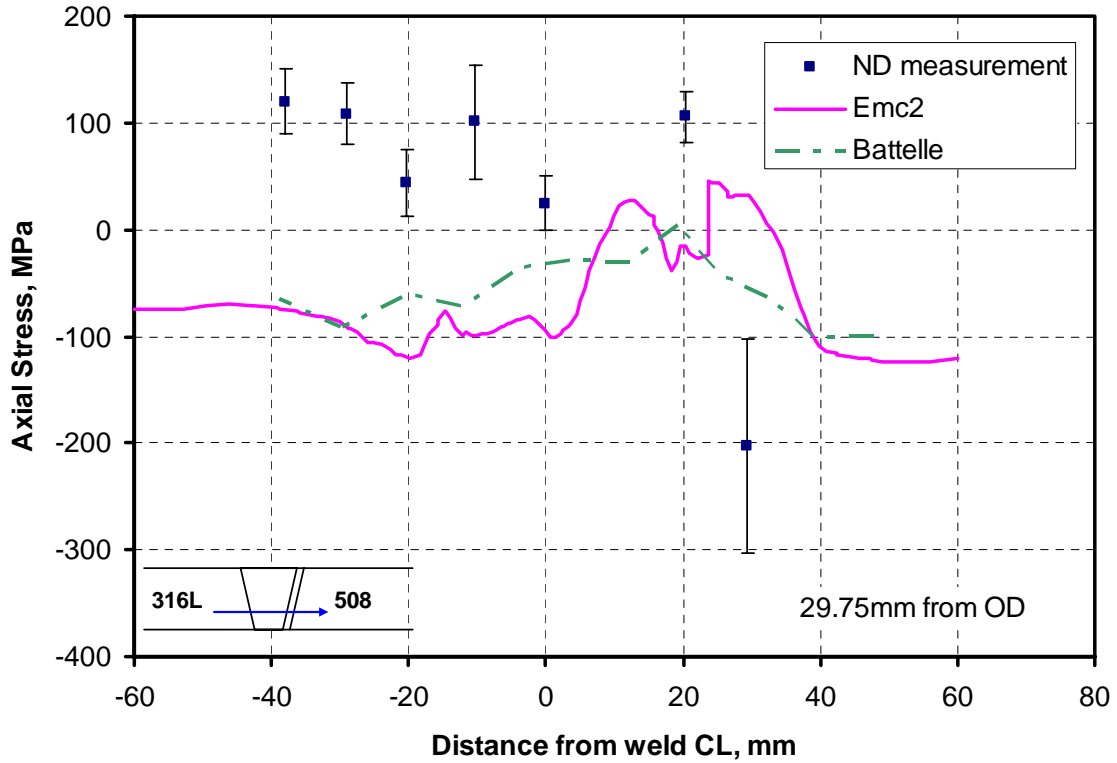
Figure 13 Residual axial stress comparison with Battelle at 29.75 mm below OD
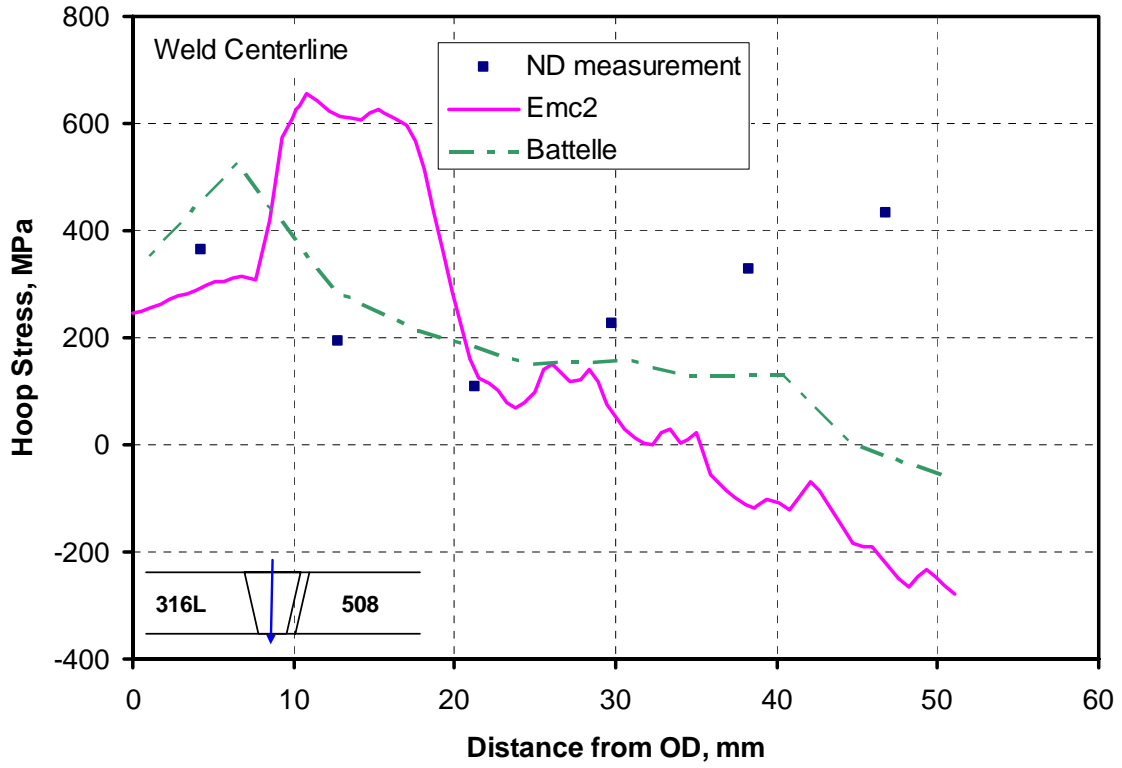
Figure 14 Residual hoop stress comparison with Battelle along weld center
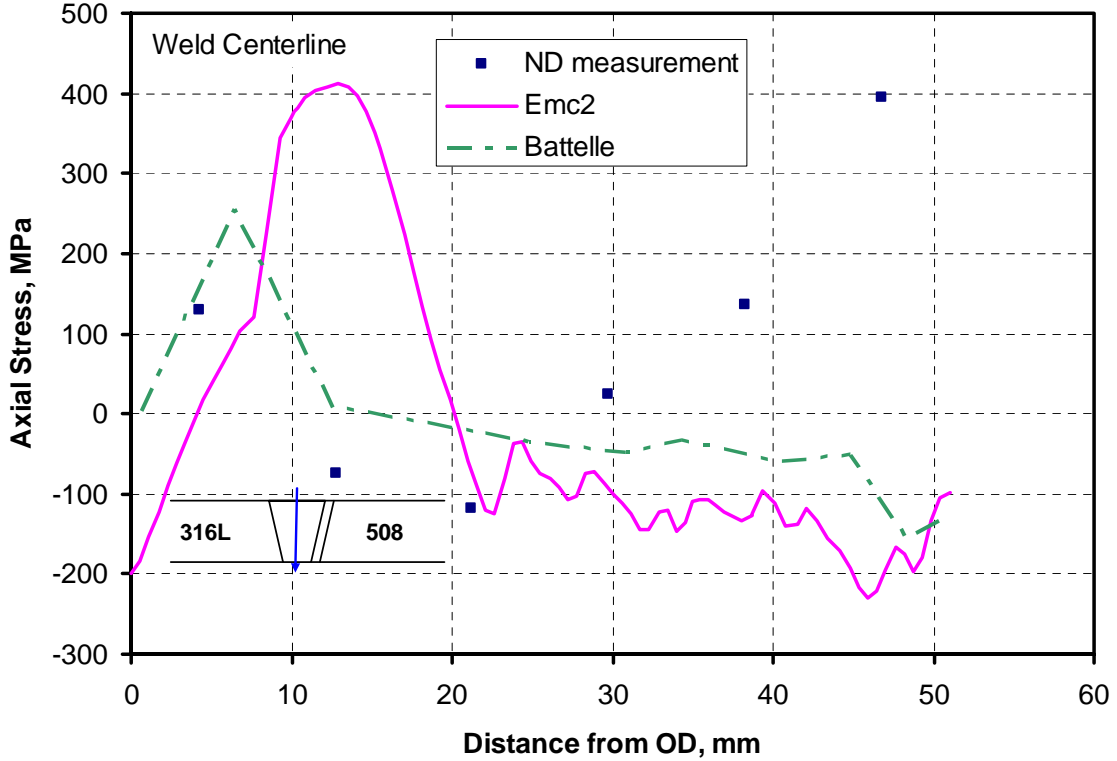
Figure 15 Residual axial stress comparison with Battelle along weld center

A-12
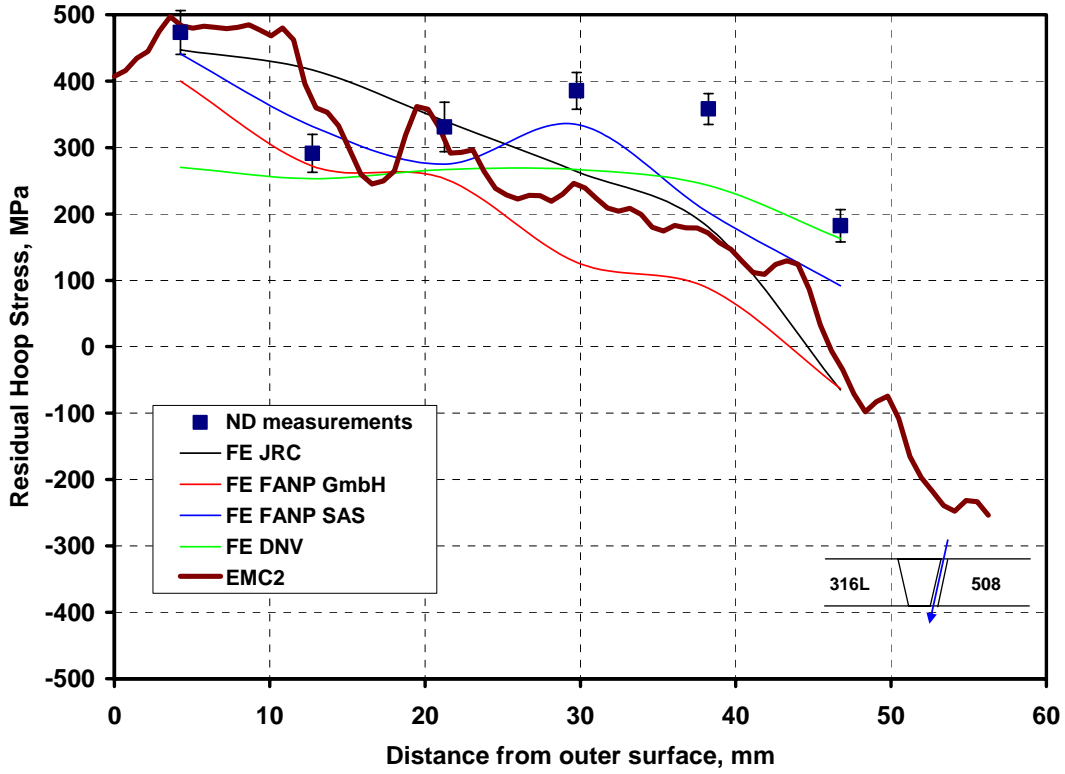
Figure 16 Comparison of various residual hoop stress plots along the center of butter
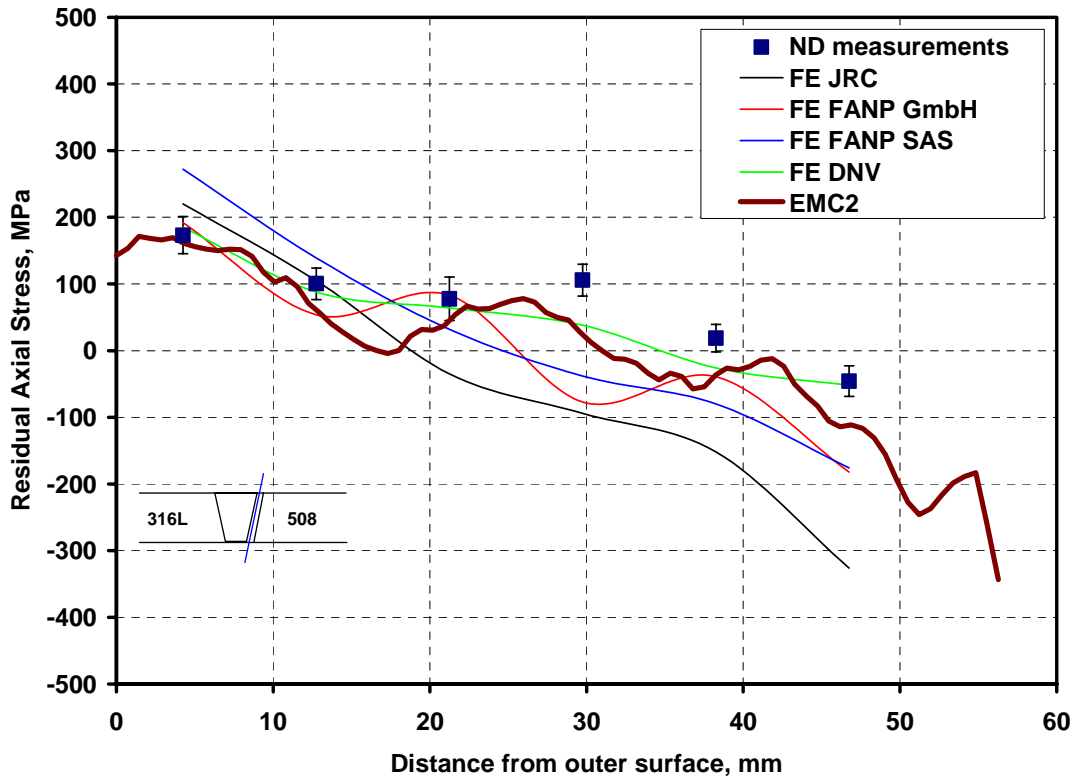
Figure 17 Comparison of various residual axial stress plots along the center of butter

A-13
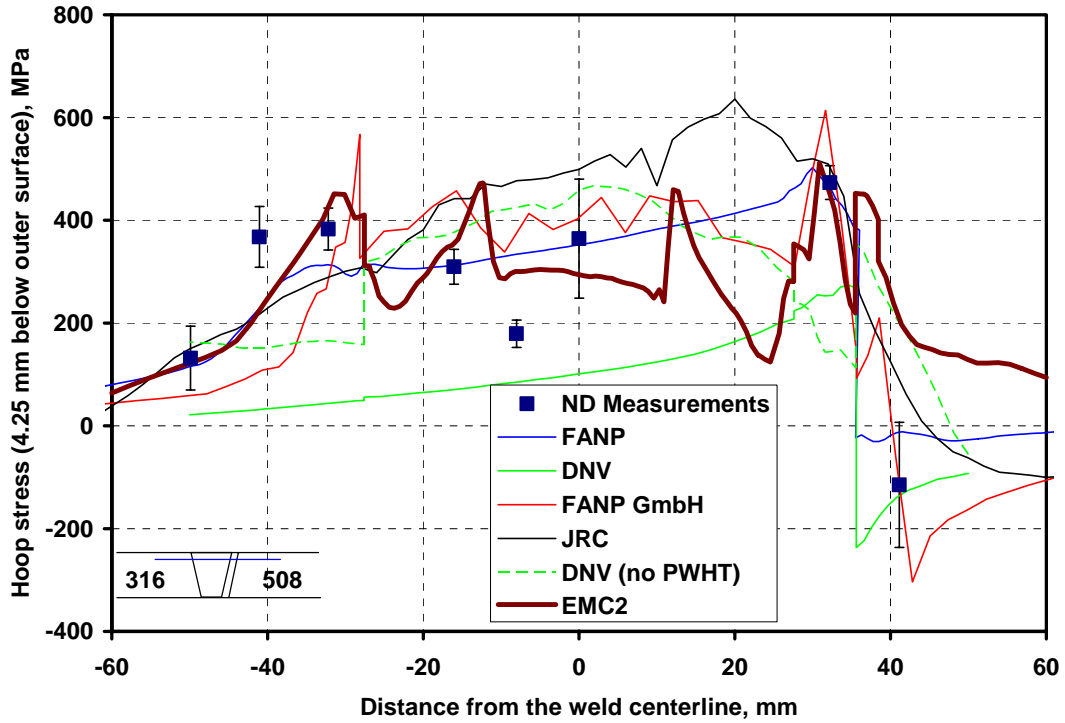
Figure 18 Comparison of various residual hoop stress plots at 4.25 mm below OD
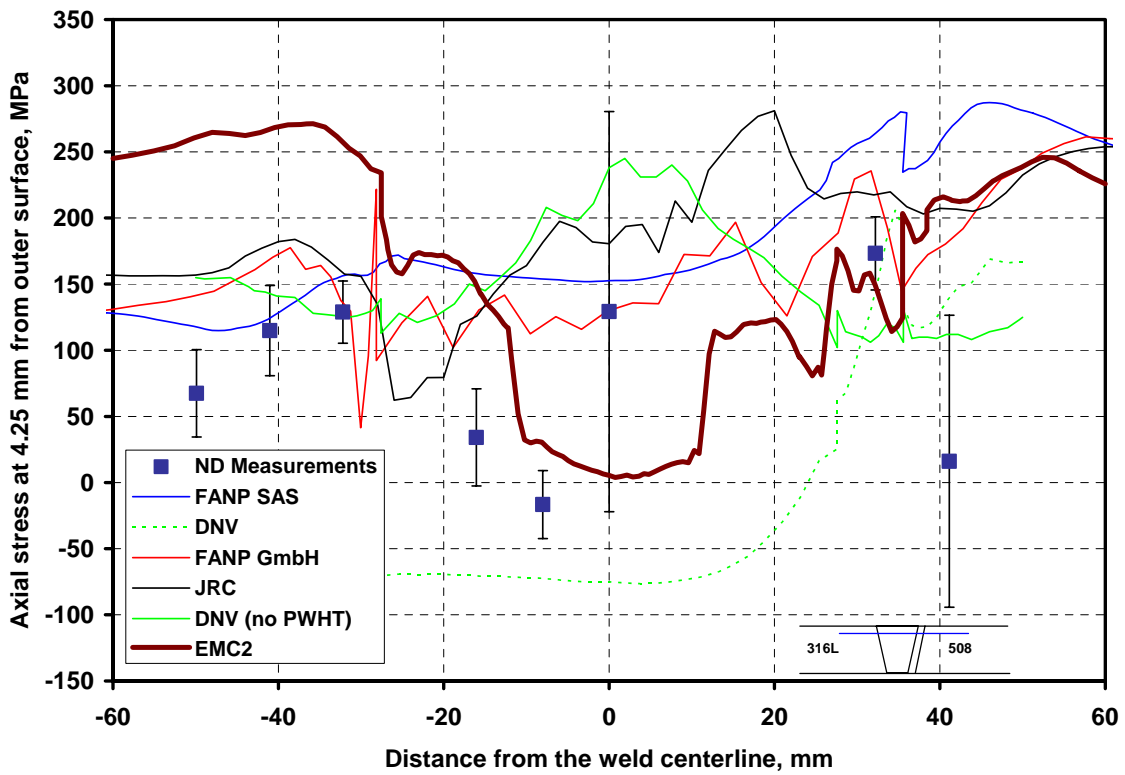
Figure 19 Comparison of various residual axial stress plots at 4.25 mm below OD
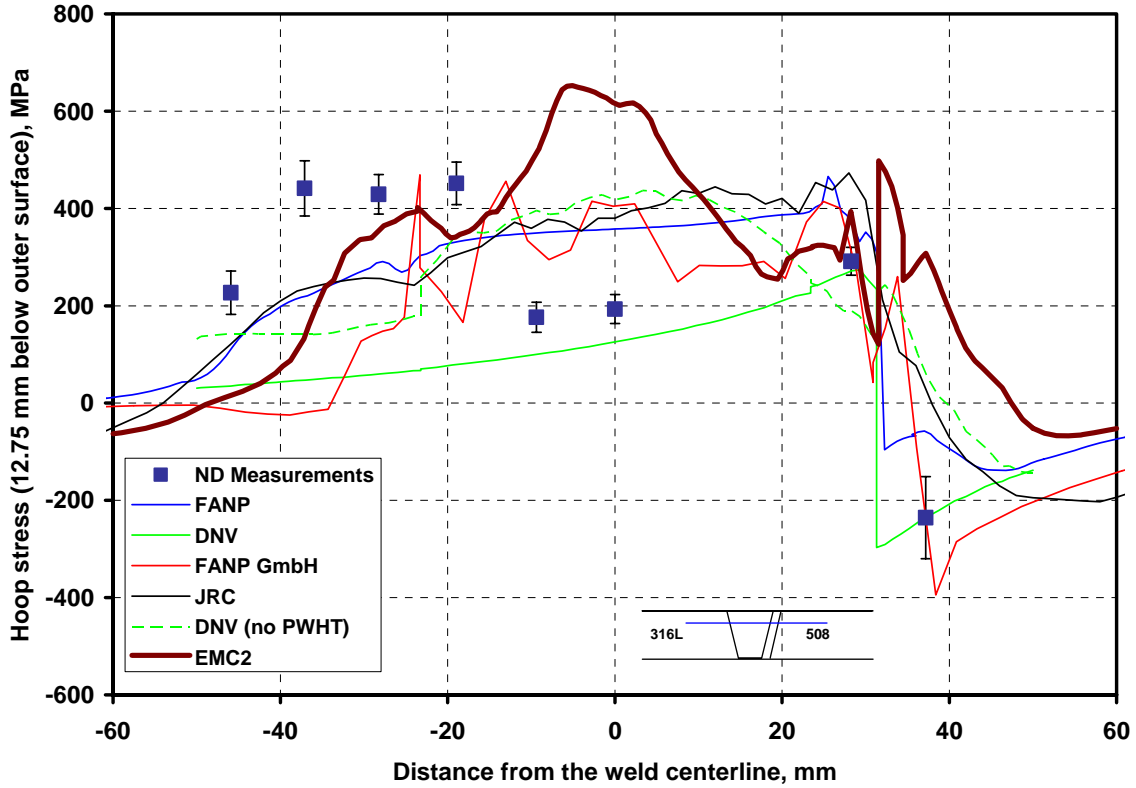
Figure 20 Comparison of various residual hoop stress plots at 12.75 mm below OD
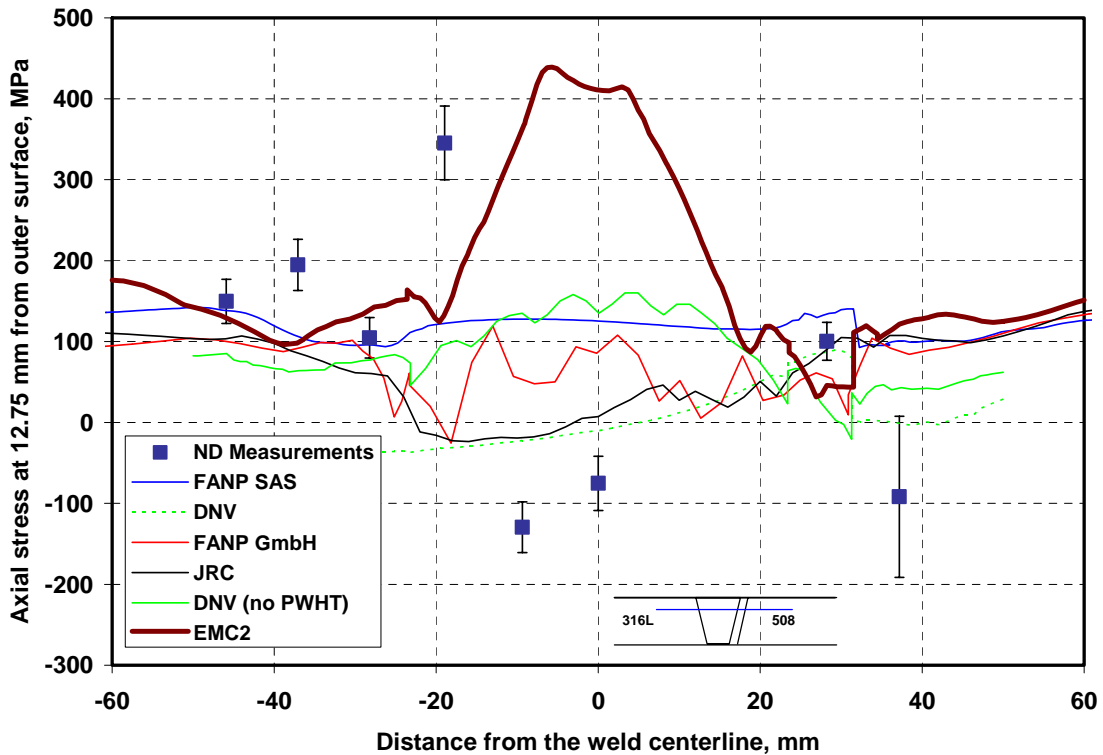
Figure 21 Comparison of various residual axial stress plots at 12.75 mm below OD

A-15
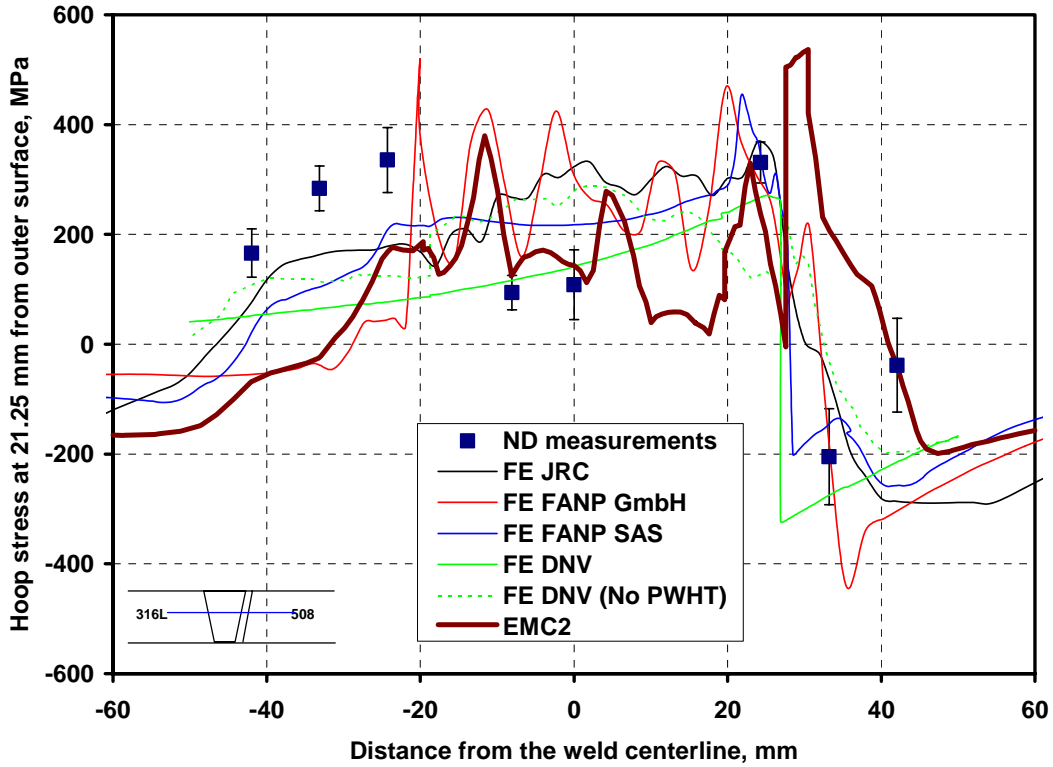
Figure 22 Comparison of various residual hoop stress plots at 21.25 mm below OD
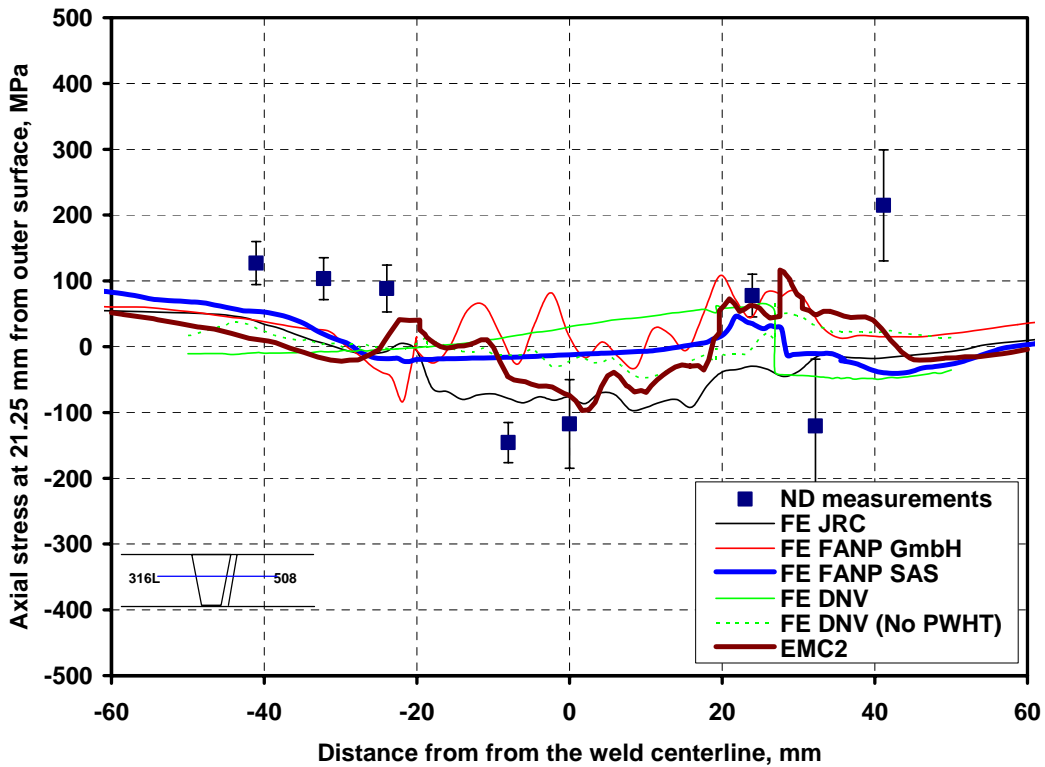
Figure 23 Comparison of various residual axial stress plots at 21.25 mm below OD

A-16
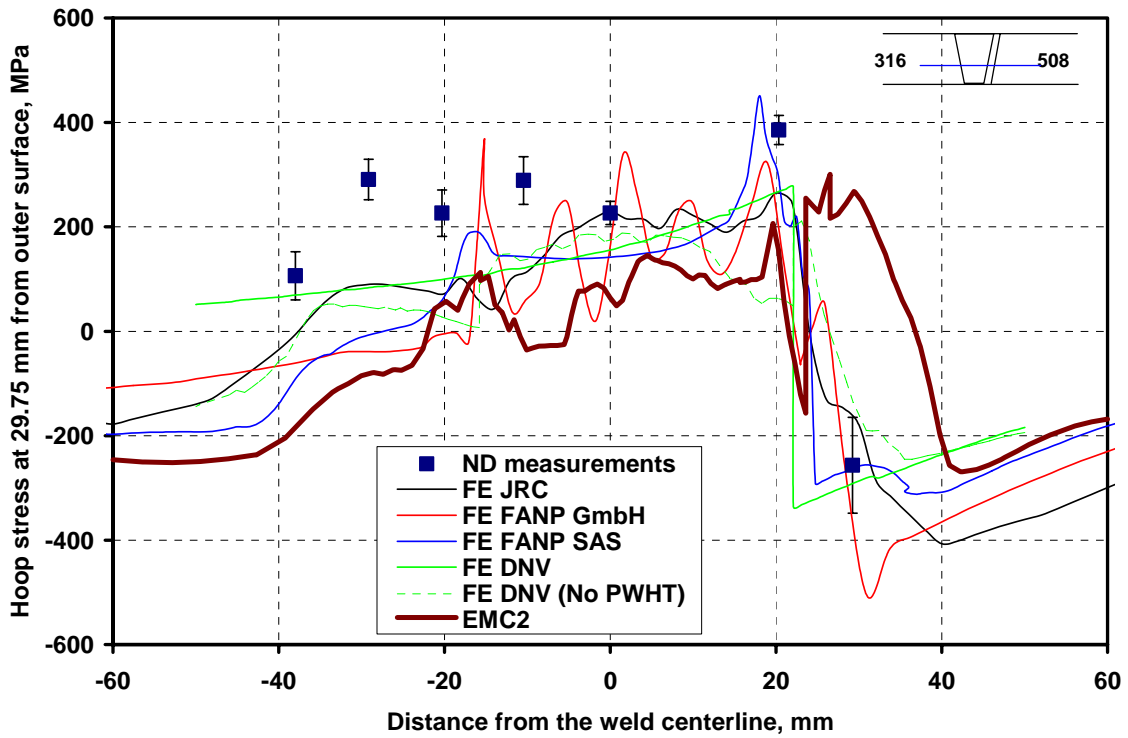
Figure 24 Comparison of various residual hoop stress plots at 29.75 mm below OD
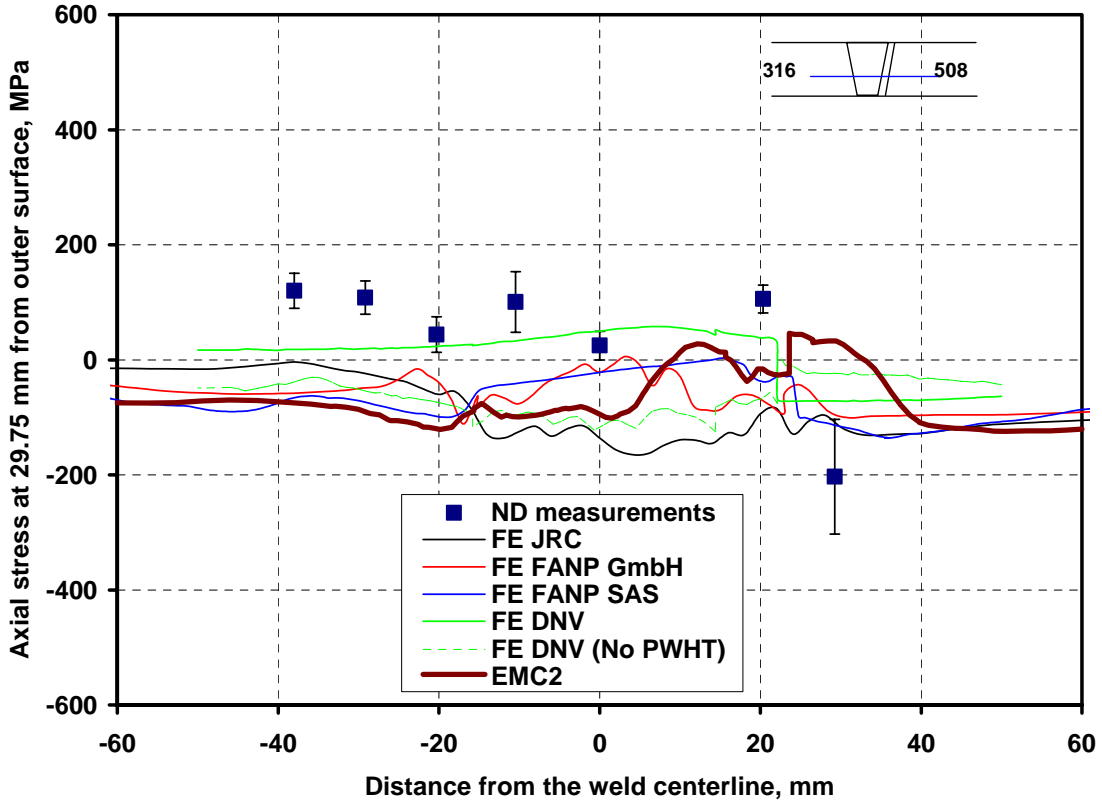
Figure 25   Comparison of various residual axial stress plots at 29.75 mm below OD

A-17
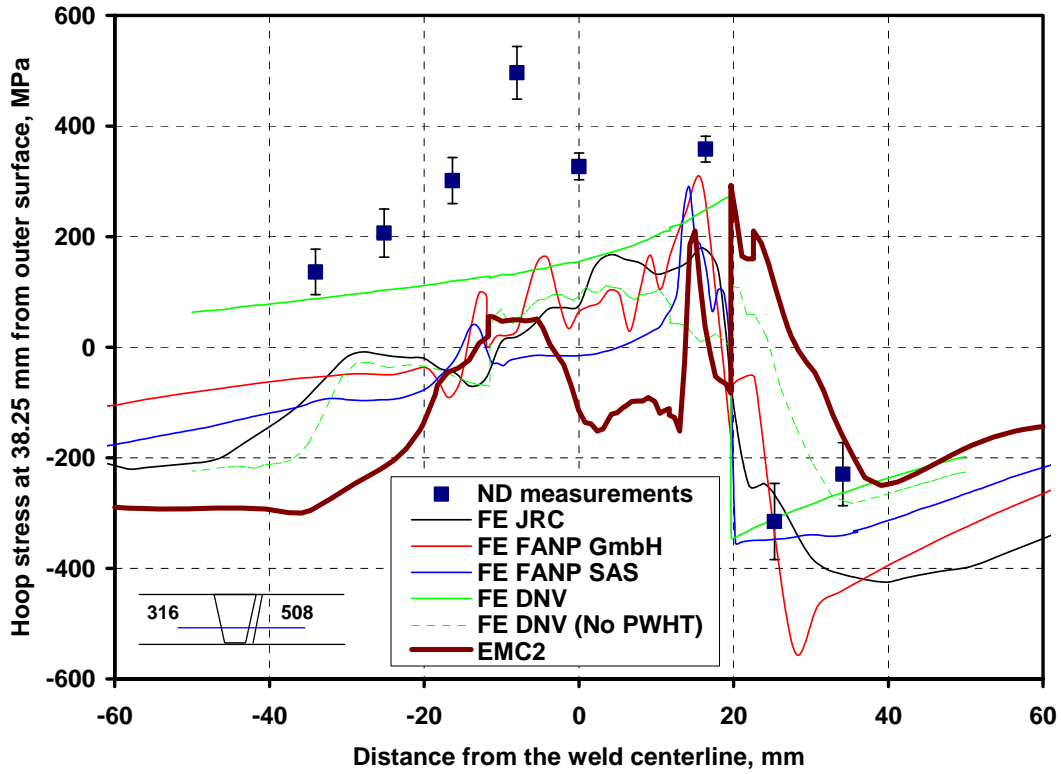
Figure 26   Comparison of various residual hoop stress plots at 38.25 mm below OD
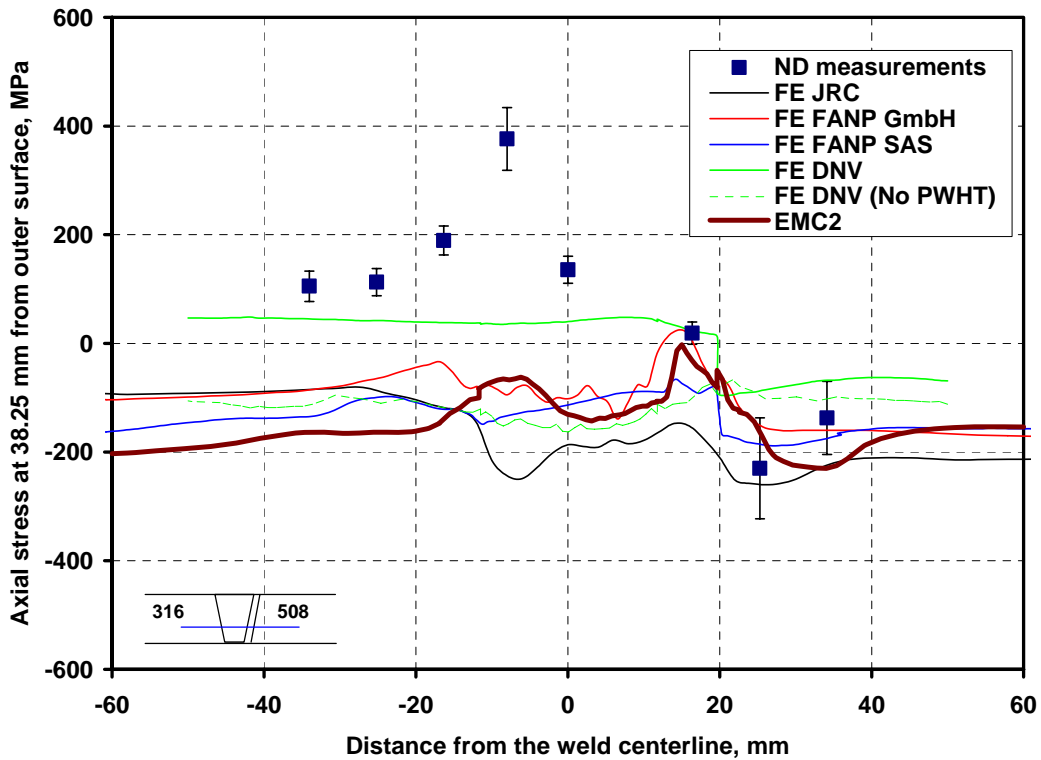
Figure 27   Comparison of various residual axial stress plots at 38.25 mm below OD
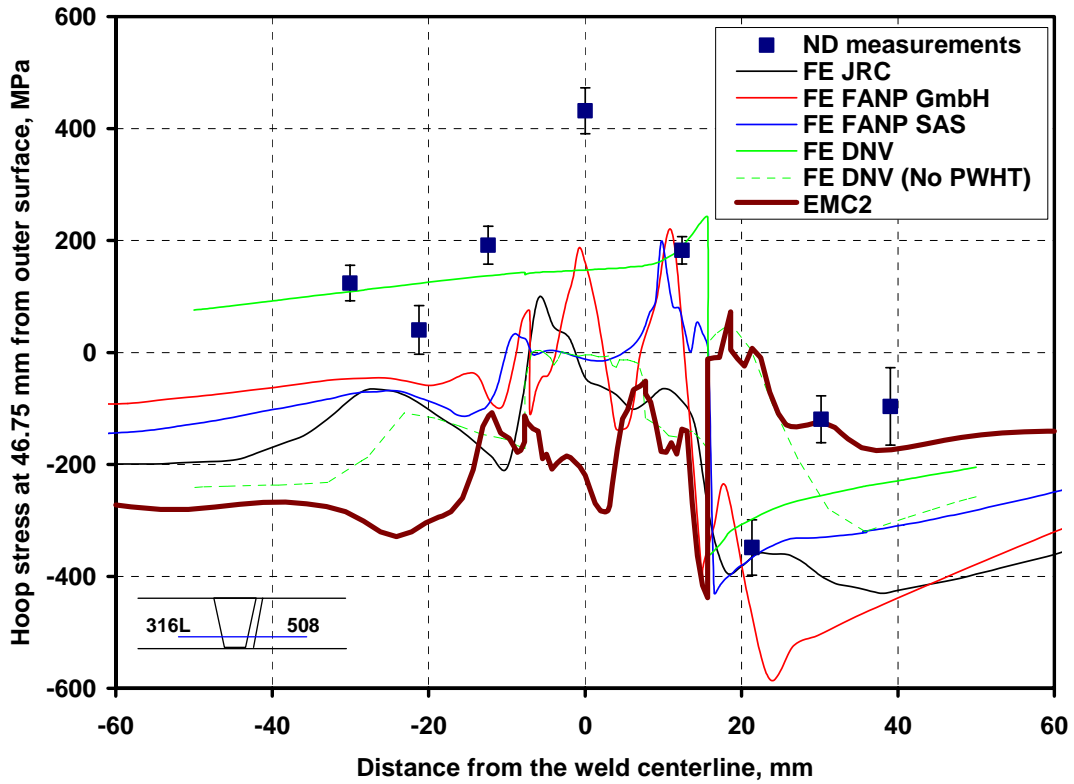
Figure 28   Comparison of various residual hoop stress plots at 46.75 mm below OD
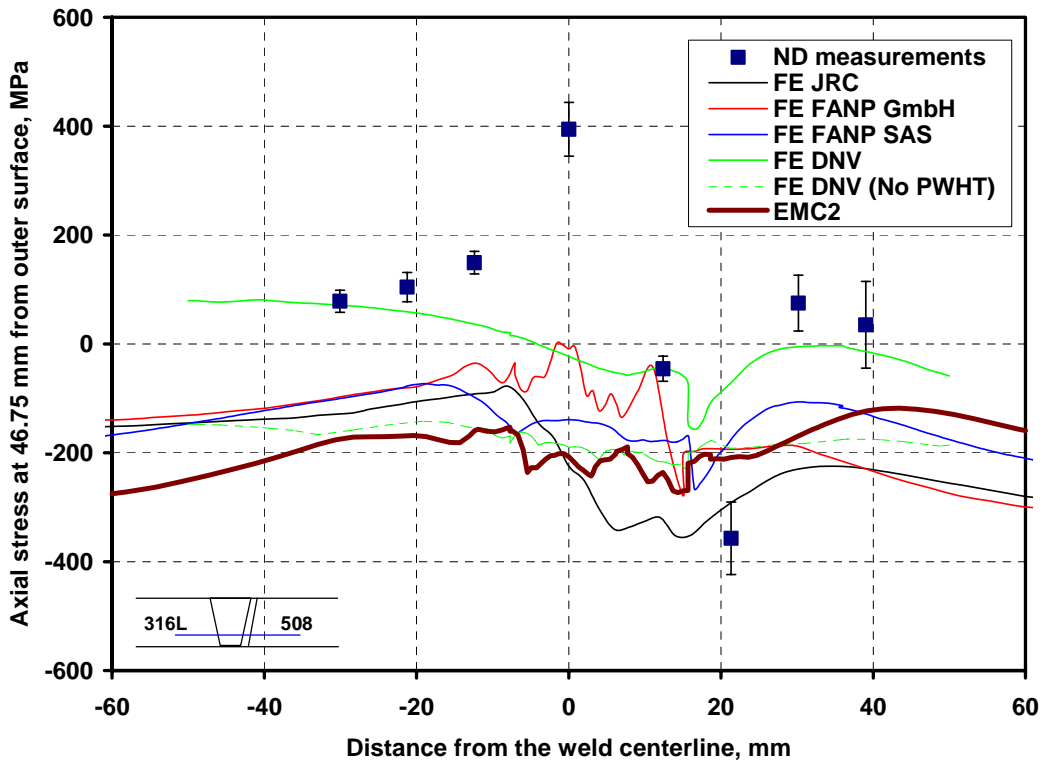
Figure 29   Comparison of various residual axial stress plots at 46.75 mm below OD
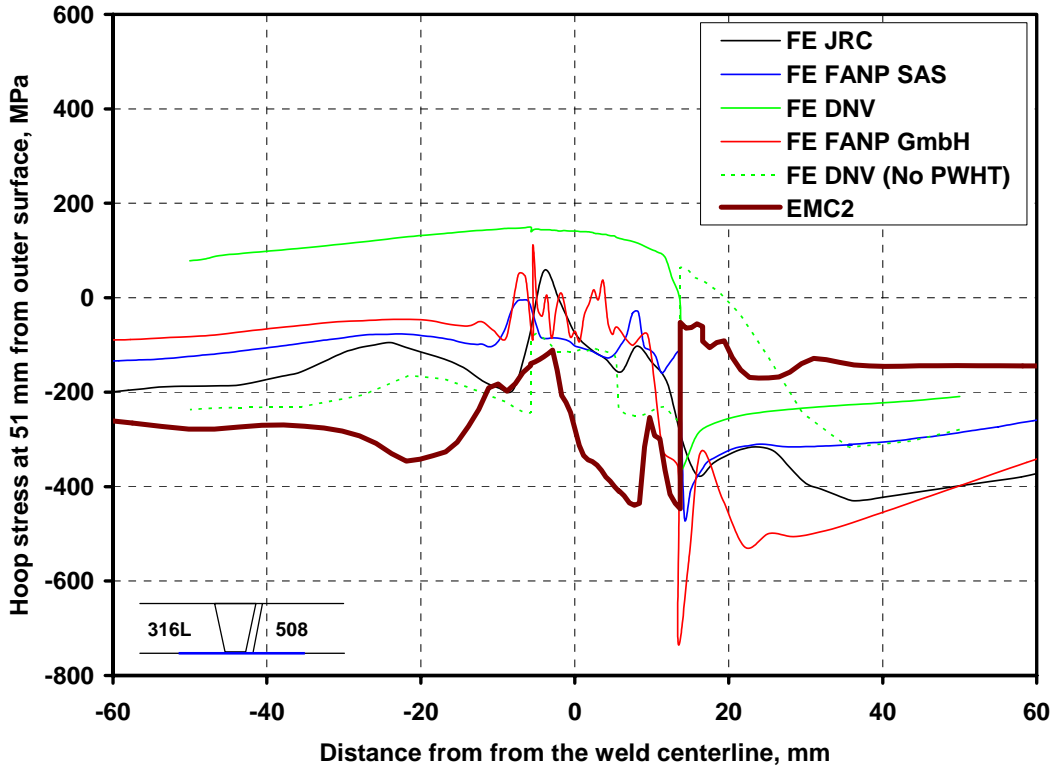
Figure 30 Comparison of various residual hoop stress plots at 51 mm (ID) below OD
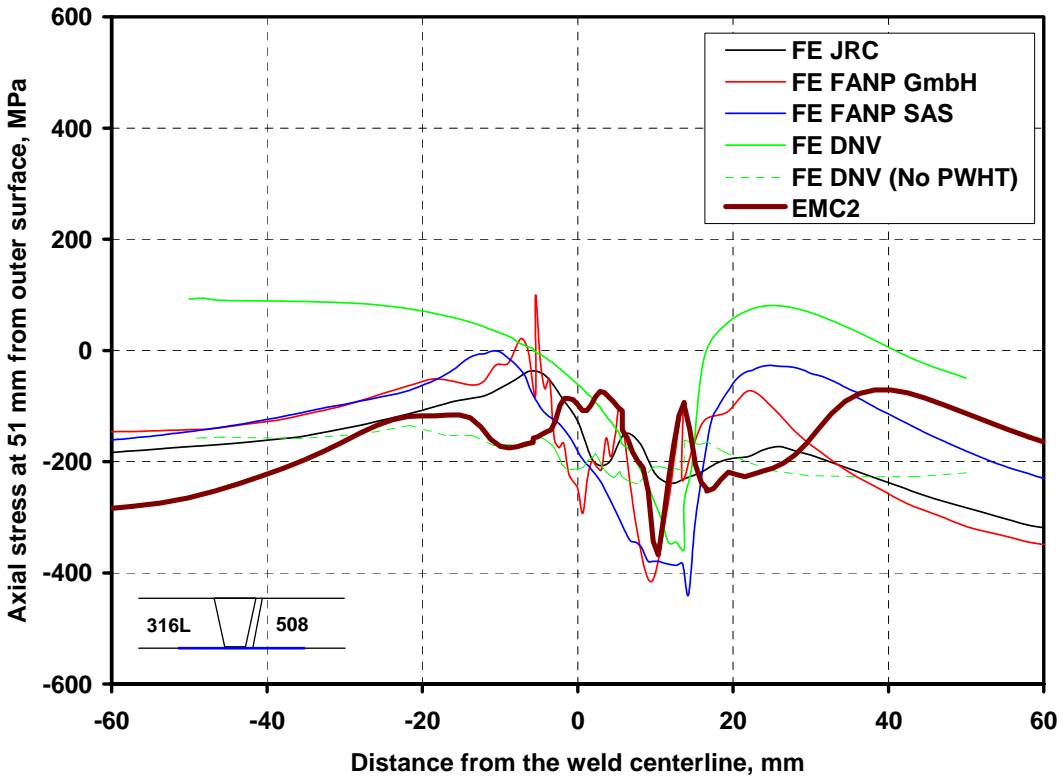
Figure 31 Comparison of various residual axial stress plots at 51 mm (ID) below OD

Appendix B – Margin and Leak Rate Results from Emc^2 Confirmatory Analyses
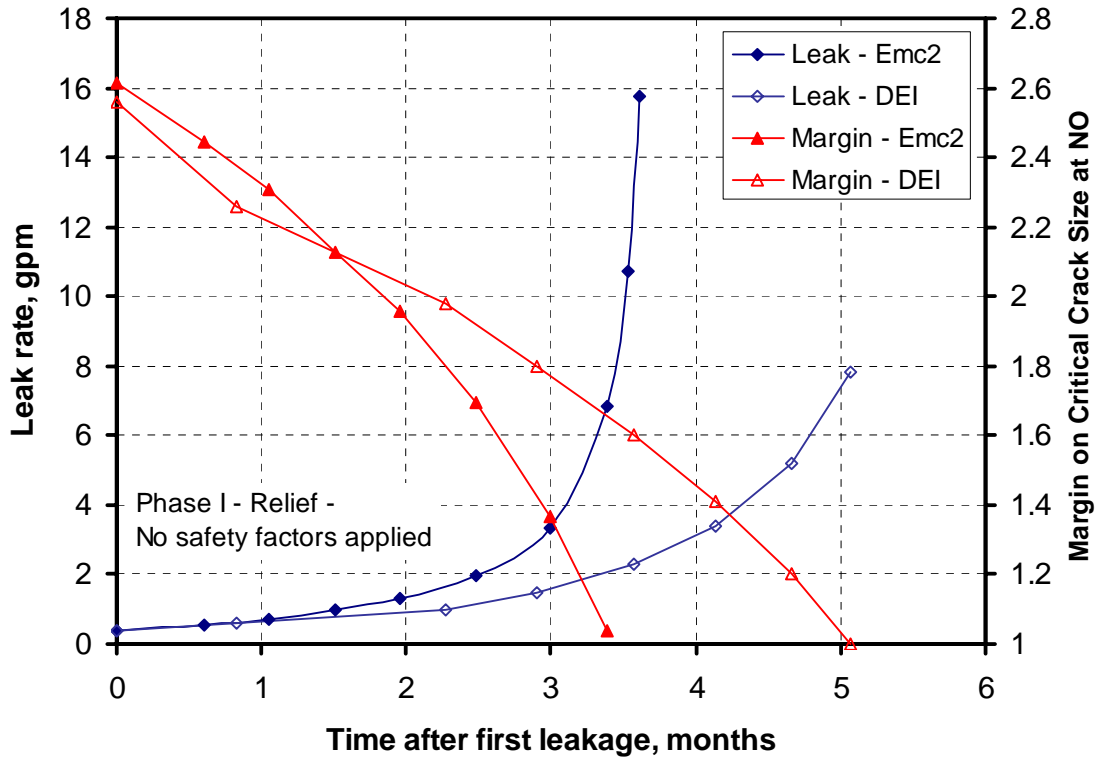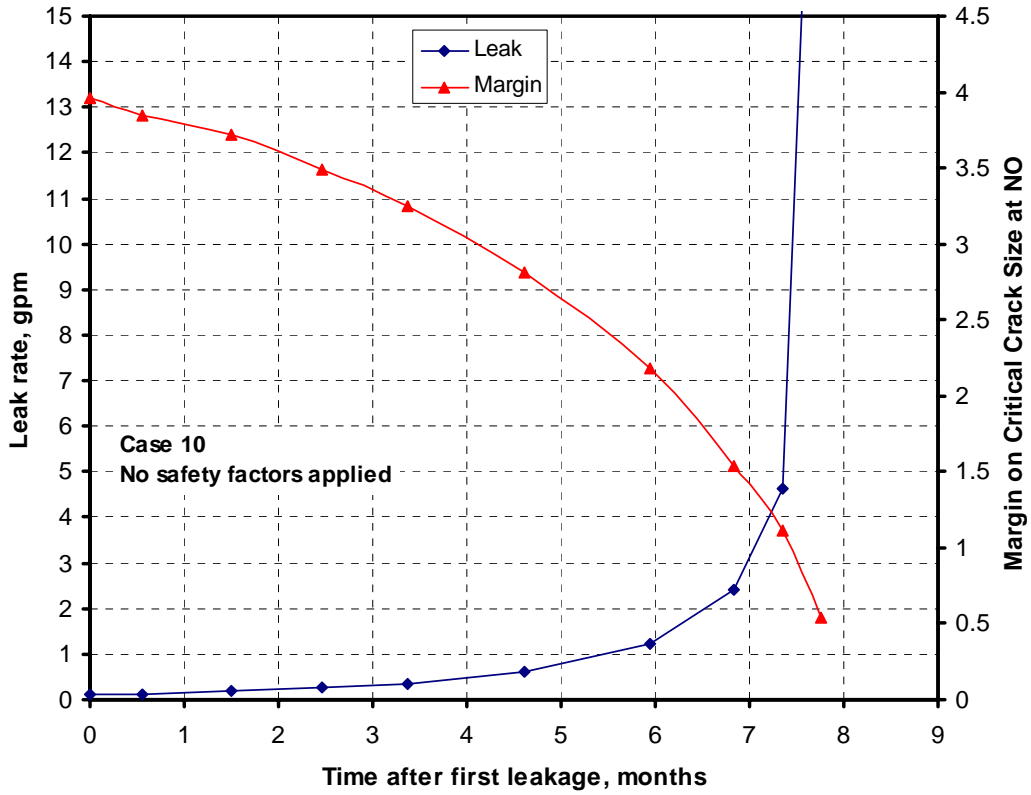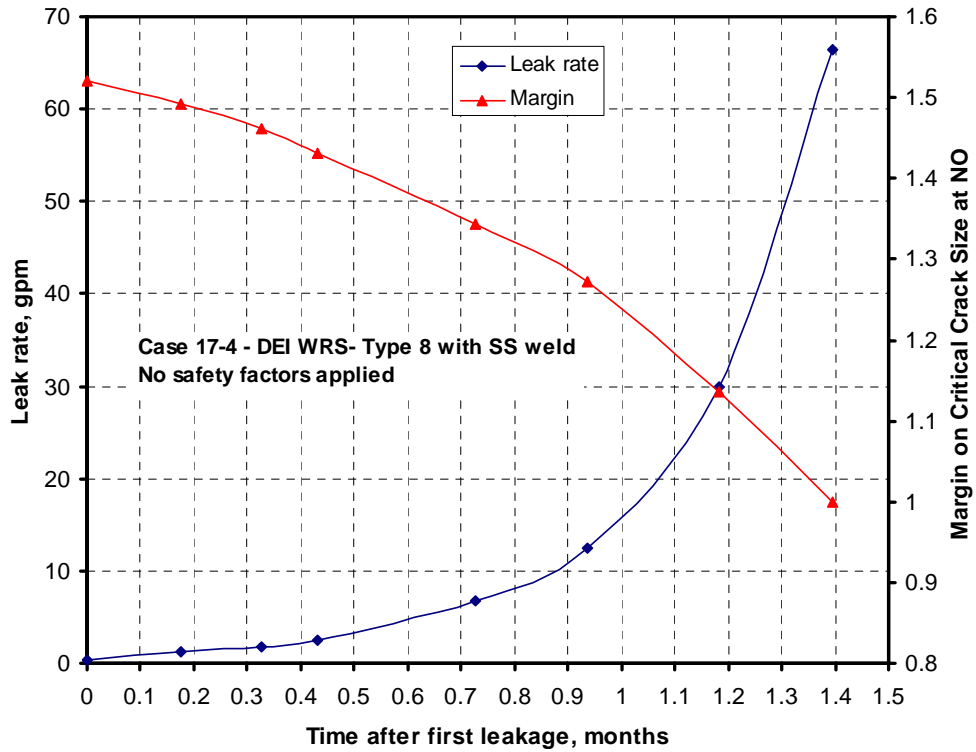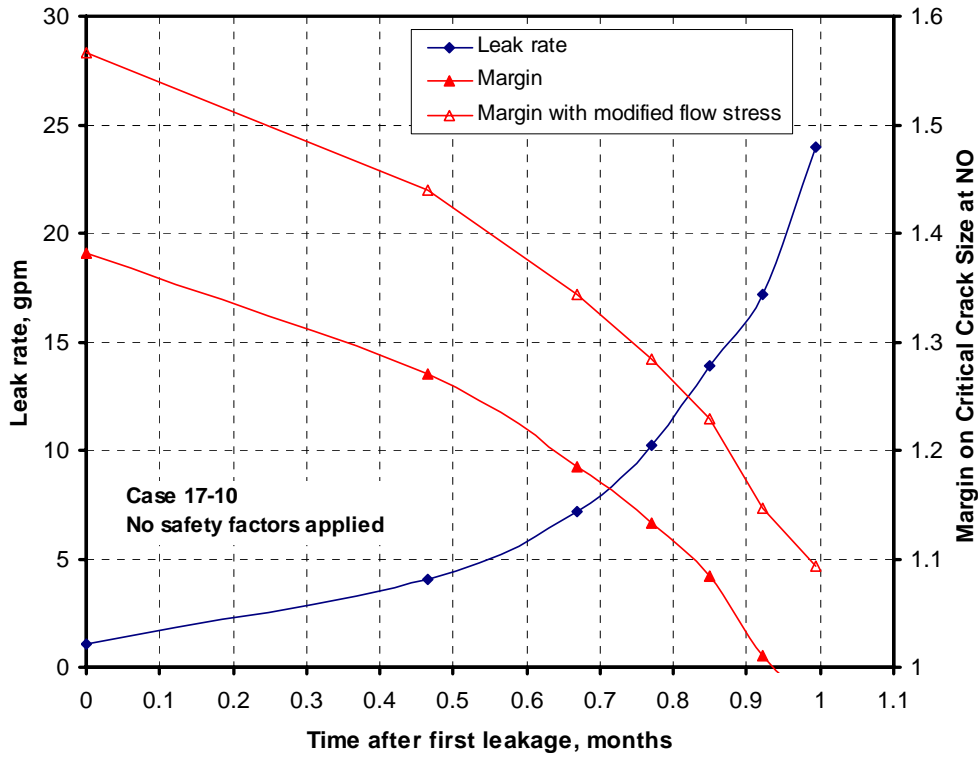
Figure 1 Margin and leak rate results for the Case P1
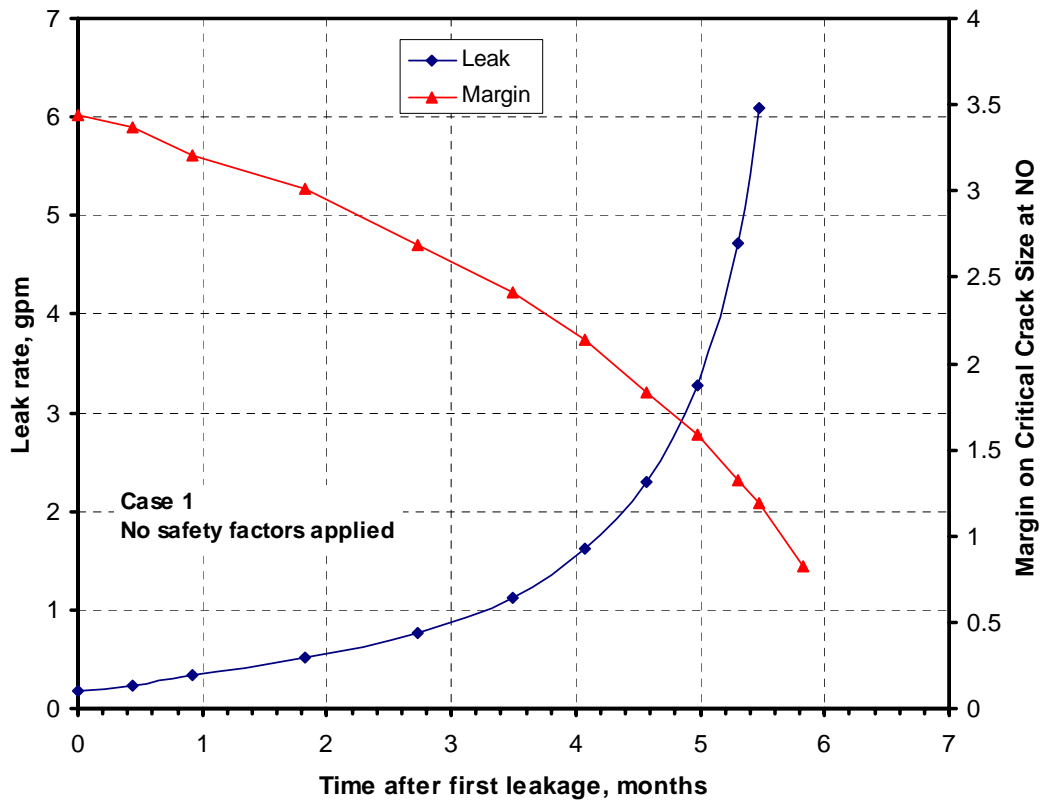
Figure 2 Margin and leak rate results for the Case 1
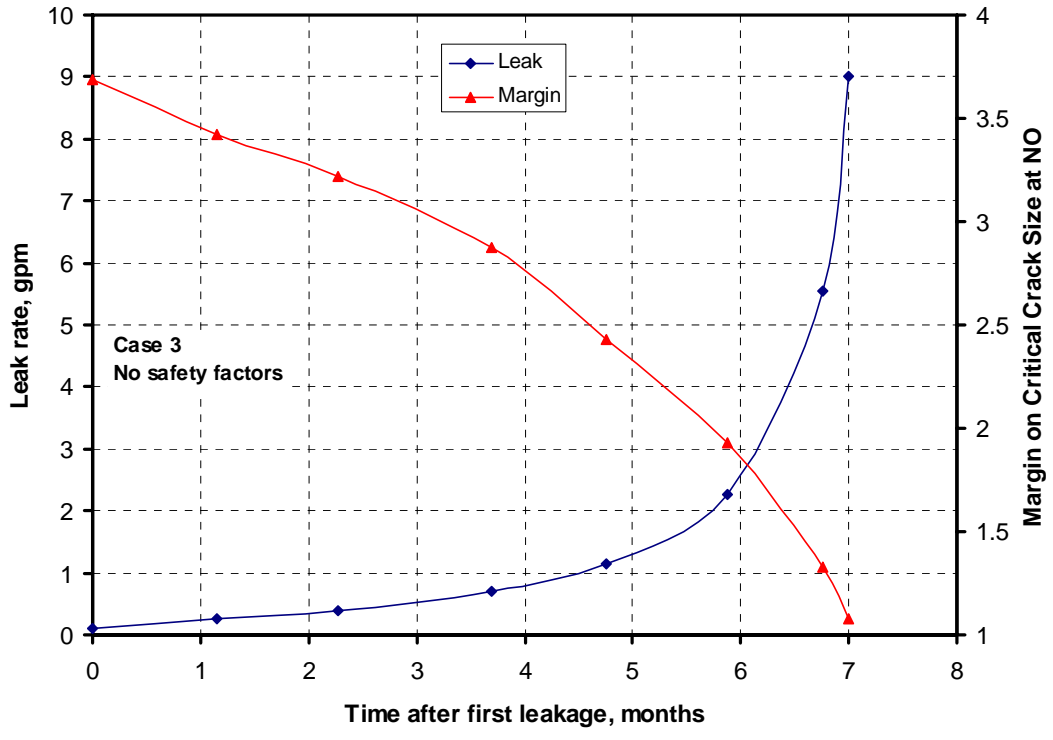
Figure 3 Margin and leak rate results for the Case 3
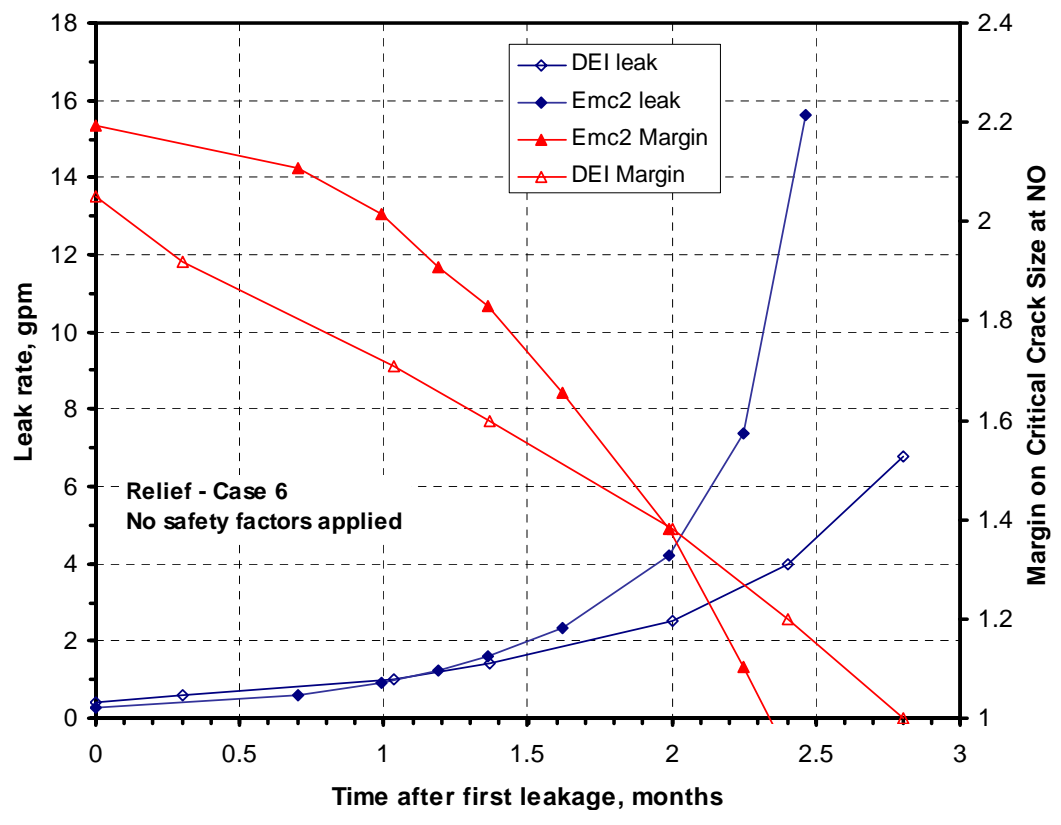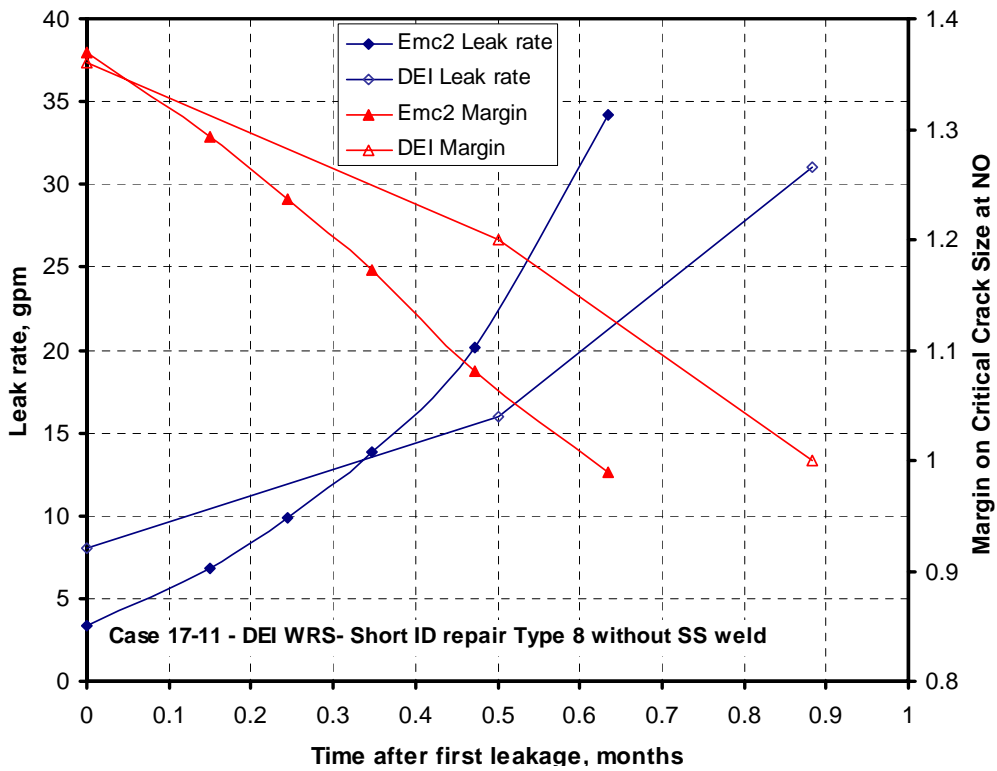

Figure 4 Margin and leak rate results for the Case 6
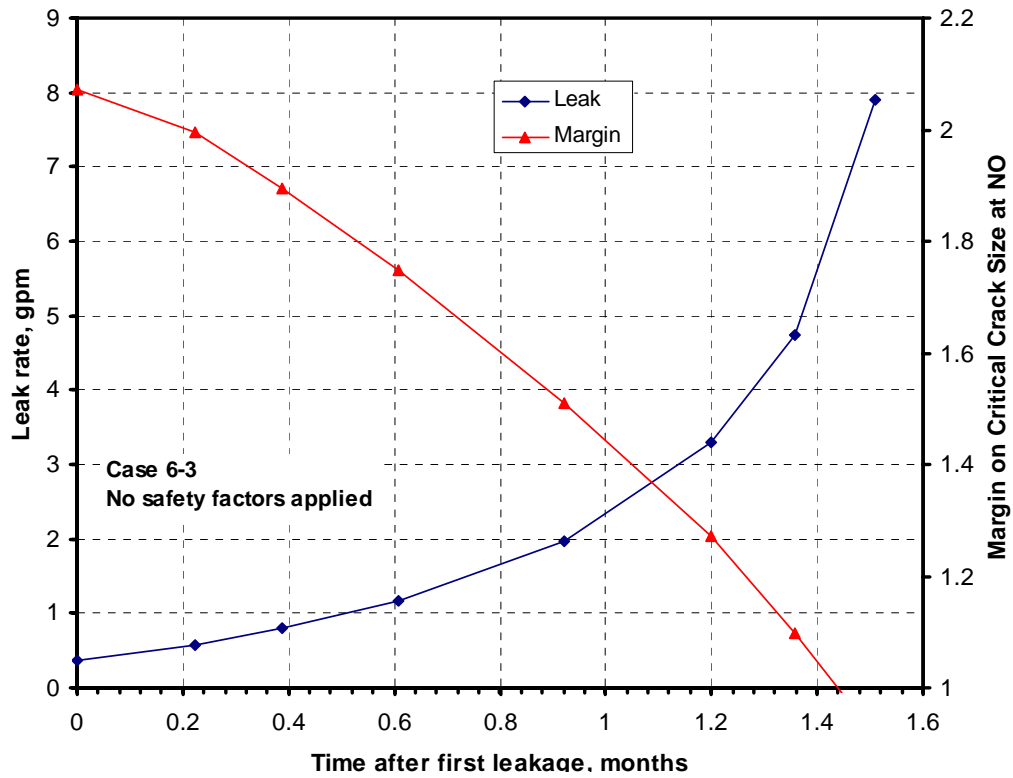
Figure 5 Margin and leak rate results for the Case 6-3
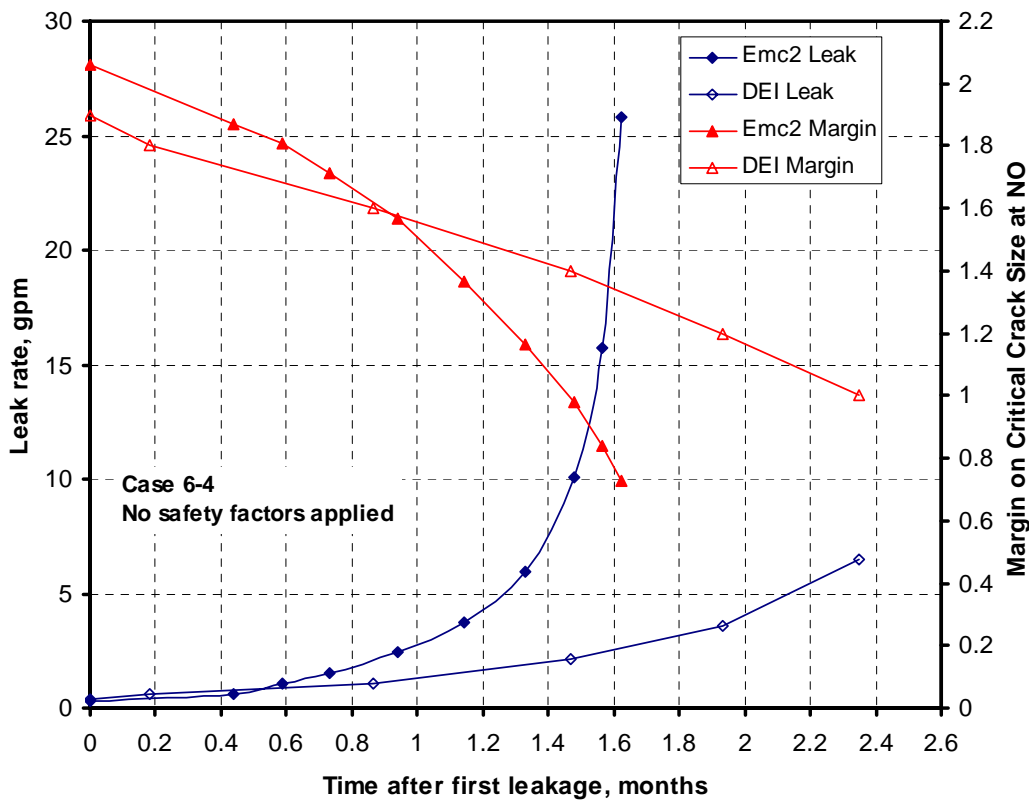
Figure 6 Margin and leak rate results for the Case 6-4
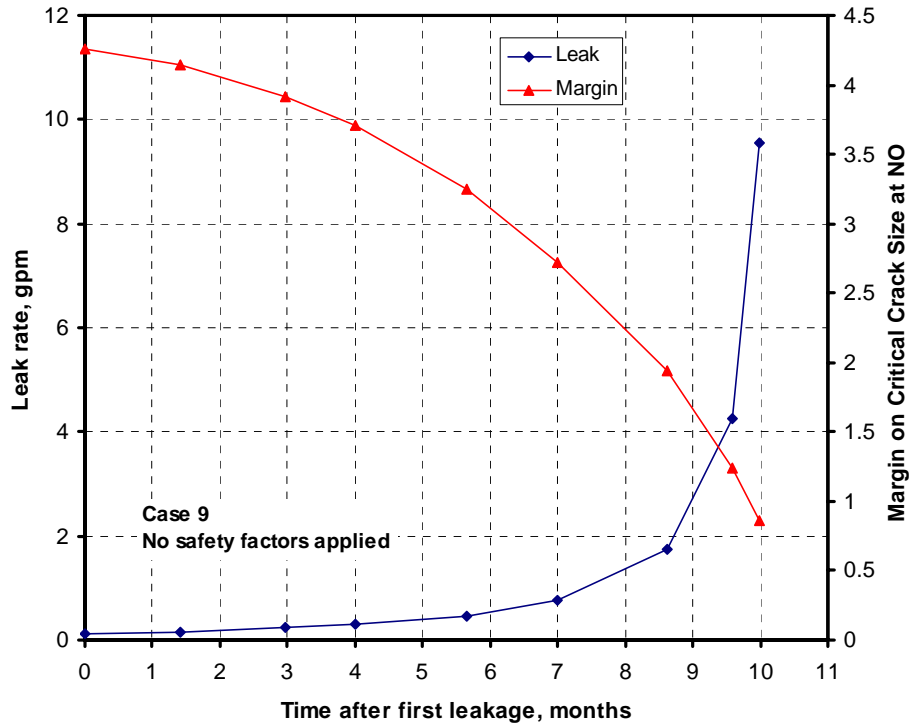
Figure 7 Margin and leak rate results for the Case 9
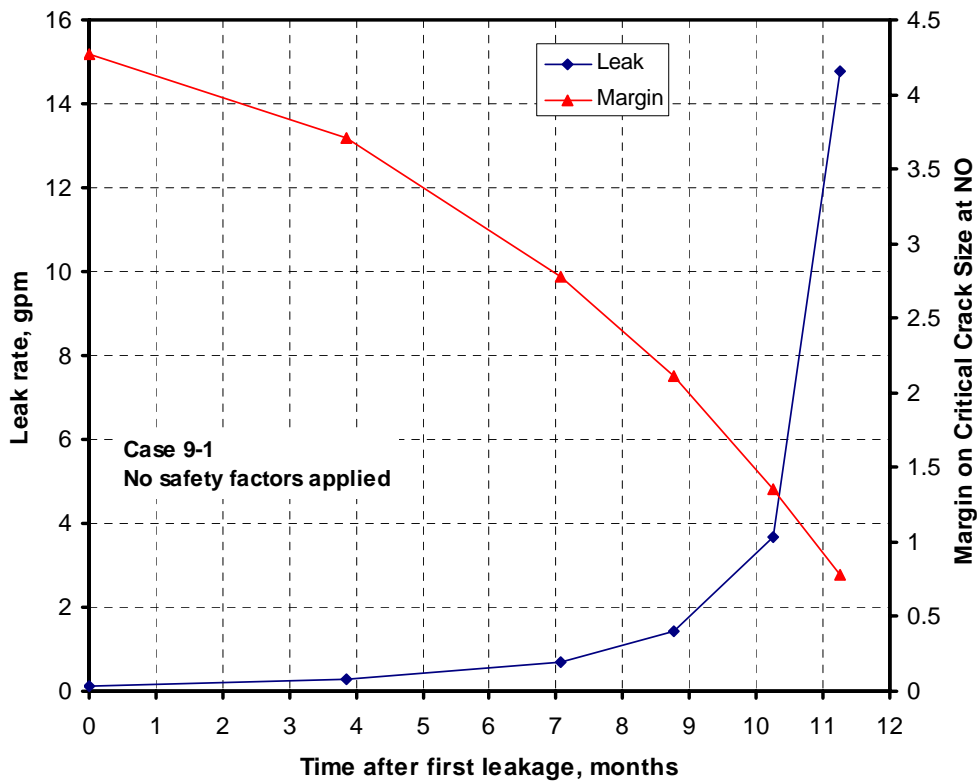
Figure 8 Margin and leak rate results for the Case 9-1

Figure 9 Margin and leak rate results for the Case 10

Figure 10 Margin and leak rate results for the Case 17-4

Figure 11　Margin and leak rate results for the Case 17-10

Figure 12　Margin and leak rate results for the Case 17-11
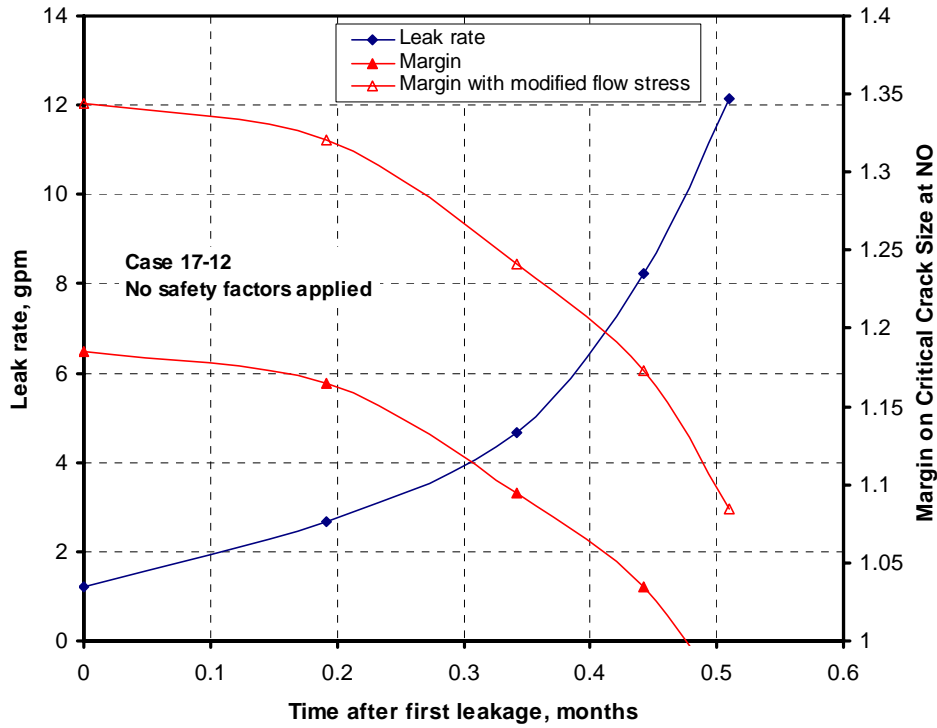
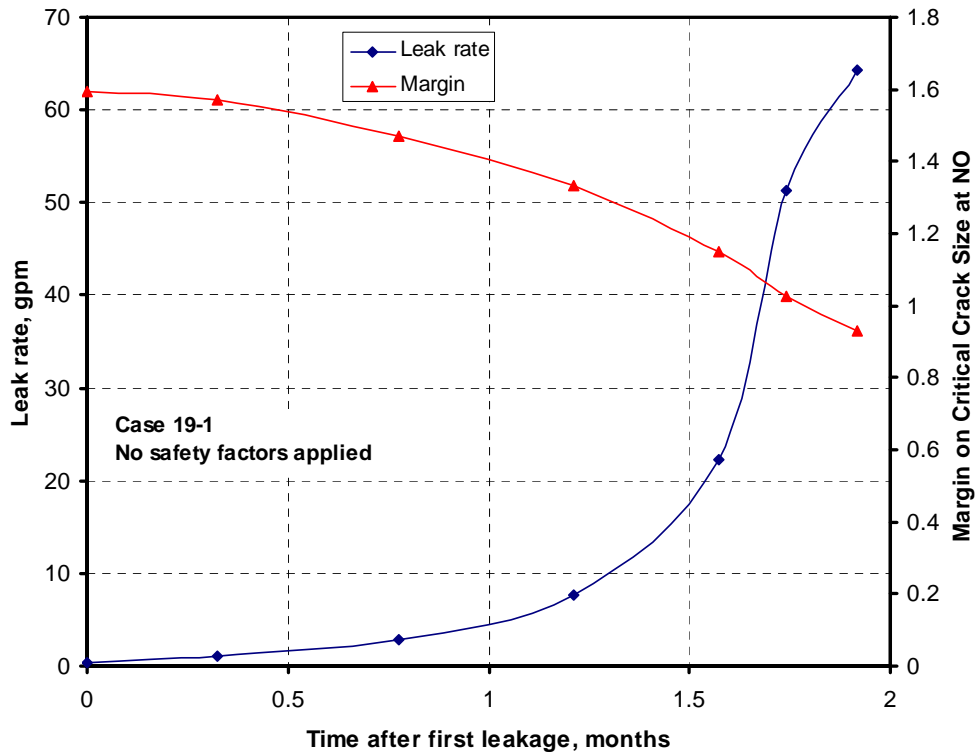**Figure 13 Margin and leak rate results for the Case 17-12**

Figure 14 Margin and leak rate results for the Case 19-1